Dual Active Bridge Converters for Electrolyzers

An application oriented perspective

Deshmukh, R.S.

DOI
10.4233/uuid:2c06f348-5cd5-41c8-9a14-dd9ca3b7d987

Publication date
2026

Document Version
Final published version

Citation (APA)
Deshmukh, R. S. (2026). *Dual Active Bridge Converters for Electrolyzers: An application oriented perspective*. [Dissertation (TU Delft), Delft University of Technology]. https://doi.org/10.4233/uuid:2c06f348-5cd5-41c8-9a14-dd9ca3b7d987

Dual Active Bridge Converters for Electrolyzers

An application oriented perspective

Rohan Shailesh Deshmukh

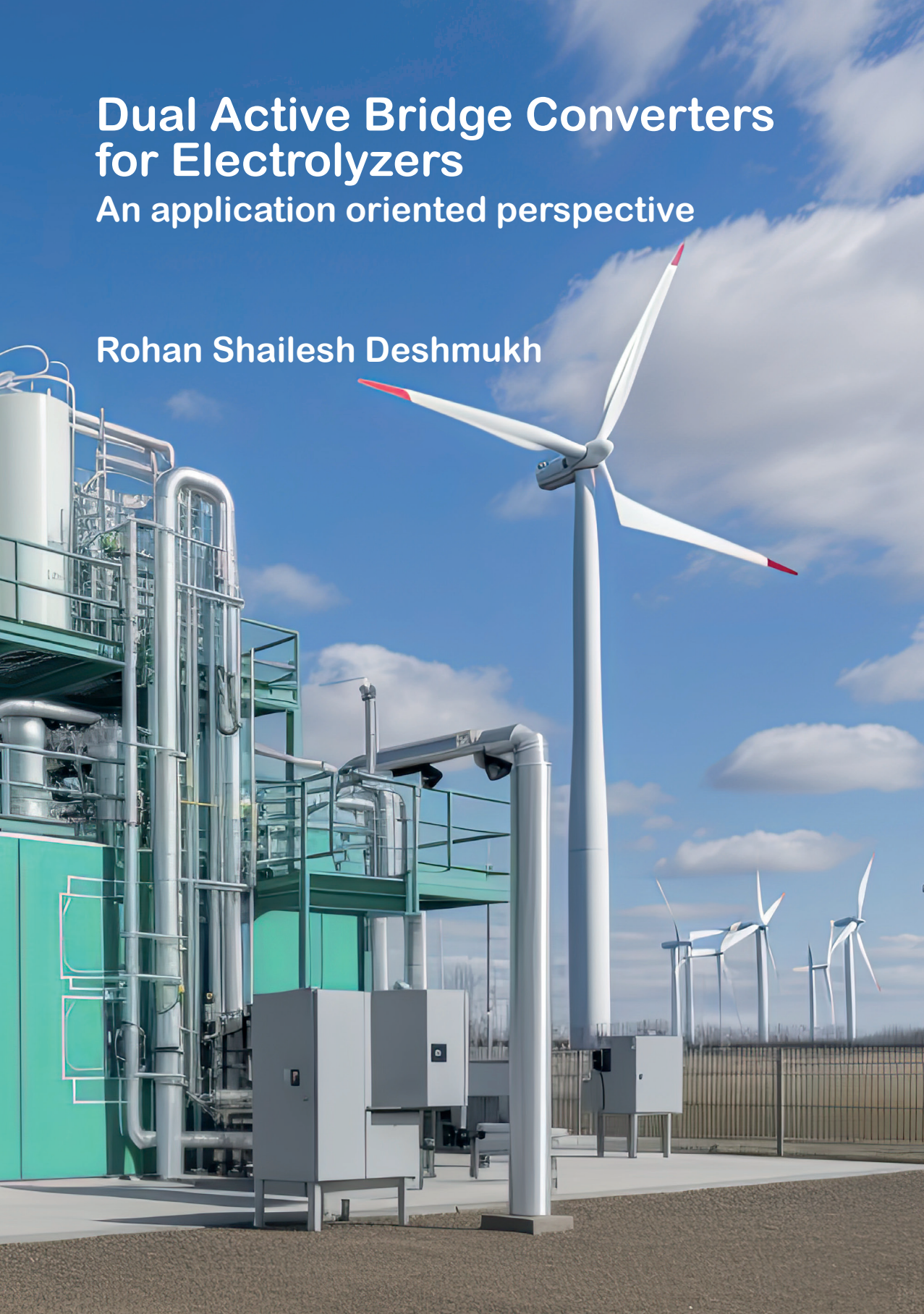

Dual Active Bridge Converters for Electrolyzers

An application oriented perspective

Dual Active Bridge Converters for Electrolyzers

An application oriented perspective

Dissertation

for the purpose of obtaining the degree of doctor
at Delft University of Technology
by the authority of the Rector Magnificus Prof. dr. ir. H. Bijl,
chair of the Board for Doctorates
to be defended publicly on
Monday 2 February, 2026, at 10:00 o'clock

by

Rohan Shailesh DESHMUKH

Master of Science in Electrical Engineering,
Delft University of Technology, The Netherlands,
born in Thane, Maharashtra, India.

This Dissertation has been approved by the (co)promotors.

Composition of the doctoral committee:

Rector Magnificus,	Chairperson
Prof. dr. ir. P. Bauer	Delft University of Technology, promotor
Dr. ir. H. Vahedi	Delft University of Technology, copromotor
Independent members:	
Em. prof. dr. ir. M. Zeman	Delft University of Technology
Dr. dipl.-ing. J. L. Rueda Torres	Delft University of Technology
Dr. Z. Qin	Delft University of Technology
Prof. dr. T. Batista Soeiro	University of Twente
Prof. dr. T. Thiringer	Chalmers University of Technology, Sweden
Prof. dr. ir. M. Popov	Delft University of Technology, reserve member

Keywords: Dual Active Bridge, Hydrogen, Electrolysis, DC/DC converters, Modulation, Real-Time Simulation.

Printed by: Gildeprint

Cover image: Vecteezy.com

Cover design: Rohan Shailesh Deshmukh, and Douwe Oppewal

ISBN/EAN (Hard copy): 978-94-6384-893-0
ISBN/EAN (Digital): 978-94-6518-214-8

An electronic version of this dissertation is available at
`http://repository.tudelft.nl/`.

॥ श्री स्वामी समर्थ ॥

To my parents

CONTENTS

NOMENCLATURE

Abbreviations

AC	Alternating-Current
AEL	Alkaline Electrolyzer
AEM	Anion Exchange Membrane
ANPC	Auxilliary Neutral Point Clamped
CV	Constant Voltage
DAB	Dual Active Bridge
DC	Direct-Current
DPS	Dual Phase Shift Modulation
DT	Digital Twin
EMI	Electromagnetic Interference
EPS	Extended Phase Shift Modulation
ESS	Energy Storage Systems
EU	European Union
EV	Electric Vehicle
FFT	Fast Fourier Transform
FHA	First-Harmonic Approximation
FPGA	Fully Programmable Gate Array
GAM	Generalized Average Model
H-HV	High Voltage H-bridge
H-LV	Low-Voltage H-bridge
HF	High Frequency
HV	High Voltage
HVDC	High Voltage Direct Current

I-P	Current-Power
I-V	Current-Voltage
I/O	Input-Output
LF	Low Frequency
LV	Low Voltage
LVAC	Low Voltage Alternating Current
LVDC	Low Voltage Direct Current
MVAC	Medium Voltage Alternating-Current
MVDC	Medium Voltage Direct Current
NPC	Neutral Point Clamped
PEC	Power Electronics Converter
PEM	Proton Exchange Membrane
PI	Proportional Integral
PV	Photovoltaic
PWM	Pulse Width Modulation
RES	Renewable Energy Sources
RMS	Root Mean Square
RTDT	Real-Time Digital Twin
SiC	Silicon-Carbide
SOE	Solid-oxide electrolyzer
SOF	Solid-Oxide Fuel
SPS	Single Phase Shift Modulation
SST	Solid-State Transformer
STATCOM	Static VAR Compensator
TPS	Triple Phase Shift Modulation
w.r.t	with respect to

Constants

$d_{\max}$	Upper bound of phase shift ratios

$d_{\min}$ Lower bound of phase shift ratios

l Lower bound

N_{s} Number of series-connected cells

N_{t} Turns ratio of transformer

R Universal gas constant, $\mathrm{JK^{-1}mol^{-1}}$

s, t, v, w Temperature dependent constants

u Upper bound

Variables

ϵ Deviation Threshold

η Converter Efficiency

ϕ Phase shift angle, rad

A_{elect} Electrode surface area, $\mathrm{m^2}$

A_{enc} Enclosed area, C

A_{eq} Equality constraint matrix

$a_{\mathrm{H_2O,KOH}}$ Water activity of KOH solution

A_{ineq} Inequality constraint matrix

b_{eq} Constant matrix for equality constraints

b_{ineq} Constant matrix for inequality constraints

$c(x)$ Inequality cost function

C_{A} Anode capacitance, F

$c_{\mathrm{eq}}(x)$ Equality cost function

C_{K} Cathode capacitance, F

C_{o} Output capacitance, F

D Pulse-width duty cycle

d Phase shift ratio

d_1 Inner phase shift ratio

d_2 Outer phase shift ratio

$d_{\mathrm{p(effective)}}$ Effective diameter of primary litz conductor, mm

$d_{\text{p(strand)}}$ Strand diameter of primary litz conductor, mm

$d_{\text{s(effective)}}$ Effective diameter of secondary litz conductor, mm

$d_{\text{s(strand)}}$ Strand diameter of secondary litz conductor, mm

F Faraday constant, C mol^{-1}

f_{sw} Switching frequency, Hz

$i_{\text{act(ano)}}$ Anode activation current, A

$i_{\text{act(cat)}}$ Cathode activation current, A

I_{D} Continuous drain current, A

$i_{\text{L(DPS)}}$ Inductor current during DPS, A

$i_{\text{L(peak)}}$ Peak inductor current, A

$i_{\text{L(rms)}}$ RMS inductor current, A

$i_{\text{L(SPS)}}$ Inductor current during SPS, A

$i_{\text{L(TPS)}}$ Inductor current during TPS, A

i_{L} Inductor current, A

i_{rect} Rectified secondary current, A

I_{sink} Gate driver sink current, A

I_{source} Gate driver source current, A

I_{stack} Average stack current, A

i_{stack} Stack current, A

i_{s} Secondary-side input current to H-LV, A

I_n Inductor state currents, A

k Voltage gain

L Series Inductance, H

l_{g} Air-gap length, mm

m Molar Concentration, $\text{mol}\,\text{kg}^{-1}$

N_{p} Number of primary turns

N_{sec} Number of secondary turns

P_{abs} Absolute pressure, bar

P_{H_2O} Vapor pressure of water, bar

P_{KOH} Vapor pressure of potassium hydroxide, bar

P_{op} Operating power set-point, W

P_o Output power, W

P_{stack} Stack Power, W

$P_{v(KOH)}$ Vapor pressure of KOH, bar

r Area-specific resistance of one of the electrolytic cells, Ωm^2

$R_{DS(on)}$ On-state resistance, Ω

R_d Lumped resistance, Ω

$R_{G(int)}$ Internal gate resistance, Ω

$R_{G(selected)}$ Selected external gate resistance, Ω

R_{int} Internal resistance of the electrolyzer cell, Ω

R_{load} Load resistance, Ω

R_{stack} Stack resistance, Ω

t Time instants, s

T_c Cell temperature, K

T_{disc} Discretization time-step, s

T_s Switching period, s

V^0_{rev,T_c} Temperature dependent reversible voltage, V

$v_{act(ano)}$ Anode activation potential, V

$v_{act(cat)}$ Cathode activation potential, V

V_A Output Voltage of H-HV Bridge, V

V_B Output Voltage of H-LV Bridge, V

v_c Capacitor voltage, V

V_{DC} Input DC link voltage, V

V_{DS} Drain-Source voltage, V

V_{int} Ohmic potential, V

v_L Voltage across series inductor, V

V_o	Converter output voltage, V
V_{rev}	Reversible cell voltage, V
V_{stack}	Average stack voltage, V
z	Number of moles of electrons transferred for one mol of product

List of Figures

List of Tables

SUMMARY

The increasing global emphasis on renewable energy stems from the need to reduce greenhouse gas emissions, enhance energy security, and promote sustainable development. Among various clean energy technologies, electrolysis has gained significant attention as an emission-free method for producing hydrogen, one of the most energy-dense fuels available. Unlike conventional hydrogen production methods that rely on the combustion of hydrocarbons and fossil fuels, electrolysis can be powered by RES, thereby enabling the production of green hydrogen.

Integrating hydrogen production systems with RES necessitates the use of PECs. However, designing PECs for electrolyzers presents unique challenges due to the distinct characteristics of electrolyzers, which are non-linear, low-voltage, and high-current DC loads. Their electrical behavior is influenced by both macro-level parameters such as temperature, pressure, and molar concentration, as well as micro-level electrochemical properties. Research examining electrolyzers from a power electronics perspective remains limited. In contrast, the DAB converter is a well-established and extensively studied DC/DC converter topology, widely used across diverse applications. Despite its popularity, little to no research has been conducted on its application in electrolysis. This thesis aims to bridge this gap by conducting application-oriented research on the design and operation of DAB converters for electrolyzer-based systems.

The design of power electronics requires a thorough understanding of the load characteristics. Chapter 2 lays the foundation by focusing on the fundamentals of electrolysis. It presents a static electrical model of an AEL based on established literature and extracts the information most relevant to power electronics without delving deeply into electrochemical details. The chapter then examines how variations in key electrolyzer parameters affect its electrical behavior. Insights from this analysis are used to formulate preliminary guidelines on the implications for DAB converter design.

Building on these results, Chapter 3 shifts focus to the mathematical modeling of the DAB converter. A high-accuracy GAM approach is proposed, with a step-by-step procedure involving minimal mathematical transformations compared to conventional methods. This model explicitly incorporates the impact of the turns ratio, N_t, and accounts for higher-order harmonics using the first M odd harmonics as input. Validation against conventional models, offline simulations, and real-time simulations demonstrates that the proposed GAM model accurately reconstructs transformer currents and provides a more precise representation of converter behavior.

The findings from Chapter 3 emphasize the importance of accurately modeling and controlling high-frequency transformer currents to ensure efficient power transfer. However, the basic DAB topology alone is insufficient for optimal electrolysis operation. Switching schemes or modulation strategies must be integrated to en-

hance performance. Chapter 4 addresses this by examining the interaction between the DAB converter and the electrolyzer. A comprehensive analysis of state-of-the-art modulation schemes namely, SPS, DPS, and TPS schemes is carried out in the context of electrolysis. Analytical expressions for transformer state currents and output power are derived for each operating mode. A peak current optimization scheme tailored to electrolysis is then introduced. Using this framework, the modulation strategies are compared across different power levels, and an optimal operating trajectory is proposed by selecting the most suitable modulation scheme and mode to minimize peak currents. This methodology is validated experimentally using a 1 kW, 20 kHz prototype for low-power electrolyzers and through MATLAB simulations for medium- and high-power systems.

Testing PECs for electrolyzers is inherently challenging due to the hazards associated with hydrogen production. Hydrogen gas is highly flammable, and faults in the connected converter can pose significant safety risks. Given that laboratory work involving hydrogen is often restricted for safety reasons, RTDT technology provides a safe and effective alternative for non-physical testing of power electronics for electrolysis. Chapter 5 presents the implementation of an RTDT for a DAB-electrolyzer system using the OP-4610XG real-time simulator. The chapter provides a detailed description of the modeling process, including steps for converting offline simulation models to real-time compatible implementations. Validation of the RTDT is performed using variations in stack temperature under closed-loop current control, demonstrating the accuracy and effectiveness of the proposed framework.

SAMENVATTING

De toenemende wereldwijde nadruk op hernieuwbare energie vloeit voort uit de noodzaak om de uitstoot van broeikasgassen te verminderen, de energiezekerheid te verbeteren en duurzame ontwikkeling te bevorderen. Onder de verschillende technologieën voor schone energie heeft elektrolyse veel aandacht gekregen als een emissievrije methode voor het produceren van waterstof. Dit is een van de meest energierijke brandstoffen die beschikbaar zijn. In tegenstelling tot conventionele waterstofproductiemethoden die afhankelijk zijn van de verbranding van koolwaterstoffen en fossiele brandstoffen, kan elektrolyse worden aangedreven door hernieuwbare energiebronnen (RES), waardoor de productie van groene waterstof mogelijk wordt.

Het integreren van waterstofproductiesystemen met RES vereist het gebruik van PEC's. Het ontwerpen van PEC's voor elektrolysers brengt echter unieke uitdagingen met zich mee vanwege de specifieke eigenschappen van elektrolysers, die niet-lineaire, laagspannings, en hoogstroom DC belastingen zijn. Hun elektrisch gedrag wordt beïnvloed door zowel macroparameters, zoals temperatuur, druk en molaire concentratie, als door micro-elektrochemische eigenschappen. Onderzoek dat elektrolysers vanuit een vermogenselektronica-perspectief bestudeert, is nog beperkt. Daarentegen is de DAB converter een gevestigde en uitgebreid bestudeerde DC/DC convertertopologie die veel wordt gebruikt in uiteenlopende toepassingen. Ondanks zijn populariteit is er nauwelijks onderzoek gedaan naar de toepassing ervan in elektrolyse. Dit proefschrift heeft tot doel deze kloof te overbruggen door toepassingsgericht onderzoek te doen naar het ontwerp en de werking van DAB-converters voor systemen op basis van elektrolysers.

Het ontwerp van vermogenselektronica vereist een grondig begrip van de belastingskarakteristieken. Hoofdstuk 2 legt de basis door zich te richten op de fundamentele principes van elektrolyse. Het presenteert een statisch elektrisch model van een AEL (alkaline electrolyzer) op basis van bestaande literatuur en haalt de informatie naar voren die het meest relevant is voor vermogenselektronica, zonder diep in te gaan op elektrochemische details. Vervolgens onderzoekt het hoofdstuk hoe variaties in belangrijke elektrolyserparameters het elektrisch gedrag beïnvloeden. De inzichten uit deze analyse worden gebruikt om voorlopige richtlijnen te formuleren voor de implicaties op het ontwerp van de DAB-converter.

Op basis van deze resultaten verschuift de focus in Hoofdstuk 3 naar de wiskundige modellering van de DAB-converter. Een GAM-aanpak met hoge nauwkeurigheid wordt voorgesteld, met een stapsgewijze procedure die minimale wiskundige transformaties vereist in vergelijking met conventionele methoden. Dit model neemt expliciet de invloed van de transformatieverhouding, N_{t}, op en houdt rekening met hogere-orde harmonischen door de eerste M oneven harmonischen als invoer te gebruiken. Validatie ten opzichte van conventionele modellen, offline simulaties en real-time simulaties toont aan dat het voorgestelde GAM-model transformatorstro-

men nauwkeurig reconstrueert en een nauwkeurigere weergave van het convertergedrag biedt.

De bevindingen uit Hoofdstuk 3 benadrukken het belang van nauwkeurige modellering en regeling van hoogfrequente transformatorstromen om een efficiënte energieoverdracht te waarborgen. De basis-DAB-topologie alleen is echter niet voldoende voor optimale elektrolysewerking. Schakelstrategieën of modulatietechnieken moeten worden geïntegreerd om de prestaties te verbeteren. Hoofdstuk 4 gaat hierop in door de interactie tussen de DAB-converter en de elektrolyser te onderzoeken. Er wordt een uitgebreide analyse uitgevoerd van de meest geavanceerde modulatietechnieken, namelijk SPS-, DPS- en TPS-schema's, in de context van elektrolyse. Voor elke bedrijfsmodus worden analytische uitdrukkingen afgeleid voor transformatorstromen en uitgangsvermogen. Vervolgens wordt een piekstroomoptimalisatieschema, specifiek afgestemd op elektrolyse, geïntroduceerd. Met dit kader worden de modulatietechnieken vergeleken bij verschillende vermogensniveaus, en wordt een optimaal bedrijfsverloop voorgesteld door de meest geschikte modulatietechniek en modus te selecteren om piekstromen te minimaliseren. Deze methode wordt experimenteel gevalideerd met een prototype van 1 kW en 20 kHz voor elektrolysers met laag vermogen, en via MATLAB-simulaties voor systemen met middelgroot en hoog vermogen.

Het testen van PEC's voor elektrolysers is van nature uitdagend vanwege de risico's die gepaard gaan met waterstofproductie. Waterstofgas is zeer brandbaar, en storingen in de aangesloten converter kunnen aanzienlijke veiligheidsrisico's opleveren. Aangezien laboratoriumwerk met waterstof vaak beperkt is om veiligheidsredenen, biedt RTDT-technologie een veilige en effectieve alternatieve methode voor het niet-fysiek testen van vermogenselektronica voor elektrolyse. Hoofdstuk 5 beschrijft de implementatie van een RTDT voor een DAB-elektrolyser-systeem met behulp van de OP-4610XG real-time simulator. Het hoofdstuk geeft een gedetailleerde beschrijving van het modelleringsproces, inclusief de stappen voor het omzetten van offline-simulatiemodellen naar real-time compatibele implementaties. Validatie van de RTDT wordt uitgevoerd door variaties in de stapeltemperatuur te testen onder gesloten-lusstroomregeling, waarmee de nauwkeurigheid en effectiviteit van het voorgestelde raamwerk worden aangetoond.

1

INTRODUCTION

1.1. BACKGROUND

Renewable energy has become increasingly important in recent years to reduce greenhouse gas emissions, improve energy security, and promote sustainable development. Many countries have been encouraging the implementation of renewable energy technologies, which could lead to the electrification of many end-use processes with power derived from clean sources [1]. In the Netherlands, the Klimaatakkoord aims at the reduction of CO_2 emissions by 49% in 2030 and 95% in 2050 relative to the 1990 levels [2]. This is well aligned with the targets set by the EU concerning the climate and, therefore, is within the framework of other international agreements, like the Paris Agreement [3, 4].

Green hydrogen is poised to become an essential component of net-zero emissions. It serves various pivotal roles. These include acting as a zero-emission transportation fuel and carbon-neutral raw material for industry [5, 6]. Additionally, it functions as a conduit for renewable energy. Lastly, it is a storage solution to stabilize fluctuating grids. Consequently, the technology for producing hydrogen without emissions is also gaining prominence and becoming central to the energy transition [7]. Currently, electrolysis stands as the predominant method for green hydrogen production [8]. This process involves separating water into hydrogen and oxygen through electricity from renewable energy sources. Currently, only 0.1% of global hydrogen production is derived from renewable energy sources powered by water electrolyzers and is classified as green [9].

According to the Global Hydrogen Review, 2022, global electrolyzer capacity could reach 134 GW by 2030 [10]. Due to its high energy density per unit mass, low weight, and easy electrochemical conversion, hydrogen can transport energy over long distances through pipelines or as liquid fuels such as ammonia on cargo ships [11]. In addition, hydrogen can store energy over extended periods, making it one of the few sustainable technologies capable of energy storage throughout the seasons, either in tanks or underground caverns [12].

1

1.1.1. ELECTROLYSIS

A simple diagram illustrating the process of water electrolysis is shown in Figure 1.1.

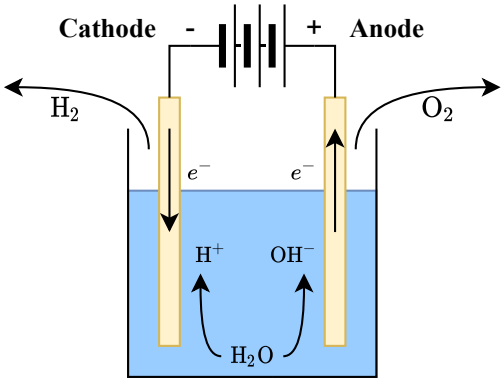

Figure 1.1: Water electrolysis

Pure water is a poor conductor of electricity. It is typically mixed with an acid or a base, such as sulfuric acid or caustic potash, which acts as an electrolyte to enhance its conductivity. This electrolyte facilitates ion movement between the anode and cathode.

As shown in the figure, the presence of the electrolyte increases water's conductivity, allowing the molecules to dissociate into protons (H^+) and hydroxyl (OH^-) ions. The protons migrate toward the cathode, while the negatively charged hydroxyl ions move toward the anode. At the cathode, protons accept electrons to form hydrogen gas, whereas hydroxyl ions lose electrons at the anode, creating oxygen gas. The following chemical reactions govern the overall process:

$$2\,H^+ + 2\,e^- \longrightarrow H_2 \qquad \text{(Cathode)}$$

$$2\,OH^- \longrightarrow \frac{1}{2}\,O_2 + H_2O + 2\,e^- \qquad \text{(Anode)}$$

1.1.2. STATE-OF-ART-ELECTROLYZER TECHNOLOGIES

Several types of electrolyzers are available in the market, each with distinct advantages and challenges. Figure 1.2 illustrates the state-of-the-art electrolyzer technologies.

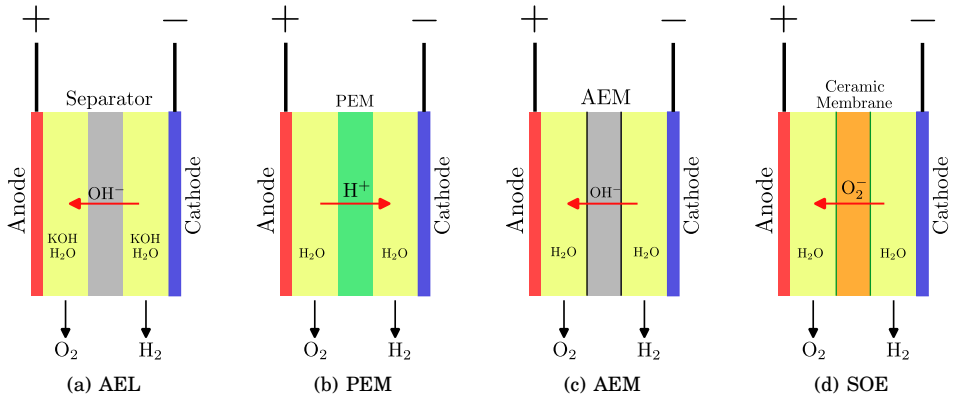

Figure 1.2: State-of-art electrolyzer technologies

AEL, illustrated in Figure 1.2(a), is the most established and widely used technology. They operate using a liquid electrolyte, typically potassium hydroxide, and have lower investment costs compared to other electrolyzer types [13]. However, they have a larger footprint and lower power density.

Figure 1.2(b) illustrates the PEM electrolyzers. They use a solid polymer electrolyte to conduct ions. General Electric developed the first PEM electrolyzer based on the solid porous electrode concept in the 1960s [14]. They are more compact and dynamic, requiring 20%-25% less space than AELs [15]. Despite their advantages, PEM electrolyzers rely on expensive noble metals like platinum and iridium, which increases their cost. However, technological advancements are expected to improve their efficiency and affordability in the coming years [16].

AEM electrolyzers combine features of both alkaline and PEM electrolyzers [17]. As shown in Figure 1.2(c), the structure is similar to PEM electrolyzers; they use a membrane to separate gases, but instead of conducting hydrogen ions, they facilitate the movement of hydroxide ions. This design eliminates the need for noble metals, allowing the use of low-cost catalysts such as cobalt, manganese, and nickel. The main challenge for AEM electrolyzers is the limited durability of their membranes, which must be improved for large-scale deployment [16].

SOE shown in Figure 1.2(d) operate at much higher temperatures than alkaline and PEM electrolyzers. These electrolyzers can work reversibly as fuel cells, converting hydrogen back into electricity [15]. The high-temperature operation enhances electrochemical reaction rates and reduces electrical energy consumption, leading to greater efficiency [16]. However, their high operating temperature results in long startup times and material degradation over time, which affects durability [18].

1

It is important to note that each of these electrolyzer technologies has its strengths and weaknesses, making them suitable for different applications and conditions. For this PhD. work, AELs will be utilized.

1.1.3. POWER ELECTRONICS AND ELECTROLYSIS

Power electronics interfaces are vital in integrating such RESs with electrolyzers. Typically, electrolyzers are interfaced with conventional AC distribution systems with either a single conversion stage (AC/DC) or an additional (optional) DC/DC conversion stage. Figure 1.3 showcases a typical architecture of electrolyzer power plants in AC and DC grids.

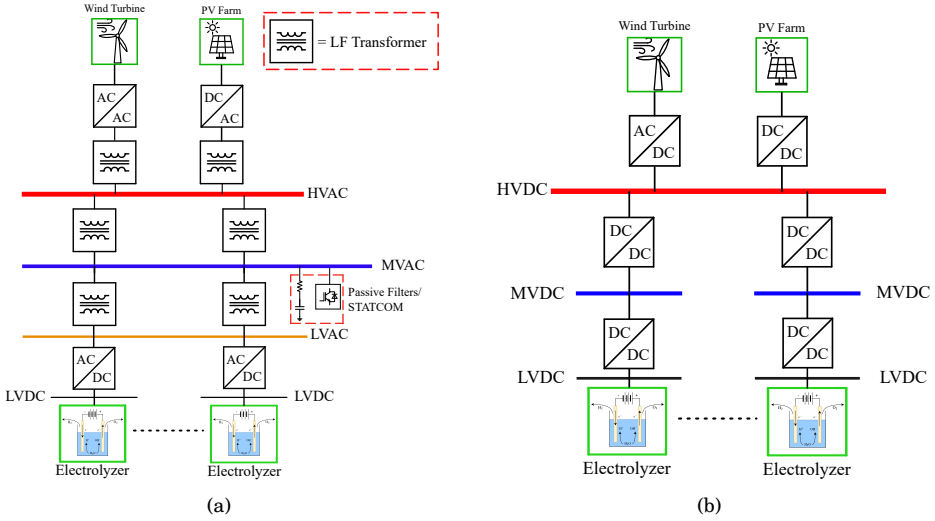

Figure 1.3: Electrolyzer power plant (a) AC grid-based and (b) DC grid-based.

Figure 1.3(a) showcases the conventional electrolyzer plant based on the MVAC system [19, 20]. This system consists of RES, such as wind turbines and PV farms, connected to the AC distribution system using AC/DC/AC back-back converters, respectively. The LF transformers step down the voltage for MVAC and LVAC distribution systems. Finally, the AC/DC converters interface the electrolyzer via an LVDC distribution system. It is important to note that the AC/DC conversion stage (rectifier) is thyristor-based.

Thyristor-based AC/DC power converters have long been the preferred solution for high-power AC/DC applications due to their robustness, high efficiency, and low cost [21–24]. Nevertheless, they also introduce power quality issues related to current harmonics and low power factor on the AC side when operated at a larger firing angle past the nominal operation point. As a result, harmonic filters/compensators such as active power filters or STATCOMs and/or passive filters are required to enhance/improve the power quality of the distribution grid. Furthermore, the requirement of bulky LF transformers increases the overall system costs [22]. Thyristor rec-

tifiers introduce a significant amount of current ripple on the DC side [25, 26]. Since the stack current of the electrolyzer controls the average hydrogen production rate [19], thyristor switch-based rectifiers have a detrimental impact on the electrolyzer operation.

Fig. 1.3(b) showcases a relatively similar electrolyzer system based on a DC distribution system. DC/DC converters have been utilized to interface several RESs with the grid and the HVDC grid with the MVDC grid. Finally, electrolyzers are interfaced with the MVDC grid using DC/DC converters.

Contrary to the system shown in Fig. 1.3(a), each DC/DC converter can be operated at a higher switching frequency, pushing the current harmonics to higher orders and minimizing them. The size of the high-frequency transformer and the filter capacitor in the case of isolated DC/DC converters can be significantly reduced. As a result, the DC-based electrolyzer power plant may exhibit significant potential compared to its AC counterpart.

Designing such power electronics interfaces is not straightforward for electrolyzer systems scaled up to an industrial level. Given the nature of electrolysis, it should be capable of operating at low voltage and extremely high DC current. DC-DC converters designed for electrolyzers must meet several requirements, which include [27, 28]: High efficiency over a wide operating range (significant DC voltage gain), high power density, lower EMI, smaller output current ripple, and low cost. In addition to the listed requirements, the converter under design must incorporate galvanic isolation conforming to ISO:22734:2020 and ISO:19880-1:2020 standards. Due to the obligatory requirement of galvanic isolation, isolated DC-DC converters are the prime candidates.

Figure 1.4 presents metrics related to publications for power electronics in electrolyzer applications.

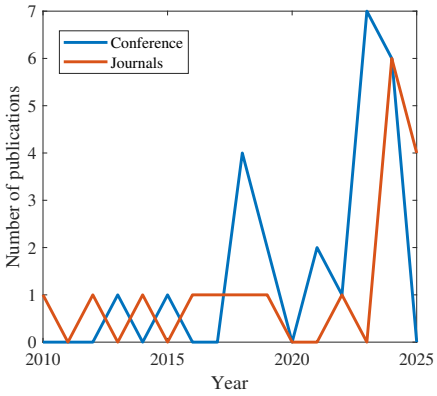

Figure 1.4: Research published on IEEE Xplore, Elsevier, and Wiley related to power electronics for electrolyzer applications as of 23 May 2025. Publications contributing to this thesis are excluded.

As the figure indicates, while interest in this area has grown in recent years, the overall research volume remains relatively limited. Among the existing literature, a

subset of studies has focused on proposing new converter topologies, analyzing converter behavior, or applying established converter designs to electrolyzer or reversible systems. These contributions are of particular relevance to this thesis.

Table 1.1 lists key references (conference and journal publications) where converter topologies are proposed, analyzed, or employed in the context of electrolyzer or reversible systems.

Table 1.1: Converter topologies proposed/analyzed for electrolyzer or reversible system applications between 2010-2025.

References	Application (Electrolyzer/Fuel Cell /Both)		Galvanic Isolation (between converter I/O)	Grid Integration	
	Electrolyzer	Fuel Cell		DC	AC
[29]	✓		✓	✓	
[30]	✓		✓		
[31]	✓			✓	
[32]	✓			✓	
[33]	✓	✓	✓	✓	
[34]	✓	✓	✓	✓	
[35]	✓	✓	✓		✓
[36]	✓				✓
[37]	✓				✓
[38]	✓		✓		
[39]	✓		✓		
[40]	✓			✓	
[41]	✓				
[42]	✓				✓
[43]	✓		✓	✓	
[44]	✓				
[45]	✓				
[46]	✓		✓	✓	✓
[47]	✓		✓		
[48]	✓		✓		✓
[49]	✓		✓	✓	
[50]	✓		✓	✓	
[51]	✓				
[52]	✓		✓	✓	
[53]	✓				
[54]	✓				
[55]	✓				✓
[56]	✓				✓
[57]	✓		✓	✓	

From Table 1.1, the following key observations can be made:

- There is a growing trend toward integrating DC grids with electrolyzers using power electronics, as evidenced by 12 publications in contrast to 8 publications focusing on AC grid integration since 2010.

- Half of the reported studies incorporate galvanic isolation between the converter input and output. In contrast, the remaining works implement isolation primarily between the grid and the converter input.
- Of the 30 studies reviewed, only two studies ([33, 47]) have employed the DAB isolated DC-DC converter topology for electrolyzers over the past 15 years, indicating limited research for this application.

Despite its widespread use, application-oriented research of DAB converters for electrolyzer systems remains notably scarce, as will be discussed in the forthcoming section. From the perspective of electrolysis, the DAB converter offers several compelling advantages, such as inherent soft-switching capability, galvanic isolation between the I/O via an HF transformer, flexibility to achieve series-parallel configurations, and high efficiency across a wide operating range [58, 59], making it a powerful candidate for integrating DC grids with electrolyzer systems.

1.2. KEY TECHNICAL CHALLENGES

In this work, four key technical challenges were identified.

1.2.1. IMPACT OF ELECTROLYZER PARAMETERS ON PECS

PEC design requires insights into the electrical load to which it would be connected. These insights help select the right semiconductor switches, ratings, switching schemes, etc. In this case, information regarding the load's electrical characteristics is important. Unlike most standard electrical loads, electrolyzers exhibit unique properties and behavior. The behavior of standard electrical loads depends on material properties and dimensions. However, the properties of electrolyzers, in addition to their physical properties, also depend on their electrochemical properties.

Studies on electrolyzers have mainly been carried out from the perspective of thermodynamics and electrochemistry. In [60], a model for alkaline electrolysis cells was developed considering the influence of temperature, electrode/diaphragm spacing, and electrolyte concentration on the process thermodynamics and electrochemistry. [61] presented an SOE model based on energetic, exergetic, and electrochemical analyses. A detailed parametric study at the single-cell level assessed the effects of operating parameters—such as temperature, pressure, steam fraction, and current density—on cell potential and performance. For AEM electrolyzers, [62] developed a mathematical model capturing equivalent impedance, electrothermal behavior, and power regulation. A corresponding electrothermal simulation was built using MATLAB/Simulink. [63] explored the influence of charge transfer coefficients and exchange current density on PEM electrolyzer polarization, performance, and operation. In [64], an equivalent electrical circuit model was presented to replicate the dynamic behavior of PEM electrolyzers under rapid current changes. An adaptive static-dynamic model was introduced and validated using a 400 W commercial PEM electrolyzer. [65] presents a holistic perspective on improving PEMs, with a focus on enhancing anode performance and reducing costs. It addresses catalyst materials,

electrode structure, and transport layers as an integrated design challenge.

Recent works include [66], which presents the modeling of an electrolyzer with an experimental setup and showcases the static-dynamic behavior. However, the study only takes into account the stack temperature. [67] presented a detailed thermodynamic and electrochemical analysis of alkaline electrolyzers under varying operating conditions to optimize hydrogen production. It examined the influence of parameters such as temperature, current density, electrode kinetics, and electrolyte thickness on cell voltage. A dynamic, parameter-adjustable mass and energy balance model was proposed in [68] for an industrial AEL plant. Developed using white-box coding and a practical set of fixed parameters, the model was validated against an industrial plant with similar power and pressure specifications. Electrochemical, mass flow, and thermal behaviors were compared to ensure accuracy and adaptability for future plant optimization. A unified multi-physics model was proposed in [69] for PEM, AEL, and SOE electrolyzers, incorporating current density distribution, single and two-phase flow, mass transfer, and temperature effects to compare I-V characteristics, efficiency, and part-load performance. [60–69] provide valuable insights regarding the electrochemical and thermodynamic properties of electrolyzers, but lack the insights from the perspective of a power electronics design.

Electrolyzers behave differently depending on conditions like temperature and pressure, which change their I-V characteristics. Electrical models of electrolyzers are already established, but what is still unclear in the literature is how these changes affect the design of the power electronics that drive the electrolyzer. In other words, converter ratings, efficiency, and control may all be impacted by these operating variations, yet this link has not been fully explored.
Therefore, the challenge is:
To investigate the impact of electrolyzer parameters on its electrical characteristics (voltage and current), and correlate this impact to the design of the DAB converter.

1.2.2. SIMPLIFIED AND ENHANCED DAB CONVERTER MODELING

Control objectives should be defined based on the application [70] to operate a power converter. The foundation for designing these control objectives and for the overall control strategy of a power electronics converter lies in understanding its mathematical modeling. These models are crucial for comprehending, analyzing, and designing power electronics systems. They help anticipate performance, refine designs, and devise effective control strategies, ensuring the converters function optimally within their intended applications.

In [71], a novel GAM approach was proposed for a phase-shift controlled bidirectional DAB converter in the continuous time domain. The method utilizes switching frequency terms in the Fourier series of the state variables. However, this modeling approach only considers the contribution of the fundamental component for modeling the converter dynamics and transformer current. Three terms (N=0 and N=±1) are

considered for the modeling approach. However, with the contribution of these three terms, a sinusoidal transformer current is obtained, which does not represent the actual current within a DAB converter. Furthermore, only the frequency response of the proposed model has been compared with other modeling approaches. The same authors in [72] introduced a GAM for DC subsystems in SSTs with DAB converters, assuming a unity turns ratio. While voltages and currents are modeled accurately, transformer currents are not due to FHA limitations. Moreover, the authors reported that extending GAM beyond the fundamental component increases complexity. In [73], the average modeling method was applied to general modulation strategies such as DPS, EPS, and TPS using the technique proposed in [71]. A method was proposed to minimize the error due to truncating the Fourier series at the fundamental harmonics. However, an additional correction factor was required to consider the copper losses in the transformer.

Other modeling approaches were also used to model the converter. A continuous-time full-order model retaining high-frequency information of the system was proposed in [74]. Using the Toeplitz operator, a single equation obtained state equations for every harmonic of a given state variable. [75] presented a per-unit small-signal model for DAB converters under TPS modulation, incorporating the voltage conversion ratio. However, it only includes the fundamental frequency component and omits transformer current dynamics. Authors in [76] present a method of constructing accurate and scalable models of DC distribution systems containing multiple DAB converters. The reconstruction of DAB transformer currents has been discussed in this work. However, this approach utilizes Fourier and inverse Laplace transformations, making the rebuilding steps complex and challenging to understand.

Recent works include a unified numerical model [77] using FFT in the frequency domain with time-domain conversion, effectively capturing transformer currents. However, it does not account for the turns ratio, limiting practical applicability. A simplified discrete-time model [78] was proposed using matrix exponential and iterative simplification. It includes both transformer currents and turns ratio. However, its simplicity compromises transformer current accuracy compared to more detailed models. A transconductance model [79] was proposed for SPS and DPS control based on first-order system dynamics, capturing control-to-output voltage behavior in time and frequency domains. However, it neglects transformer currents, which are critical in DAB converters.
Therefore, the challenge is:
To develop a step-by-step modeling approach for the DAB converter that goes beyond conventional methods, allowing accuracy to be adjusted as needed with minimal mathematical transformations.

1.2.3. APPLICATION-SPECIFIC CONVERTER EVALUATION FOR ELECTROLYSIS

It is important to compare the usage of this topology in various applications apart from electrolysis. Table 1.2 provides application-based classification of prior DAB

converter research.

Table 1.2: Application-Based Classification of Prior DAB Converter Research

Reference	DC grids	EV charging	SST	Aerospace	ESS	Electrolysis	Converter Analysis
[80–86]	✓						
[87]		✓					✓
[59, 88–95]		✓					
[96–99]			✓				
[100, 101]				✓			
[102–104]					✓		
[105]					✓		✓
[47, 49]						✓	

DAB converters are utilized extensively across various applications, including DC grids, EV charging, SSTs, aerospace, and ESS. While these areas are well represented in the literature, only two works in the past 15 years have specifically proposed DAB converters for electrolyzer applications, as concluded in Section 1.1.3.

Studies reported in Table 1.2 can be broadly categorized as:

- Studies that utilize a DAB converter within a larger system without in-depth application-specific analysis.
- Studies that both propose a DAB converter topology and carry out detailed converter-level analysis tailored to the application.

Despite the widespread deployment of DAB converters in EV charging and DC grid applications, there is limited converter-level analysis carried out. For instance, only one study has compared modulation strategies for EV and ESS, while no such studies exist for electrolysis. Regarding the two reported studies of DAB converters with electrolyzers, [33] implemented a partial parallel DAB converter with variable voltage gain for an SOE/SOF system, validated using a 0.53 kW prototype. On the other hand, [47] proposed a SiC-based 48 V-380 V DAB converter for energy transfer to an electrolyzer in a green hydrogen system, employing a closed-loop PI controller with corresponding design guidelines. Both these works lack converter-level analysis from the electrolysis perspective.

Therefore, the challenge is:

To conduct a converter-level investigation of DAB topology in the context of electrolysis.

1.2.4. EVALUATION OF POWER ELECTRONICS FOR ELECTROLYSIS

Electrolysis requires low voltage and extremely high current for its optimal operation [106]. Therefore, the converter under design must be evaluated for different test conditions before integrating the converter with the electrolyzer system.
Testing and evaluation of power electronics for electrolysis imposes several challenges, such as:

- Safety concerns associated with hydrogen gas. Since most power supplies for electrolyzers are integrated within the chassis, any abnormal behavior or fault exhibited by the converter during the testing phase might trigger hazardous conditions.
- Access to real electrolyzers and their electrical characteristics is restricted due to proprietary concerns from manufacturers.
- As an academic/research institution, procurement of electrolyzers is restricted due to regulatory and safety constraints.

As a result, a framework to evaluate DAB converters for electrolyzer systems without a physical system can be beneficial for researchers who do not have access to electrolyzers, especially researchers working in technical universities.

An elegant tool to evaluate the performance of a designed PEC for the electrolyzer is with the help of DTs. The definition of a DT is volatile and depends on the application. In this thesis, a DT is defined as a virtual representation of a physical PEC, including its characteristics, behavior, and performance [107].

Recently, authors in [108] reviewed the integration of DT technology in power electronics systems, focusing on real-time synchronization, accurate modeling, and data interaction. It explores four DT modeling techniques based on: mechanism, simulation, multi-physics, and data.

Table 1.3: Application-based classification of prior DT implementation (Does not include publications of this PhD).

References	Aerospace	Power Systems	EV	Fuel Cells	Power Electronics	Health Care	Electrolysis
[109]	✓						
[110–113]		✓					
[114]			✓				
[115]			✓		✓		
[116, 117]				✓			
[118–132]					✓		
[133]		✓			✓		
[134–137]					✓	✓	
[138]							✓
[139, 140]						✓	
[141]					✓		✓

In this thesis, a simulation model-based DT would be a suitable candidate. Simulation model-based DTs are virtual representations of physical systems that replicate their behavior under various conditions. Simulation models enable the virtual testing of scenarios that would be difficult or costly to implement in the real world. This is the case for electrolyzer applications, especially in the early stages of development and before hardware testing [108]. Table 1.3 provides reports on literature related to DTs based on application. From Table 1.3, the following key observations can be made:

- The application of DTs has been widely used in power electronics, with over 14 works reported since 2010. Some work has been carried out at the intersection of power systems, health care, and EVs.
- Only one study on DTs has been reported for electrolysis. Similarly, only one study in DTs has been reported to have an intersection of power electronics with electrolysis, indicating limited application of DTs within this domain.

Table 1.4: Topologies utilized within a subset of studies conducted for DTs in the power electronics domain from Table 1.3

Reference	Topology	Intermediate Conversion Stage? (part of the converter topology)
[118]	1-ϕ AC/DC + 3-ϕ DC/AC converter	No
[119]	3-ϕ DC/AC converter and DC/DC boost converter	No
[120, 128]	3-ϕ AC/DC converter	No
[121, 129, 130]	DC/DC buck converter	No
[122, 124]	1-ϕ DC/AC converter	No
[123]	T-type 3-level AC/DC converter	No
[125]	1-ϕ AC/DC converter	No
[126]	5-level ANPC multilevel converter	No
[127]	3-ϕ NPC converter	No
[131]	DC/DC synchronous buck converter and 3-ϕ DC/AC converter	No
[132]	DC/DC boost converter	No

Table 1.4 reports topologies utilized within the subset of studies conducted for DTs in the power electronics domain from Table 1.3. The insights from Table 1.4 are particularly relevant to this PhD work. Studies on DT, either purely for power electronics or the intersection of power electronics with electrolysis, have utilized power electronics topologies that consist of only one power conversion stage. No studies on DTs reported using power electronics converter topologies containing more than one conversion stage.
Therefore, the challenge is:
To develop a real-time digital twin test bench for analyzing DAB converters for electrolyzers.

1.3. RESEARCH OBJECTIVES AND QUESTIONS

The main research objective of this doctoral thesis is as follows:

Conduct application oriented studies of DAB converter from the persepective of electrolysis.

To achieve this objective, the research questions to be answered in this doctoral thesis are as follows:

1. *How do electrolyzer parameters influence its electrical behavior from a power electronics design perspective?*
    - Study the state-of-the-art electrolyzer technologies. Select the most widely used and mature technology.
    - Identify key electrolyzer parameters that can change during operation.
    - Using the identified electrolyzer parameters, conduct sensitivity analysis to investigate their impact on its electrical characteristics.
    - Co-relate the findings of the sensitivity analysis to determine preliminary consequences on the DAB design.
2. *How can the GAM of the DAB converter be simplified to achieve accurate transformer current reconstruction with minimal mathematical complexity?*
    - Study existing GAM approaches for modeling the DAB converter. Identify the drawbacks of these approaches.
    - Formulate a step-by-step methodology to develop a GAM of a DAB converter that can achieve high accuracy with minimal mathematical complexity.
    - Validate the developed GAM model with offline and real-time simulations.
3. *How do different state-of-the-art modulation strategies affect the performance of the DAB converter during electrolysis? How can the operation of the DAB converter be optimized for electrolysis?*
    - Study the state-of-the-art modulation strategies for the DAB converter.
    - Conduct converter-level analysis for the considered modulation strategies for electrolysis.
    - Perform optimization for electrolyzers of different power levels for the considered modulation strategies and identify which modulation scheme performs the best.
    - Develop an algorithm that determines the optimal operating trajectory for the converter for electrolysis.
    - Perform experimental validation of the optimization and simulation results using a lab-scale prototype.

1

4. *How can a DAB-electrolyzer system be implemented and evaluated using an RTDT?*
    - Study the real-time simulation architecture of OPAL-RT real-time simulators.
    - Convert the offline simulation model of the DAB-electrolyzer system to the real-time simulation environment.
    - Evaluate and validate the developed RTDT model against different stack temperature test cases during electrolysis.

1.4. STRUCTURE OF THE THESIS

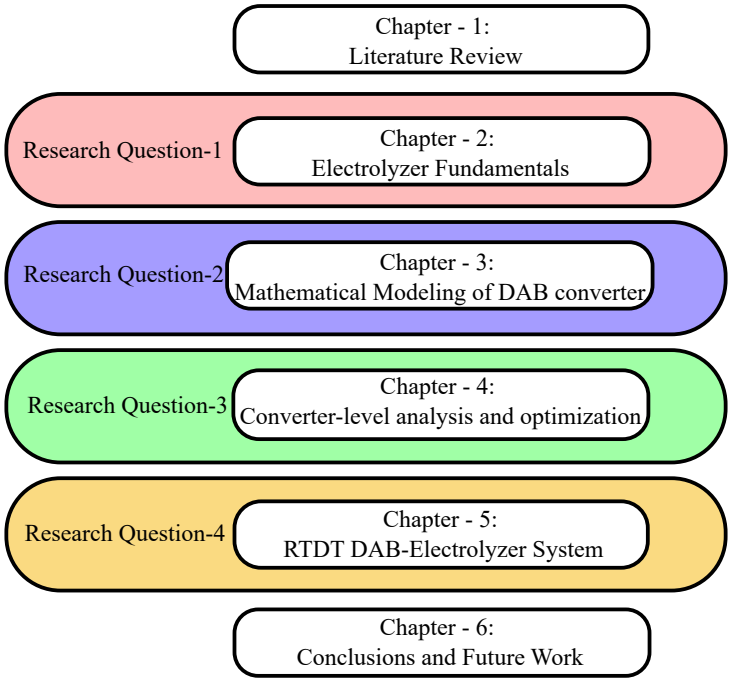

Figure 1.5: Structure of this thesis.

The structure of the thesis has been illustrated in Fig. 1.5. **Chapter-2** investigates the electrical behavior of electrolyzers. **Chapter-3** introduces a high-accuracy GAM for the DAB converter, validated through offline and real-time simulations. **Chapter-4** provides a converter-level analysis of the DAB converter by evaluating various state-of-the-art modulation strategies in electrolysis. Modulation schemes are further optimized and validated using offline simulations and a 1 kW lab-scale prototype. **Chapter-5** focuses on implementing RTDT setup of a DAB-electrolyzer system. **Chapter-6** concludes the thesis by summarizing the key findings and outlining directions for future research.

2

ELECTROLYZER FUNDAMENTALS

The design of power electronics often requires sufficient knowledge about the connected load, as the electrical load dictates electrical characteristics on the basis of which the choice of operating modes, component sizing/selection, etc, is determined. This chapter presents the fundamentals of electrically modeling an electrolyzer. The electrical modeling, although based on an existing modeling approach, has been modified for an AEL. Using this model, a sensitivity analysis was conducted on this electrical model to study how electrolyzer parameters have an impact on its electrical behavior.

Chapter partially published in R. S. Deshmukh, G. Rituraj, P. Bauer and H. Vahedi, "Real-time digital twin implementation of power electronics-based hydrogen production system," in *Energy Reports*, vol. 13, pp. 5006-5015, 2025.

2.1. INTRODUCTION

Designing power electronics starts with understanding the electrical load it will be driving. Without this knowledge, it is difficult to determine the right design considerations, operating modes, or control strategies.

2

In this chapter, the fundamentals of electrolysis are introduced with a focus on what matters for converter design:

- Electrolysis is fundamentally an electrochemical process. While a detailed study of its chemistry can provide deeper insight, the main requirement is the electrical load profile of the electrolyzer as far as the power electronics are concerned. To capture this, an established model from the literature is used to represent the electrical behavior of an AEL.
- As discussed in Section 1.2.1, the operation of an electrolyzer depends on several parameters that affect its performance at both macro and micro scales. Four parameters are examined here, and their effects on the voltage-current characteristics are analyzed.
- Based on this analysis, preliminary insights relevant to the design of a Dual Active Bridge (DAB) converter are identified.

2.2. ELECTRICAL MODELING

From a PEC design perspective, the relevant electrical parameters of an electrolyzer are the stack voltage and current. In the literature, several modeling approaches [142–145] have been proposed. The approach proposed in [144] has been used in this work.

2.2.1. ASSUMPTIONS

- The diffusion potential is negligible.
- The experimentally determined parameters provided in [144] that are crucial for the modeling process are considered the same for the electrolyzer to be modeled.

The stack voltage of an electrolyzer constitutes four potentials: reversible stack potential, activation potential, ohmic potential, and diffusion potential.

2.2.2. REVERSIBLE POTENTIAL

Equation (2.1) defines the reversible stack potential. It exhibits the thermodynamic phenomena in the electrolysis reaction. Mathematically, the reversible cell voltage is given by the Nernst equation [144],

$$V_{\text{rev}} = N_{\text{s}} \left(V^{0}_{\text{rev,T}_{\text{c}}} + \frac{R T_{\text{c}}}{zF} \log \left(\frac{(P_{\text{abs}} - P_{\text{v(elec)}})^{1.5}}{a_{\text{we}}} \right) \right) \tag{2.1}$$

As observed in (2.1), the reversible cell voltage is divided into two types:

- Temperature dependent cell potential at a reference standard pressure (1 bar), V^0_{rev,T_c}.
- Logarithmic dependence, accounting for the pressure dependence and non-idealities of the process due to the vapour pressures of H_2 and O_2.

where,

$$P_{H_2O} = \exp\left(81.618 - \frac{7699.7}{T_c} - 10.9\log(T_c) + (9.589 \times 10^{-3}) \cdot T_c\right)$$

$$P_{KOH} = \exp(2.302 \cdot a + b \cdot \log(P_{H_2O}))$$

$$a_{we} = \exp\left((-51.92 \times 10^{-3}) \cdot m + (3.3 \times 10^{-3}) \cdot m^2 + \left(\frac{3.3177 \cdot m - 2.131 \cdot m^2}{T_c}\right)\right)$$

$$a = -0.0151 \cdot m - (1.6788 \times 10^{-3}) \cdot m^2 + (2.2588 \times 10^{-5}) \cdot m^3$$

$$b = 1 - (1.2062 \times 10^{-3}) \cdot m + (5.6024 \times 10^{-4}) \cdot m^2 - (7.8228 \times 10^{-6}) \cdot m^3$$

2.2.3. ACTIVATION POTENTIAL

Activation potential refers to the interaction of electrolyte (chemical species) and electrodes via electrical charges. Fig. 2.1 shows this interaction in detail.

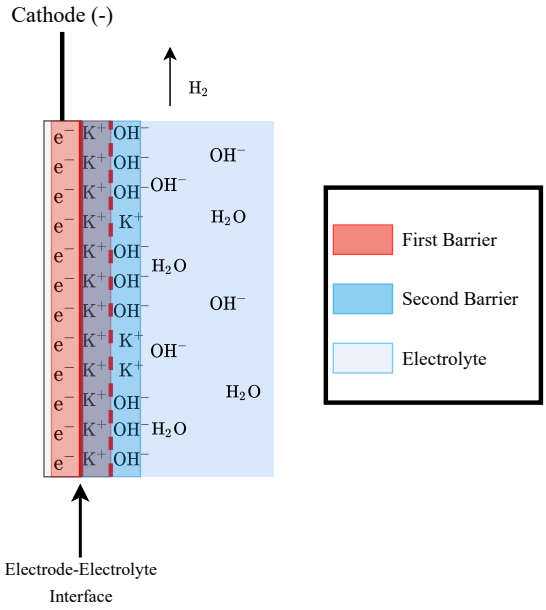

Figure 2.1: Double Layer Effect

In this figure, the electrons are received by the electrodes from the power supply, and therefore, they begin to accumulate. As a result of this concentration, potassium ions (positive polarity) get attracted towards this electrode. A condition is reached where the charge on the electrode is compensated by an equal amount of charge provided by the potassium ions. This process leads to the formation of the double-layer effect [146]. The double layer shown here represents a parallel plate capacitor with the electrode-electrolyte interface as the dielectric medium connected in parallel with a resistance similar to an RC network. In continuous direct current operation, the activation phenomena are represented in the form of a non-linear voltage. The activation potential of both electrodes can be represented by the modified Tafel equations [144]. Equations (2.2) and (2.3) define the electrode activation potentials for anode and cathode, respectively.

$$v_{\text{act(A)}} = sN_{\text{s}} \log\left(\frac{i_{\text{act(A)}}}{t} + 1\right) \tag{2.2}$$

$$v_{\text{act(K)}} = vN_{\text{s}} \log\left(\frac{i_{\text{act(K)}}}{w} + 1\right) \tag{2.3}$$

where,

$$s = s_1 + s_2 T_{\text{c}} + s_3 T_{\text{c}}^2$$
$$t = t_1 + t_2 T_{\text{c}} + t_3 T_{\text{c}}^2$$
$$v = v_1 + v_2 T_{\text{c}} + v_3 T_{\text{c}}^2$$
$$w = w_1 + w_2 T_{\text{c}} + w_3 T_{\text{c}}^2$$

s, t, v, w are determined with the help of curve-fitting and experimental data in contrast to the traditional exchange current density parameter due to the significant variation in the numerical values used in the literature [63]. $i_{\text{act(A)}}$ and $i_{\text{act(K)}}$ are activation currents for anode and cathode, respectively.

2.2.4. OHMIC POTENTIAL

Finally, (2.4) refers to the ohmic potential, which can be defined as the voltage drop across the internal resistance (electrolyte) between the two electrodes. This potential is imposed on the cell due to the ohmic resistance offered by the electrolyzer cell, which is a hindrance to the path of current. This is represented by a temperature-dependent resistance [144].

$$V_{\text{int}} = N_{\text{s}} i_{\text{stack}} R_{\text{int}} = N_{\text{s}} i_{\text{stack}} \frac{r}{A_{\text{elect}}} \tag{2.4}$$

where, R_{int} is the internal resistance of the electrolyzer cell, Ω. r is area specific resistance, Ωm^2. It is determined from the experimental static I-V characteristics at different temperatures of the electrolyzer with the help of the curve-fitting technique. The resistance value can therefore be calculated,

$$r = r_1 + r_2 T_{\text{c}} + \frac{r_3}{T_{\text{c}}} + \frac{r_4}{T_{\text{c}}^2}$$

2.2.5. STACK VOLTAGE

The total stack voltage of an AEL can be obtained as the sum of the potentials mentioned in (2.1) - (2.4).

$$v_{\text{stack}} = V_{\text{rev}} + v_{\text{act(A)}} + v_{\text{act(K)}} + V_{\text{int}} \tag{2.5}$$

The equivalent circuit highlighting each potential is illustrated in Fig. 2.2

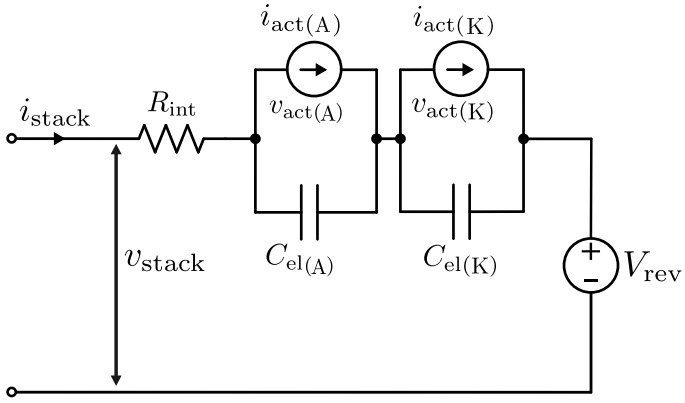

Figure 2.2: Electrical model of an AEL

2.2.6. RESULTS

Table 2.1 and 2.2 showcase the basic specifications of the electrolyzer to be modeled, and the experimentally determined parameters obtained from [144] utilized for this modeling process, respectively.

Table 2.1: Electrolyzer Specifications

	Value		**Value**
Electrolyte	KOH 30% wt.	A_{elect}	300 cm^2
m	7.64 mol kg^{-1}	P_{abs}	5 bar
T_{c}	15 °C	P_{stack}	10 kW
N_{s}	36	i_{stack}	148 A

Table 2.2: Experimental data from [144]

Parameters	Value	Parameters	Value
r_1	$59.5482 \times 10^{-6}\,\Omega\mathrm{m}^2$	t_2	$-2.4601 \times 10^{-3}\,\mathrm{A}^{\circ}\mathrm{C}^{-1}$
r_2	$-340.8224 \times 10^{-9}\,\Omega\mathrm{m}^2\,^{\circ}\mathrm{C}^{-1}$	t_3	$52.1217 \times 10^{-6}\,\mathrm{A}^{\circ}\mathrm{C}^{-2}$
r_3	$-106.9708 \times 10^{-6}\,\Omega\mathrm{m}^2\,^{\circ}\mathrm{C}$	v_1	$110.3623 \times 10^{-3}\,\mathrm{V}$
r_4	$2.7075 \times 10^{-3}\,\Omega\mathrm{m}^2\,^{\circ}\mathrm{C}^2$	v_2	$-1.6466 \times 10^{-3}\,\mathrm{V}^{\circ}\mathrm{C}^{-1}$
s_1	$25.2300 \times 10^{-3}\,\mathrm{V}$	v_3	$22.8382 \times 10^{-6}\,\mathrm{V}^{\circ}\mathrm{C}^{-2}$
s_2	$-234.0338 \times 10^{-6}\,\mathrm{V}^{\circ}\mathrm{C}^{-1}$	w_1	$45.7027\,\mathrm{A}$
s_3	$3.1832 \times 10^{-6}\,\mathrm{V}^{\circ}\mathrm{C}^{-2}$	w_2	$0.7781\,\mathrm{A}^{\circ}\mathrm{C}^{-1}$
t_1	$54.6185 \times 10^{-3}\,\mathrm{A}$	w_3	$-10.5743 \times 10^{-3}\,\mathrm{A}^{\circ}\mathrm{C}^{-2}$
$C_{\mathrm{el(A)}}$	637.5 mF	$C_{\mathrm{el(K)}}$	30.7 mF

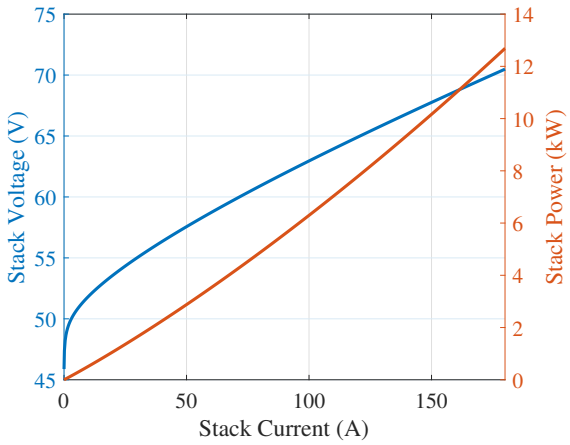

Figure 2.3: Electrical characteristics of 10 kW AEL

Fig. 2.3 showcases the I-V and I-P characteristics of a 10 kW AEL operating at a stack temperature of 15 °C. The characteristics indicate a wide operating range of the electrolyzer. In addition to the stack temperature, other parameters govern the operation of an electrolyzer that, in turn, may also impact its electrical behavior. These parameters include stack pressure, molar concentration of the electrolyte, electrode cross-sectional area, and activation current. It has been proven experimentally in [144] that stack pressure does not impact the electrolyzer's electrical characteristics; therefore, this parameter will not be considered in this work. It is essential to conduct a sensitivity analysis on the electrolyzer model to study the effect of these parameters on the electrical characteristics.

2.3. SENSITIVITY ANALYSIS

Fig. 2.4(a)-2.4(d) shows the impact on the electrical characteristics for variation in stack temperature, molar concentration, electrode cross-sectional area, and activation current, respectively.

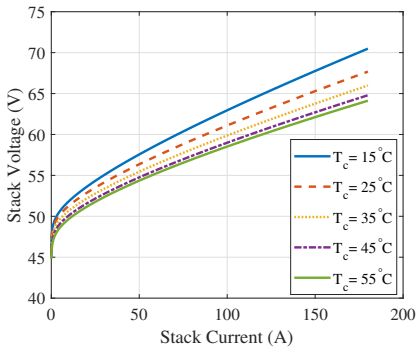

(a) Effect of stack temperature

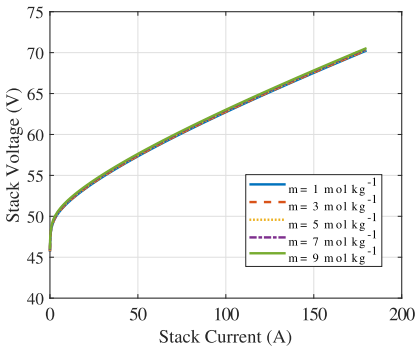

(b) Effect of molar concentration of electrolyte

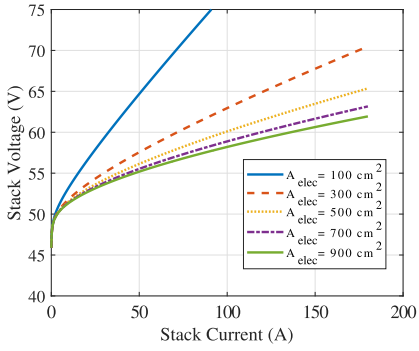

(c) Effect of electrode surface area

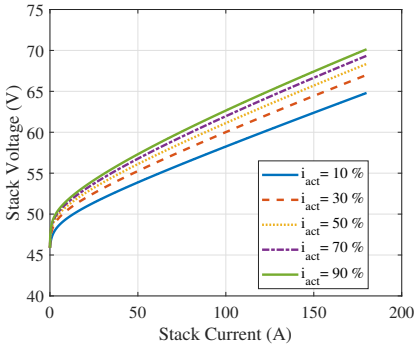

(d) Effect of activation current

Figure 2.4: Sensitivity analysis conducted on a 10 kW electrical model of an AEL

- The stack temperature shifts the characteristics along the stack voltage axis, as shown in Fig. 2.4(a). A higher stack temperature accelerates the rate of chemical reaction, thereby improving the hydrogen yield. While higher stack temperature enhances the hydrogen production rate, it decreases the stack voltage and increases the stack current for the same operating power.

- Little or no variation is observed from the electrical perspective in case of variation in the molar concentration of the electrolyte, as illustrated in Fig. 2.4(b). However, a higher molar concentration leads to a more corrosive electrolyte, which can degrade the electrodes and the inner body of the electrolyzer. In this case, the power electronics design is unaffected, and the impact of this param-

eter is only on the electrolyzer.

- The choice of electrode cross-sectional area directly affects the internal resistance per (2.4). While a smaller electrode surface area increases the stack voltage for a given stack current, as depicted in Fig. 2.4(c), it leads to considerable internal resistance (higher ohmic potential), decreasing the electrolyzer's efficiency as the hydrogen production rate is dictated by the stack current. On the other hand, a large cross-sectional area of the electrode leads to a decrease in stack voltage for a given stack current; however, this improves the electrolyzer's efficiency. The size of the electrolyzer also limits the cross-sectional area of the electrode.

- Activation current is required to overcome the double-barrier effect formed due to electric charge transfer between the chemical species and the electrodes. Fig. 2.4(d) shows curves for various percentage loading of activation current. A lower activation current leads to a lower stack voltage as it is more difficult to overcome the double-barrier effect which is necessary to kick-start the process.

2.4. CONSEQUENCES ON DAB DESIGN

Based on the sensitivity analysis conducted in Section 2.3 and Fig. 2.5, the following preliminary insights can be determined from the perspective of DAB converter design:

- Operating at a higher stack temperature will require operating at a lower stack voltage for the same operating power. This results in an increase in primary-secondary turns ratio of the HF transformer and the requirement of a larger conductor cross-sectional area of the secondary winding. This may complicate transformer design.

- A higher stack temperature would lead to higher stack current that necessitates the selection of semiconductor switches with higher thermal handling capability.

- Molar concentration of the electrolyte does not directly have an impact on the converter design during operation. However, as time passes, the impedance seen by the designed DAB converter will change due to the corrosion of the electrodes and inner walls of the electrolyzer by the electrolyte.

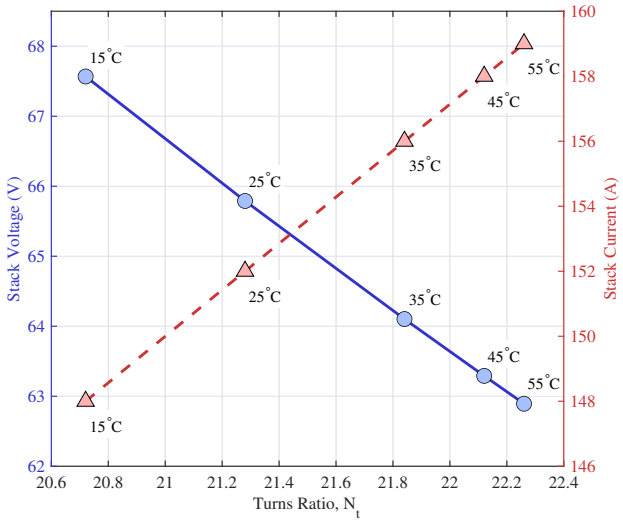

Figure 2.5: Impact of stack temperature on stack voltage, current, and turns ratio of the HF transformer for a 1400 V/70 V, 50 kHz DAB converter supplying a 10 kW electrolyzer at a nominal operating power of 10 kW.

2.5. CONCLUSIONS

This chapter introduced the basics of electrolysis and highlighted its relevance to power electronics design. Knowledge of electrical load is necessary prior to initiating the design of the power electronics. An established modeling approach of an AEL was utilized, and the electrical characteristics of the electrolyzer were extracted. A sensitivity analysis was conducted to see how different parameters affect the electrical behavior of the electrolyzer. These insights were further utilized to draw preliminary insights on the DAB converter design.

3

High-Accuracy Generalized Average Model of Dual Active Bridge Converters

This chapter presents a detailed procedure for deriving the GAM of a DAB converter. The proposed model incorporates higher orders of harmonic components to increase accuracy. Moreover, the turn ratio of the HF transformer (N_t) is considered for realistic modeling, which removes the conventional assumption of a unity turn ratio. A detailed model of the DAB will ensure an accurate control design. Required mathematical expressions are derived and explained thoroughly, with an example showcasing a GAM model of the DAB converter up to the ninth harmonics. Several GAM models using different harmonic orders (first, third, fifth, seventh, and ninth harmonics) are derived and compared with the PLECS simulation model and the real-time simulation model of the DAB converter on the PLECS RT-Box-2. Results show that including up to the ninth harmonics in the proposed model of the DAB converter leads to achieving accurate voltage and current amplitudes that are almost identical to the simulation outputs and even better than the experimental results.

Chapter published in R. S. Deshmukh, P. Bauer and H. Vahedi, "High-Accuracy Generalized Average Model of Dual Active Bridge Converters," in *IEEE Open Journal of Power Electronics*, vol. 5, pp. 452-460, 2024.

3.1. INTRODUCTION

Most DC-DC converters have only one conversion state, containing only DC variables. The small ripple approximation holds in modeling such converters, wherein the higher-order terms are neglected. However, in the case of special DC-DC converters such as the DAB converter, there is an intermediate AC stage, i.e., the converter quantities within this intermediate stage between the two H-Bridge is purely AC, and therefore, the previously stated small ripple approximation no longer can be applied to such a converter.

This chapter emphasizes DAB converters' Generalized Average Modelling approach, offering the following contributions:

- An exhaustive, step-by-step methodology to derive the generalized average model of a DAB converter, extending beyond the conventional scope, is proposed.
- While the GAM methodology frequently presupposes a unity transformer turns ratio for simplification purposes, this assumption does not universally apply to all DAB converter designs. The proposed modeling approach considers the impact of the turn ratio.
- The conventional GAM is typically restricted to the fundamental frequency component. Contrasting this, the proposed modeling procedure, along with the inclusion of the turns ratio, also encompasses the integration of higher-order harmonic elements employing only Fourier transformations to enhance the model's fidelity and applicability.
- Generalized expressions for more straightforward computation when contributions of additional harmonics are necessary are provided to fine-tune the accuracy of the model as per requirement.

3.2. CONCEPT OF GENERALIZED AVERAGE MODELING

To model power electronics converters with more than one conversion stage, the generalized average modeling (GAM) technique can be utilized. This technique captures the contribution of higher-order harmonics using averaging [70]. The GAM is based on the waveform representation using the complex Fourier series [147]. A signal $x(t)$ can be expressed as

$$x(t) = \sum_{-\infty}^{\infty} x_p \cdot e^{jp\omega_s t} \tag{3.1}$$

where ω_s is the angular switching frequency, rad s^{-1}. x_p is the p^{th} coefficient of variable x which can be defined as,

$$x_p(t) = \frac{1}{T_s} \int_{t-T_s}^{T_s} x(\tau) \cdot e^{-jp\omega_s \tau} d\tau \tag{3.2}$$

Applying the principle of averaging,

$$x(t) = \langle x \rangle_p(t) \tag{3.3}$$

GAM technique utilizes two fundamental properties necessary for simplifying the calculations [147]. The first property relates to the derivative of the p^{th} coefficient of variable x.

$$\frac{d\langle x \rangle_p(t)}{dt} = \left\langle \frac{dx}{dt} \right\rangle_p (t) - jp\omega_s \langle x \rangle_p(t) \tag{3.4}$$

The second property relates to the p^{th} product of two variables x and y,

$$\langle x \cdot y \rangle_p(t) = \sum_i \langle x \rangle_{p-i}(t) \cdot \langle y \rangle_i(t) \tag{3.5}$$

3.3. PROPOSED MODELING PROCEDURE

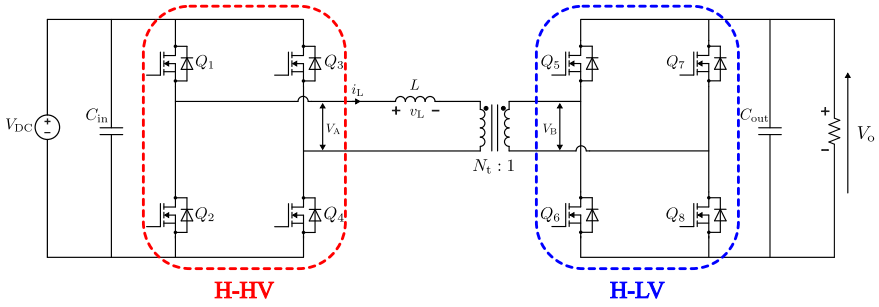

Figure 3.1: DAB Converter

3.3.1. STEP 1: DEFINING THE SWITCHING FUNCTIONS

The operation of a DAB converter is mainly governed by two piece-wise switching functions defined as follows:

$$S_1(t) = \begin{cases} +1 & ,0 \le t < \dfrac{T_s}{2}, \\ -1 & ,\dfrac{T_s}{2} \le t < T_s \end{cases} \tag{3.6}$$

$$S_2(t) = \begin{cases} -1 & ,0 \le t < \dfrac{dT_s}{2}, \\ +1 & ,\dfrac{dT_s}{2} \le t < \dfrac{dT_s}{2} + \dfrac{T_s}{2} \\ -1 & ,\dfrac{dT_s}{2} + \dfrac{T_s}{2} \le t < T_s \end{cases} \tag{3.7}$$

Table 3.1: Switching states of the DAB converter based on the switching functions $S_1(t)$ and $S_2(t)$ with reference to Fig. 3.1.

Value	Switching States ($S_1(t)$)	Switching States ($S_2(t)$)
+1	Q_1, Q_4 ON	Q_5, Q_8 ON
-1	Q_2, Q_3 ON	Q_6, Q_7 ON

Table 3.1 showcases the switching states of the DAB converter based on the defined piece-wise switching functions, where $S_1(t)$ represents the switching function associated with H-HV, and $S_2(t)$ represents the switching function associated with H-LV. For this work, d represents the phase shift duty ratio of H-LV with respect to H-HV.

3.3.2. STEP 2: IDENTIFYING THE FOURIER COEFFICIENTS

Any signal $x(t)$ can be defined using a series of sinusoids with the help of the Fourier Series [148],

$$x(t) = A_0 + \sum_{n=1}^{N} A_n \cos(n\omega_s t) + \sum_{n=1}^{N} B_n \sin(n\omega_s t) \tag{3.8}$$

where

$$A_0 = \frac{1}{T_s} \int_0^{T_s} x(t)dt$$

$$A_n = \frac{2}{T_s} \int_0^{T_s} x(t)\cos(n\omega_s t)dt$$

$$B_n = \frac{2}{T_s} \int_0^{T_s} x(t)\sin(n\omega_s t)dt$$

Before analyzing the switching functions, it is evident from preliminary inspection of their definitions that the DC component for both switching functions, $S_1(t)$ and $S_2(t)$ is zero.

ANALYSIS OF $S_1(t)$

$$A_n = \frac{2}{T_s}\left(\int_0^{\frac{T_s}{2}} \cos(n\omega_s t)dt + \int_{\frac{T_s}{2}}^{T_s} -\cos(n\omega_s t)dt\right)$$

$$B_n = \frac{2}{T_s}\left(\int_0^{\frac{T_s}{2}} \sin(n\omega_s t)dt + \int_{\frac{T_s}{2}}^{T_s} -\sin(n\omega_s t)dt\right)$$

$$A_0 = 0 \tag{3.9}$$

$$A_n = 0, \ \forall \ n \tag{3.10}$$

$$B_n = \begin{cases} \dfrac{4}{n\pi} & , n \text{ is odd} \\ 0 & , n \text{ is even} \end{cases} \tag{3.11}$$

3

ANALYSIS OF $S_2(t)$

$$A'_n = \frac{2}{T_s}\left(\int_0^{\frac{dT_s}{2}} -\cos(n\omega_s t)dt + \int_{\frac{dT_s}{2}}^{\frac{dT_s}{2}+\frac{T_s}{2}} \cos(n\omega_s t)dt + \int_{\frac{dT_s}{2}+\frac{T_s}{2}}^{T_s} -\cos(n\omega_s t)dt\right)$$

$$B'_n = \frac{2}{T_s}\left(\int_0^{\frac{dT_s}{2}} -\sin(n\omega_s t)dt + \int_{\frac{dT_s}{2}}^{\frac{dT_s}{2}+\frac{T_s}{2}} \sin(n\omega_s t)dt + \int_{\frac{dT_s}{2}+\frac{T_s}{2}}^{T_s} -\sin(n\omega_s t)dt\right)$$

$$A'_0 = 0 \tag{3.12}$$

$$A'_n = \begin{cases} \dfrac{-4\sin(n\phi)}{n\pi} & , n \text{ is odd} \\ 0 & , n \text{ is even} \end{cases} \tag{3.13}$$

$$B'_n = \begin{cases} \dfrac{4\cos(n\phi)}{n\pi} & , n \text{ is odd} \\ 0 & , n \text{ is even} \end{cases} \tag{3.14}$$

where ϕ is the phase shift angle of switching function $S_2(t)$ with respect to $S_1(t)$. The switching functions can, therefore, be represented using (3.8),

$$S_1(t) = A_0 + \sum_{n=1}^{N} A_n \cos(n\omega_s t) + \sum_{n=1}^{N} B_n \sin(n\omega_s t) \tag{3.15}$$

$$S_2(t) = A'_0 + \sum_{n=1}^{N} A'_n \cos(n\omega_s t) + \sum_{n=1}^{N} B'_n \sin(n\omega_s t) \tag{3.16}$$

3.3.3. STEP 3: VALIDATION OF FOURIER COEFFICIENTS

Fig. 3.2 shows the comparison between the piece-wise switching functions, $S_1(t)$ (Q_1&Q_4) and $S_2(t)$ (Q_2&Q_3), obtained using (3.6) and (3.7) with Fourier switching functions obtained using (3.15) and (3.16) for $N = 50$. The Fourier coefficients have been computed correctly.

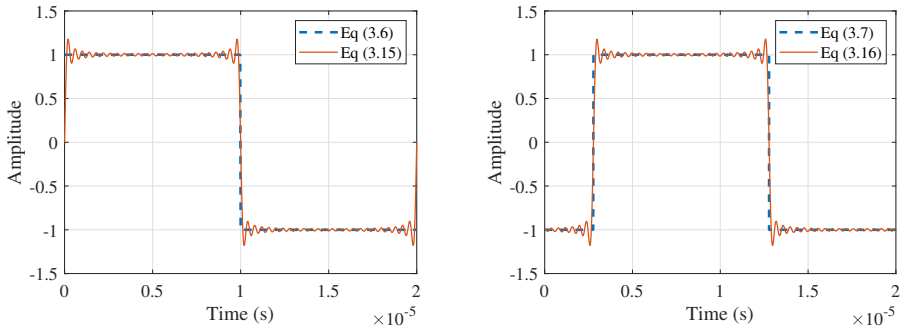

Figure 3.2: Verification of Fourier coefficients, d =0.2764 (ϕ =0.873 rad).

3.3.4. STEP 4: DEFINING THE DAB CONVERTER DYNAMICS

Once the switching functions have been defined and represented correctly, the next step is to define the converter dynamics with the help of state-space equations. The following assumptions have been made:

1. The switching is considered to be instantaneous, and therefore, the effect of dead time has not been considered.
2. The transformer is considered ideal; therefore, the magnetizing inductance is sufficiently large to prevent saturation.
3. All quantities have been referred to the primary side of the transformer.
4. The input voltage and load dynamics are much slower than the converter's.

The primary side inductor current, $i_{\mathrm{L}}(t)$ and the output capacitor voltage, $v_{\mathrm{c}}(t)$ have been considered as state variables for this model. The primary side inductor current, considering the turn ratio of the transformer, N_{t}, can be expressed as,

$$\frac{di_{\mathrm{L}}(t)}{dt} = \frac{1}{L}\Big(V_{\mathrm{A}}(t) - N_{\mathrm{t}}V_{\mathrm{B}}(t) - R_{\mathrm{d}} \cdot i_{\mathrm{L}}(t)\Big)$$

where R_{d} is the lumped resistance that takes into account the equivalent series resistance of the inductor, L, and the on-state resistance of the semiconductor switches.

Similarly, the output capacitor voltage can be expressed as,

$$\frac{dv_{\mathrm{c}}(t)}{dt} = \frac{1}{C_{\mathrm{o}}}\left(i_{\mathrm{rect}}(t) - \frac{v_{\mathrm{c}}(t)}{N_{\mathrm{t}}R_{\mathrm{load}}}\right)$$

where $V_A(t)$ and $V_B(t)$ are the output voltage and input voltage of H-HV and H-LV, respectively, and $i_{rect}(t)$ is the rectified secondary current of the H-LV.

The voltage of the H-bridges, H-HV, and H-LV, as well as the rectified current of H-LV, can now be expressed in terms of the switching functions by using (3.6) and (3.7).

$$\frac{di_L(t)}{dt} = \frac{1}{L}\Big(S_1(t)\cdot V_{DC} - N_t\cdot S_2(t)\cdot v_c(t) - R_d\cdot i_L(t)\Big) \tag{3.17}$$

Similarly, the output capacitor voltage can be expressed as,

$$\frac{dv_c(t)}{dt} = \frac{1}{C_o}\left(S_2(t)\cdot i_s(t) - \frac{v_c(t)}{N_t R_{load}}\right) \tag{3.18}$$

where $i_s(t)$ is the secondary side input current to H-LV.

3.3.5. STEP 5: TRANSITIONING TOWARDS GENERALIZED STATE SPACE AVERAGING

To apply the complex Fourier series, the following changes need to be carried out:

1. The Fourier coefficients computed for the switching functions in Step 2 need to be expressed in terms of equivalent complex Fourier coefficients [148]. Note that the DC component remains independent of this change.

$$\langle S_1\rangle_0 = A_0 \tag{3.19}$$

$$\langle S_1\rangle_{n\mathrm{R}} = \frac{A_n}{2} \tag{3.20}$$

$$\langle S_1\rangle_{n\mathrm{I}} = -\frac{B_n}{2} \tag{3.21}$$

$$\langle S_2\rangle_0 = A'_0 \tag{3.22}$$

$$\langle S_2\rangle_{n\mathrm{R}} = \frac{A'_n}{2} \tag{3.23}$$

$$\langle S_2\rangle_{n\mathrm{I}} = -\frac{B'_n}{2} \tag{3.24}$$

   where the subscripts R and I denote the real and imaginary components.

2. Equations (3.17) and (3.18) need to be decomposed into real and imaginary components.

Therefore, applying (3.3) and (3.4) on (3.17) and (3.18),

$$\frac{d\langle i_{\mathrm{L}}\rangle_0}{dt} = \frac{1}{L}\Big(\langle S_1 \cdot V_{\mathrm{DC}}\rangle_0 - N_{\mathrm{t}} \cdot \langle S_2 \cdot v_{\mathrm{c}}\rangle_0 - R_{\mathrm{d}} \cdot \langle i_{\mathrm{L}}\rangle_0\Big) \tag{3.25}$$

$$\frac{d\langle i_{\mathrm{L}}\rangle_{1\mathrm{R}}}{dt} = \frac{1}{L}\Big(\langle S_1 \cdot V_{\mathrm{DC}}\rangle_{1\mathrm{R}} - N_{\mathrm{t}} \cdot \langle S_2 \cdot v_{\mathrm{c}}\rangle_{1\mathrm{R}} - R_{\mathrm{d}} \cdot \langle i_{\mathrm{L}}\rangle_{1\mathrm{R}}\Big) + \omega_{\mathrm{s}}\langle i_{\mathrm{L}}\rangle_{1\mathrm{I}} \tag{3.26}$$

$$\frac{d\langle i_{\mathrm{L}}\rangle_{1\mathrm{I}}}{dt} = \frac{1}{L}\Big(\langle S_1 \cdot V_{\mathrm{DC}}\rangle_{1\mathrm{I}} - N_{\mathrm{t}} \cdot \langle S_2 \cdot v_{\mathrm{c}}\rangle_{1\mathrm{I}} - R_{\mathrm{d}} \cdot \langle i_{\mathrm{L}}\rangle_{1\mathrm{I}}\Big) - \omega_{\mathrm{s}}\langle i_{\mathrm{L}}\rangle_{1\mathrm{R}} \tag{3.27}$$

$$\frac{d\langle v_{\mathrm{c}}\rangle_0}{dt} = \frac{1}{C_{\mathrm{o}}}\left(\langle S_2 \cdot i_{\mathrm{s}}\rangle_0 - \frac{\langle v_{\mathrm{c}}\rangle_0}{N_{\mathrm{t}}R_{\mathrm{load}}}\right) \tag{3.28}$$

$$\frac{d\langle v_{\mathrm{c}}\rangle_{1\mathrm{R}}}{dt} = \frac{1}{C_{\mathrm{o}}}\left(\langle S_2 \cdot i_{\mathrm{s}}\rangle_{1\mathrm{R}} - \frac{\langle v_{\mathrm{c}}\rangle_{1\mathrm{R}}}{N_{\mathrm{t}}R_{\mathrm{load}}}\right) + \omega_{\mathrm{s}} \cdot \langle v_{\mathrm{c}}\rangle_{1\mathrm{I}} \tag{3.29}$$

$$\frac{d\langle v_{\mathrm{c}}\rangle_{1\mathrm{I}}}{dt} = \frac{1}{C_{\mathrm{o}}}\left(\langle S_2 \cdot i_{\mathrm{s}}\rangle_{1\mathrm{I}} - \frac{\langle v_{\mathrm{c}}\rangle_{1\mathrm{I}}}{N_{\mathrm{t}}R_{\mathrm{load}}}\right) - \omega_{\mathrm{s}} \cdot \langle v_{\mathrm{c}}\rangle_{1\mathrm{R}} \tag{3.30}$$

Equations (3.25), (3.29), and (3.30) can be truncated based on the fourth assumption. (3.26)-(3.28) contains the product of the fundamental harmonics as well as the product of the DC component. Therefore, (3.5) is necessary to further simplify (3.26)-(3.28).

Considering that the $-N^{\mathrm{th}}$ coefficient is a complex conjugate of the N^{th} coefficient, we have for $N = 1$,

$$\langle xy\rangle_0 = \langle x\rangle_1 \cdot \langle y\rangle_{-1} + \langle x\rangle_0 \cdot \langle y\rangle_0 + \langle x\rangle_{-1} \cdot \langle y\rangle_1 \tag{3.31}$$

$$\langle xy\rangle_1 = \langle x\rangle_1 \cdot \langle y\rangle_0 + \langle x\rangle_0 \cdot \langle y\rangle_1 \tag{3.32}$$

In general, for the first M odd harmonics,

$$\boxed{\langle xy\rangle_0 = \langle x\rangle_0 \cdot \langle y\rangle_0 + 2 \cdot \Big(\sum_{p=1}^{M}\big(\langle x\rangle_{(2p-1)\mathrm{R}} \cdot \langle y\rangle_{(2p-1)\mathrm{R}} + \langle x\rangle_{(2p-1)\mathrm{I}} \cdot \langle y\rangle_{(2p-1)\mathrm{I}}\big)\Big)} \tag{3.33}$$

Similarly,

$$\langle xy\rangle_{(2p-1)\mathrm{R}} = \langle x\rangle_{(2p-1)\mathrm{R}} \cdot \langle y\rangle_0 + \langle x\rangle_0 \cdot \langle y\rangle_{(2p-1)\mathrm{R}} \tag{3.34}$$

$$\langle xy\rangle_{(2p-1)\mathrm{I}} = \langle x\rangle_{(2p-1)\mathrm{I}} \cdot \langle y\rangle_0 + \langle x\rangle_0 \cdot \langle y\rangle_{(2p-1)\mathrm{I}} \tag{3.35}$$

where $p = 1, 2, 3 \ldots M$.

Applying (3.33)-(3.35) to (3.26)-(3.28), we have,

$$\frac{d\langle i_{\mathrm{L}}\rangle_{1\mathrm{R}}}{dt} = \frac{1}{L}\Big(\big(\langle S_1\rangle_{1\mathrm{R}}\cdot\langle V_{\mathrm{DC}}\rangle_0 + \langle S_1\rangle_0\cdot\langle V_{\mathrm{DC}}\rangle_{1\mathrm{R}}\big) - N_{\mathrm{t}}\cdot\big(\langle S_2\rangle_{1\mathrm{R}}\cdot\langle v_{\mathrm{c}}\rangle_0 + \langle S_2\rangle_0\cdot\langle v_{\mathrm{c}}\rangle_{1\mathrm{R}}\big) - R_{\mathrm{d}}\cdot\langle i_{\mathrm{L}}\rangle_{1\mathrm{R}}\Big) + \omega_{\mathrm{s}}\langle i_{\mathrm{L}}\rangle_{1\mathrm{I}}$$

$$\frac{d\langle i_{\mathrm{L}}\rangle_{1\mathrm{I}}}{dt} = \frac{1}{L}\Big(\big(\langle S_1\rangle_{1\mathrm{I}}\cdot\langle V_{\mathrm{DC}}\rangle_0 + \langle S_1\rangle_0\cdot\langle V_{\mathrm{DC}}\rangle_{1\mathrm{I}}\big) - N_{\mathrm{t}}\cdot\big(\langle S_2\rangle_{1\mathrm{I}}\cdot\langle v_{\mathrm{c}}\rangle_0 + \langle S_2\rangle_0\cdot\langle v_{\mathrm{c}}\rangle_{1\mathrm{I}}\big) - R_{\mathrm{d}}\cdot\langle i_{\mathrm{L}}\rangle_{1\mathrm{I}}\Big) - \omega_{\mathrm{s}}\langle i_{\mathrm{L}}\rangle_{1\mathrm{R}}$$

$$\frac{d\langle v_{\mathrm{c}}\rangle_0}{dt} = \frac{1}{C_{\mathrm{o}}}\Big(\langle S_2\rangle_0\cdot\langle i_{\mathrm{L}}\rangle_0 + 2\cdot\big(\langle S_2\rangle_{1\mathrm{R}}\cdot\langle i_{\mathrm{L}}\rangle_{1\mathrm{R}} + \langle S_2\rangle_{1\mathrm{I}}\cdot\langle i_{\mathrm{L}}\rangle_{1\mathrm{I}}\big) - \frac{\langle v_{\mathrm{c}}\rangle_0}{N_{\mathrm{t}}R_{\mathrm{load}}}\Big)$$

Applying the fourth assumption and substituting the values of $\langle S_1\rangle_0$, $\langle S_1\rangle_{n\mathrm{R}}$, $\langle S_1\rangle_{n\mathrm{I}}$, $\langle S_2\rangle_0$, $\langle S_2\rangle_{n\mathrm{R}}$, and $\langle S_2\rangle_{n\mathrm{I}}$ from (3.19)-(3.24), we have,

$$\frac{d\langle i_{\mathrm{L}}\rangle_{1\mathrm{R}}}{dt} = \frac{1}{L}\Big(\frac{2N_{\mathrm{t}}\sin(\phi)\langle v_{\mathrm{c}}\rangle_0}{\pi} - R_{\mathrm{d}}\cdot\langle i_{\mathrm{L}}\rangle_{1\mathrm{R}}\Big) + \omega_{\mathrm{s}}\langle i_{\mathrm{L}}\rangle_{1\mathrm{I}} \tag{3.36}$$

$$\frac{d\langle i_{\mathrm{L}}\rangle_{1\mathrm{I}}}{dt} = \frac{1}{L}\Big(\frac{-2V_{\mathrm{DC}}}{\pi} + \frac{2N_{\mathrm{t}}\cos(\phi)\langle v_{\mathrm{c}}\rangle_0}{\pi} - R_{\mathrm{d}}\cdot\langle i_{\mathrm{L}}\rangle_{1\mathrm{I}}\Big) - \omega_{\mathrm{s}}\langle i_{\mathrm{L}}\rangle_{1\mathrm{R}} \tag{3.37}$$

$$\frac{d\langle v_{\mathrm{c}}\rangle_0}{dt} = \frac{1}{C_{\mathrm{o}}}\left(\frac{-4\sin(\phi)\langle i_{\mathrm{L}}\rangle_{1\mathrm{R}}}{\pi} - \frac{4\cos(\phi)\langle i_{\mathrm{L}}\rangle_{1\mathrm{I}}}{\pi} - \frac{\langle v_{\mathrm{c}}\rangle_0}{N_{\mathrm{t}}R_{\mathrm{load}}}\right) \tag{3.38}$$

3.3.6. STEP 6: MATRIX REPRESENTATION OF THE SYSTEM

Equations (3.36), (3.37), and (3.38) define the dynamics of the DAB converter by only considering the fundamental component. (3.39) provides the matrix representation defining the dynamics of the DAB converter, considering only the fundamental component.

$$\frac{d}{dt}\begin{bmatrix} i_{\mathrm{L1R}} \\ i_{\mathrm{L1I}} \\ v_{\mathrm{c0}} \end{bmatrix} = \begin{bmatrix} -\frac{R_{\mathrm{d}}}{L} & \omega_{\mathrm{s}} & \frac{2N_{\mathrm{t}}\sin(\phi)}{\pi L} \\ -\omega_{\mathrm{s}} & -\frac{R_{\mathrm{d}}}{L} & \frac{2N_{\mathrm{t}}\cos(\phi)}{\pi L} \\ \frac{-4\sin(\phi)}{\pi C_{\mathrm{o}}} & \frac{-4\cos(\phi)}{\pi C_{\mathrm{o}}} & \frac{-1}{N_{\mathrm{t}}R_{\mathrm{load}}C_{\mathrm{o}}} \end{bmatrix}\begin{bmatrix} i_{\mathrm{L1R}} \\ i_{\mathrm{L1I}} \\ v_{\mathrm{c0}} \end{bmatrix} + \begin{bmatrix} 0 \\ \frac{-2}{L\pi} \\ 0 \end{bmatrix} V_{\mathrm{DC}} \tag{3.39}$$

The system defined by (3.39) can be easily recomputed to include additional harmonic components using (3.3)-(3.5), and (3.33)-(3.35) to model the transformer current of the DAB converter accurately. Considering the contribution until the third harmonics,

the DAB converter model is described below as an example.

$$\frac{d\langle i_{\mathrm{L}}\rangle_{1\mathrm{R}}}{dt} = \frac{1}{L}\left(\frac{2N_{\mathrm{t}}\sin(\phi)\langle v_{\mathrm{c}}\rangle_0}{\pi} - R_{\mathrm{d}}\cdot\langle i_{\mathrm{L}}\rangle_{1\mathrm{R}}\right) + \omega_{\mathrm{s}}\langle i_{\mathrm{L}}\rangle_{1\mathrm{I}}$$

$$\frac{d\langle i_{\mathrm{L}}\rangle_{1\mathrm{I}}}{dt} = \frac{1}{L}\left(\frac{-2V_{\mathrm{DC}}}{\pi} + \frac{2N_{\mathrm{t}}\cos(\phi)\langle v_{\mathrm{c}}\rangle_0}{\pi} - R_{\mathrm{d}}\cdot\langle i_{\mathrm{L}}\rangle_{1\mathrm{I}}\right) - \omega_{\mathrm{s}}\langle i_{\mathrm{L}}\rangle_{1\mathrm{R}}$$

$$\frac{d\langle i_{\mathrm{L}}\rangle_{3\mathrm{R}}}{dt} = \frac{1}{L}\left(\frac{2N_{\mathrm{t}}\sin(3\phi)\langle v_{\mathrm{c}}\rangle_0}{3\pi} - R_{\mathrm{d}}\cdot\langle i_{\mathrm{L}}\rangle_{3\mathrm{R}}\right) + 3\omega_{\mathrm{s}}\langle i_{\mathrm{L}}\rangle_{3\mathrm{I}}$$

$$\frac{d\langle i_{\mathrm{L}}\rangle_{3\mathrm{I}}}{dt} = \frac{1}{L}\left(\frac{-2V_{\mathrm{DC}}}{3\pi} + \frac{2N_{\mathrm{t}}\cos(3\phi)\langle v_{\mathrm{c}}\rangle_0}{3\pi} - R_{\mathrm{d}}\cdot\langle i_{\mathrm{L}}\rangle_{3\mathrm{I}}\right) - 3\omega_{\mathrm{s}}\langle i_{\mathrm{L}}\rangle_{3\mathrm{R}}$$

$$\frac{d\langle v_{\mathrm{c}}\rangle_0}{dt} = \frac{1}{C_{\mathrm{o}}}\left(\frac{-4\sin(\phi)\langle i_{\mathrm{L}}\rangle_{1\mathrm{R}}}{\pi} - \frac{4\cos(\phi)\langle i_{\mathrm{L}}\rangle_{1\mathrm{I}}}{\pi} - \frac{4\sin(3\phi)\langle i_{\mathrm{L}}\rangle_{3\mathrm{R}}}{3\pi} - \frac{4\cos(3\phi)\langle i_{\mathrm{L}}\rangle_{3\mathrm{I}}}{3\pi} - \frac{\langle v_{\mathrm{c}}\rangle_0}{N_{\mathrm{t}}R_{\mathrm{load}}}\right)$$

Equation (3.40) showcases the GAM model of the DAB converter considering the first five odd harmonics.

3

$$
\frac{d}{dt}\begin{bmatrix} i_{\mathrm{L1R}} \\ i_{\mathrm{L1I}} \\ i_{\mathrm{L3R}} \\ i_{\mathrm{L3I}} \\ i_{\mathrm{L5R}} \\ i_{\mathrm{L5I}} \\ i_{\mathrm{L7R}} \\ i_{\mathrm{L7I}} \\ i_{\mathrm{L9R}} \\ i_{\mathrm{L9I}} \\ v_{\mathrm{c0}} \end{bmatrix} = \begin{bmatrix} -\frac{R_{\mathrm{d}}}{L} & \omega_{\mathrm{s}} & 0 & 0 & 0 & 0 & 0 & 0 & 0 & 0 & \frac{-N_{\mathrm{t}}\langle S_2\rangle_{1\mathrm{R}}}{L} \\ -\omega_{\mathrm{s}} & -\frac{R_{\mathrm{d}}}{L} & 0 & 0 & 0 & 0 & 0 & 0 & 0 & 0 & \frac{-N_{\mathrm{t}}\langle S_2\rangle_{1\mathrm{I}}}{L} \\ 0 & 0 & -\frac{R_{\mathrm{d}}}{L} & 3\omega_{\mathrm{s}} & 0 & 0 & 0 & 0 & 0 & 0 & \frac{-N_{\mathrm{t}}\langle S_2\rangle_{3\mathrm{R}}}{L} \\ 0 & 0 & -3\omega_{\mathrm{s}} & -\frac{R_{\mathrm{d}}}{L} & 0 & 0 & 0 & 0 & 0 & 0 & \frac{-N_{\mathrm{t}}\langle S_2\rangle_{3\mathrm{I}}}{L} \\ 0 & 0 & 0 & 0 & -\frac{R_{\mathrm{d}}}{L} & 5\omega_{\mathrm{s}} & 0 & 0 & 0 & 0 & \frac{-N_{\mathrm{t}}\langle S_2\rangle_{5\mathrm{R}}}{L} \\ 0 & 0 & 0 & 0 & -5\omega_{\mathrm{s}} & -\frac{R_{\mathrm{d}}}{L} & 0 & 0 & 0 & 0 & \frac{-N_{\mathrm{t}}\langle S_2\rangle_{5\mathrm{I}}}{L} \\ 0 & 0 & 0 & 0 & 0 & 0 & -\frac{R_{\mathrm{d}}}{L} & 7\omega_{\mathrm{s}} & 0 & 0 & \frac{-N_{\mathrm{t}}\langle S_2\rangle_{7\mathrm{R}}}{L} \\ 0 & 0 & 0 & 0 & 0 & 0 & -7\omega_{\mathrm{s}} & -\frac{R_{\mathrm{d}}}{L} & 0 & 0 & \frac{-N_{\mathrm{t}}\langle S_2\rangle_{7\mathrm{I}}}{L} \\ 0 & 0 & 0 & 0 & 0 & 0 & 0 & 0 & -\frac{R_{\mathrm{d}}}{L} & 9\omega_{\mathrm{s}} & \frac{-N_{\mathrm{t}}\langle S_2\rangle_{9\mathrm{R}}}{L} \\ 0 & 0 & 0 & 0 & 0 & 0 & 0 & 0 & -9\omega_{\mathrm{s}} & -\frac{R_{\mathrm{d}}}{L} & \frac{-N_{\mathrm{t}}\langle S_2\rangle_{9\mathrm{I}}}{L} \\ \frac{2\langle S_2\rangle_{1\mathrm{R}}}{C_{\mathrm{o}}} & \frac{2\langle S_2\rangle_{1\mathrm{I}}}{C_{\mathrm{o}}} & \frac{2\langle S_2\rangle_{3\mathrm{R}}}{C_{\mathrm{o}}} & \frac{2\langle S_2\rangle_{3\mathrm{I}}}{C_{\mathrm{o}}} & \frac{2\langle S_2\rangle_{5\mathrm{R}}}{C_{\mathrm{o}}} & \frac{2\langle S_2\rangle_{5\mathrm{I}}}{C_{\mathrm{o}}} & \frac{2\langle S_2\rangle_{7\mathrm{R}}}{C_{\mathrm{o}}} & \frac{2\langle S_2\rangle_{7\mathrm{I}}}{C_{\mathrm{o}}} & \frac{2\langle S_2\rangle_{9\mathrm{R}}}{C_{\mathrm{o}}} & \frac{2\langle S_2\rangle_{9\mathrm{I}}}{C_{\mathrm{o}}} & \frac{-1}{N_{\mathrm{t}}R_{\mathrm{load}}C_{\mathrm{o}}} \end{bmatrix} \begin{bmatrix} i_{\mathrm{L1R}} \\ i_{\mathrm{L1I}} \\ i_{\mathrm{L3R}} \\ i_{\mathrm{L3I}} \\ i_{\mathrm{L5R}} \\ i_{\mathrm{L5I}} \\ i_{\mathrm{L7R}} \\ i_{\mathrm{L7I}} \\ i_{\mathrm{L9R}} \\ i_{\mathrm{L9I}} \\ v_{\mathrm{c0}} \end{bmatrix}
$$

$$
+ \begin{bmatrix} 0 & \frac{\langle S_1\rangle_{1\mathrm{I}}}{L} & 0 & \frac{\langle S_1\rangle_{3\mathrm{I}}}{L} & 0 & \frac{\langle S_1\rangle_{5\mathrm{I}}}{L} & 0 & \frac{\langle S_1\rangle_{7\mathrm{I}}}{L} & 0 & \frac{\langle S_1\rangle_{9\mathrm{I}}}{L} & 0 \end{bmatrix}^{\mathrm{T}} V_{\mathrm{DC}} \tag{3.40}
$$

3.4. RESULTS AND DISCUSSION

A test case was considered to validate the GAM model. Table 3.3 showcases the specifications of the DAB converter utilized for the validation purpose. Fig. 3.3 showcases the experimental setup consisting of a PLECS RT-Box-2 connected to a PC.

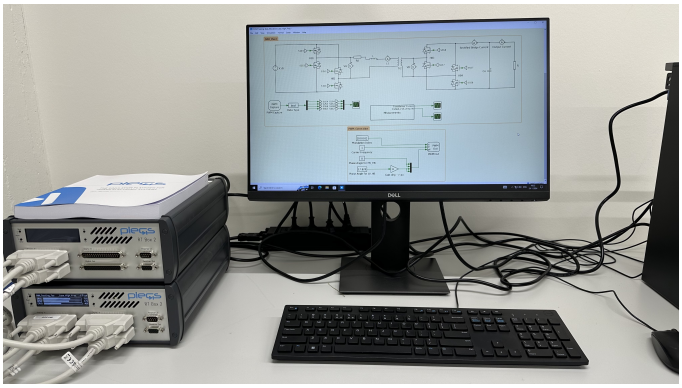

Figure 3.3: Experimental Setup.

Table 3.2 provides the specifications of the PLECS RT-Box-2. A discretization time step of $T_{\text{disc}} = 1.5\ \mu$s was selected for the real-time simulation model.

Table 3.2: PLECS RT-Box-2 Specifications [149]

Processor	Xilinx Zynq Ultrascale+	ZU9EG
Number of CPU cores	4	ARM Cortex-A53, 1.5 GHz
Analog inputs	Channels	16
	Resolution	16 bit
	Input type	Differential
	Max. sample rate	5 Msps
Analog outputs	Channels	16
	Resolution	16 bit
	Max. update rate	5 Msps
Digital inputs	Channels	32
	Logic levels	3.3 V (5 V tolerant)
Digital outputs	Channels	32
	Logic levels	3.3 V, 5 V

Table 3.3: Test Converter Specifications

Parameter	Value	Parameter	Value
P_o	2.5 kW	f_{sw}	50 kHz
V_{DC}	500 V	R_d	0.1 Ω
V_o	50 V	C_o	200 μF
N_t	10:1	R_{load}	1Ω
L	200 μH		

Fig. 3.4(a) showcases the steady state output voltage response obtained from GAM ($M = 1$ and $M = 5$), PLECS simulation model, and the RT-Box-2 for the considered test case. While the PLECS model response for the output voltage contains higher ripple content, the GAM response for the output voltage contains little or no ripple. It is evident from the response that the output voltage of the converter for the case of GAM ($M = 1$) has a steady-state error. On the other hand, the output voltage of GAM ($M = 5$) converges towards the PLECS simulation response, such that it is nearly the average of the PLECS simulation response. The real-time simulation response contains a steady-state error but has a similar ripple content to the PLECS simulation model. The transformer current with contributions up to the first M odd harmonics using the GAM can be extracted using the following expression:

$$i_L(t) = 2\sum_{p=1}^{M}\left(i_{L(2p-1)R}\cos\left((2p-1)\cdot\left(\omega_s t-\frac{\phi}{2}\right)\right)+i_{L(2p-1)I}\sin\left((2p-1)\cdot\left(\omega_s t-\frac{\phi}{2}\right)\right)\right) \tag{3.41}$$

With the increase in M, the accuracy of the GAM increases as shown in Fig. 3.4(b)-3.4(f) that showcases the comparison of the reconstructed transformer currents of the GAM with the response of the PLECS simulation model and the real-time simulation model.

To quantitatively evaluate the accuracy of the GAM obtained using the proposed procedure, several GAMs (fundamental, third, fifth, seventh, and ninth harmonics) are compared against the PLECS and the real-time simulation models. Table 3.4 showcases the GAM accuracy. All models are operated at five different operating power set-points, starting from 0.5 kW up to the rated power of 2.5 kW. Absolute error is calculated by comparing the output power of a given model type with the analytically calculated power, P_o.

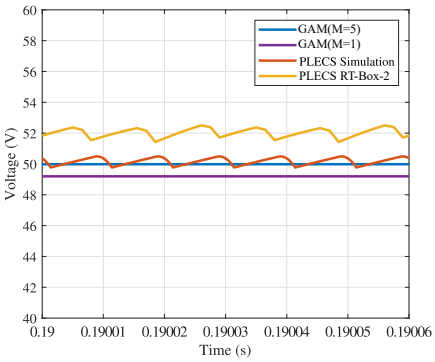

(a) Output Voltage Response

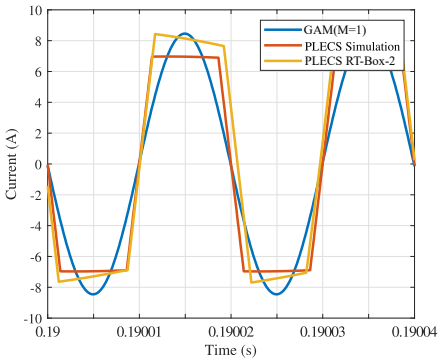

(b) Transformer currents ($M = 1$)

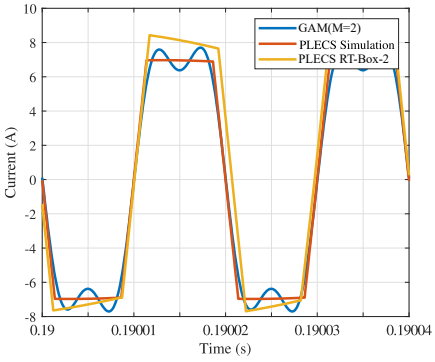

(c) Transformer currents ($M = 2$)

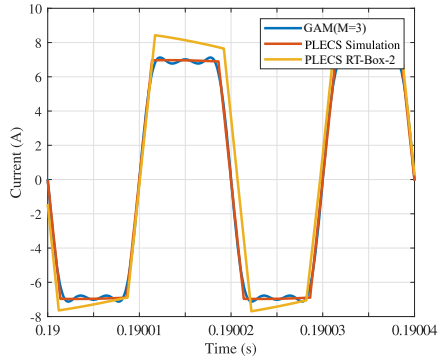

(d) Transformer currents ($M = 3$)

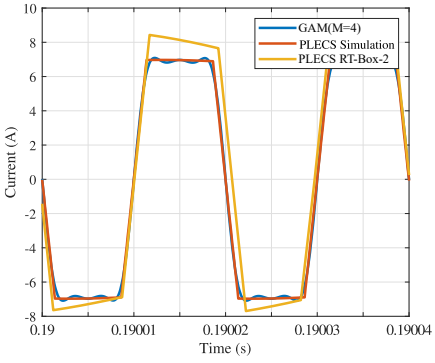

(e) Transformer currents ($M = 4$)

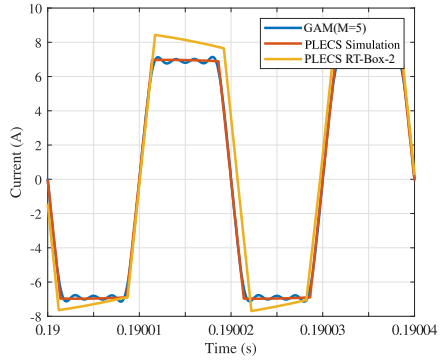

(f) Transformer currents ($M = 5$)

Figure 3.4: Comparison of output voltage response and steady-state transformer currents of GAM, PLECS simulation model, and PLECS RT-Box-2 for the first M odd harmonics.

Table 3.4: Evaluation of GAM Accuracy

d	0.0993	0.1486	0.1916	0.2333	0.2764
P_o	0.5 kW	1 kW	1.5 kW	2 kW	2.5 kW
Model Type	**% Error**				
PLECS	0.868	0.748	0.631	0.652	0.681
PLECS RT-Box	104.69	9.399	12.909	12.914	8.288
GAM (M = 1)	21.16	15.536	11.021	6.932	3.184
GAM (M = 2)	5.177	1.331	0.625	1.57	1.662
GAM (M = 3)	0.64	1.019	0.975	0.412	0.265
GAM (M = 4)	0.733	0.869	0.121	0.355	0.418
GAM (M = 5)	0.992	0.380	0.226	0.234	0.065

Results indicate that the GAM (M = 1) is the most inaccurate model among the considered GAMs, with an error of greater than 3% up to a maximum error of 21.16%. As M increases for the subsequent GAMs, this error significantly reduces. The GAM (M = 5) presents an error of less than 1% and has relatively higher accuracy than other GAMs, PLECS simulation, and real-time simulation models on the RT-Box-2. It is interesting to note two observations:

- First, the contribution up to the ninth harmonic (M = 5) is sufficient to model the transformer currents of the converter accurately.
- The transformer currents obtained from the real-time simulation present a similar wave shape; however, they contain inaccuracies in their amplitudes. An error of 104.69% was observed for PLECS RT-Box-2 at P_o = 0.5 kW. This error reduces significantly as the operating power gradually increases.

The following two factors can justify the amplitude inaccuracies throughout the operating power range and the large error at P_o = 0.5 kW:

- The RT-Box-2 contains four available CPU cores; however, only three are available for computation during the real-time simulation. The remaining core is reserved for the Linux operating system, which runs internally. The discretization time step depends not only on the complexity of the real-time simulation model of the power electronics converter but also on the switching frequency. The best time step that could be achieved for RT-Box-2, considering the converter model and choice of switching frequency, was T_{disc} = 1.5 μs. Any discretization step below 1.5 μs leads to an overrun condition of the real-time simulator. The computation load distribution among the CPU cores is inconsistent in this condition. This inconsistency causes overburden on the CPU cores and causes the converter quantities visualized on the scope to contain frequent fluctuations and inaccuracies.
- To achieve an operating power of 0.5 kW, the phase angle required is approximately ϕ = 0.312 rad. This phase angle is expressed as 1.98 μs when translated

into the switching period. For the chosen discretization time-step, the CPU cannot accurately reconstruct the transformer current since the CPU updates the converter quantities every 1.5 μs. Assuming that t = 0 initially, information is lost between t = 1.5 μs and t = 3 μs as the CPU updates every 1.5 μs. However, this issue no longer exists as the phase angle gradually increases. Considering the operating power of P_o = 1.5 kW, the corresponding phase angle is approximately ϕ = 0.602 rad. This phase angle is expressed as 3.83 μs when translated into the switching period. In this case, the CPU can reconstruct the transformer currents more accurately than in the previous case, as the data points of the transformer current are retained within two samples of 1.5 μs each. This is evident by the decrease in error for PLECS RT-Box-2 as the operating power increases beyond 0.5 kW.

3.5. CONCLUSIONS

In this chapter, a step-by-step procedure to obtain a DAB model with the help of the GAM technique using only Fourier transformations was proposed. Unlike the conventional GAM technique, which is often restricted to consideration of only the fundamental component, the proposed procedure provides general expressions that can be used for developing the GAM of the converter that can take into account higher-order harmonics. Moreover, the impact of the transformer's turn ratio was considered within the modeling procedure. The fundamental GAM (M = 1) of the DAB converter was developed to describe the modeling procedure and extended further to develop a ninth harmonic GAM (M = 5) of the converter. The validation of the model obtained with the proposed method was carried out by comparing transformer currents obtained from several GAMs (fundamental, third, fifth, seventh, and ninth harmonics) against the transformer currents of the simulation model and real-time simulation model in PLECS and PLECS RT-Box-2, respectively. The steady-state output voltage was evaluated by comparing the PLECS simulation and real-time simulation response with GAM (M = 1 and M = 5). A quantitative evaluation of model accuracy indicated that the ninth harmonic GAM of the converter was more consistent in accuracy over the operating power range than the PLECS simulation and the real-time simulation model on the PLECS RT-Box-2. The findings from this chapter emphasize the importance of accurately modeling and controlling HF transformer currents to ensure efficient power transfer. This is quite important for electrolysis due to the extremely high current operation and non-linear nature.

4

Peak Current Optimization of DAB Modulation Strategies for Electrolysis

Electrolyzers operate as nonlinear, low-voltage, high-current loads, presenting significant challenges for power conversion systems. This chapter investigates state-of-the-art modulation schemes for the DAB converters, focusing on their performance and interaction with electrolyzer loads in electrolysis applications. The behavior of electrolyzers is compared with that of conventional CV loads across various modulation schemes, using peak primary transformer current as the evaluation metric at three power levels: 1 kW, 10 kW, and 100 kW. A peak current optimization strategy tailored for electrolysis applications is proposed. Based on this, an optimized operating trajectory for the DAB converter during electrolysis is identified for each power level. The optimization results are validated experimentally using a 1 kW, 20 kHz prototype, and through MATLAB simulations for the 10 kW and 100 kW systems.

Chapter based on R. S. Deshmukh, G. Rituraj, P. Bauer ,and H. Vahedi, "Evaluation and Optimization of Modulation Strategies of a Dual Active Bridge Converter for Electrolyzers," IEEE Open Journal of the Industrial Electronics Society. *(accepted)*

4.1. INTRODUCTION

The DAB topology alone cannot meet all performance requirements. With reference to the insights reported in Section 1.2.3, despite the widespread deployment of DAB converters in EV charging and DC grid applications, there is limited converter-level analysis conducted in these domains, with no converter-level analysis carried out for electrolyzer applications. This chapter emphasizes application-oriented converter-level analysis of the DAB converter for electrolyzer applications, offering the following contributions:

- It examines DAB converter performance within electrolysis using the three primary phase shift modulation schemes—SPS, DPS, and TPS, providing expressions for output power and state currents for various operating modes of DPS and TPS tailored for electrolysis, with detailed illustrations of each mode.
- While the SPS phase shift ratio is straightforward to determine, calculating phase shift ratios for DPS and TPS schemes is more complex. A simple peak current optimization method using the `fmincon` function in MATLAB is presented for DPS and TPS methods for electrolysis. Detailed steps of this optimization process are provided along with parameter selections.
- A comparative analysis is performed to show the effect of electrolyzer load on the SPS, DPS, and TPS modulation schemes from the primary transformer peak currents context for three power ratings (1 kW, 10 kW, and 100 kW) of electrolyzer against a 500 V CV load of the same power ratings.
- An optimized operation for electrolysis is proposed for the modulation methods and for each power rating. This optimized operation is compared against the conventional SPS modulation scheme, highlighting its benefit.

4.2. Single Phase Shift Modulation (SPS)

The SPS modulation scheme is one of the fundamental modulation schemes proposed for the DAB converter. It has been considered a standard controller in the industry and, therefore, is the most widely used scheme [150–153]. Fig. 4.2 showcases the SPS modulation scheme. Each switch of the DAB converter is operated at a fixed duty ratio of 50 %. However, the switches in the L-LV bridge are phase-shifted by an angle ϕ or phase-shift duty ratio d with switches in the H-HV bridge as the reference. This way, power flow can be achieved from H-HV to L-LV or vice versa.

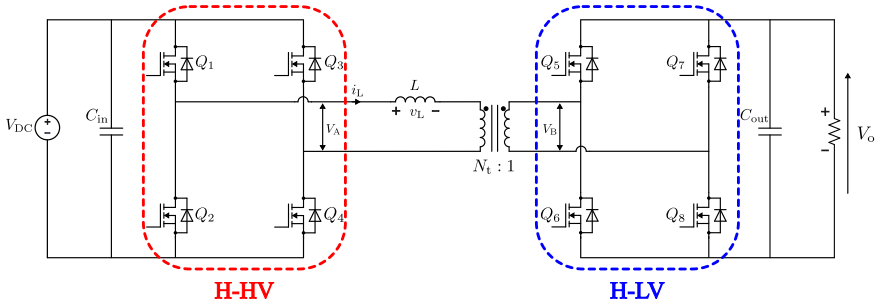

Figure 4.1: DAB Converter

The equations governing the operation of the DAB in the SPS modulation scheme are given below,

$$P_o = \frac{(d \cdot (1-d)) \cdot V_{DC} \cdot k V_o \cdot N_t}{2 \cdot f_{sw} \cdot L} \tag{4.1}$$

$$N_t = \frac{V_{DC}}{V_o} \tag{4.2}$$

$$d = \frac{\phi}{\pi} \tag{4.3}$$

where, k is the votage gain which is defined as the ratio of the stack voltage during electrolysis to the nominal output voltage of the DAB converter. Furthermore, by substituting Equation (2.5) in Equation (4.1), we have,

$$P_o = \frac{V_{DC} N_t N_s R d(1-d)}{2 L f_{sw} z F} \left(T_c \log\left(\frac{(P_{abs} - P_{v,KOH})^{1.5}}{a_{we}} \right) + \frac{zF}{R} \left(V_{rev}^0 + s \log\left(\frac{i_{act(A)}}{t} + 1 \right) + v \log\left(\frac{i_{act(K)}}{w} + 1 \right) + V_{int} \right) \right) \tag{4.4}$$

Equation (4.4) showcases the relationship between the parameters of the DAB converter and the electrolyzer parameters. It provides a strong indication that the choice of converter parameters can no longer be dependent purely on the voltage, current, and switching frequency, but also on parameters of the electrolyzer, such as the vapor pressure, water activity, activation currents, the internal resistance (the electrode-electrolyte interface behaves as a resistance), stack temperature, etc.

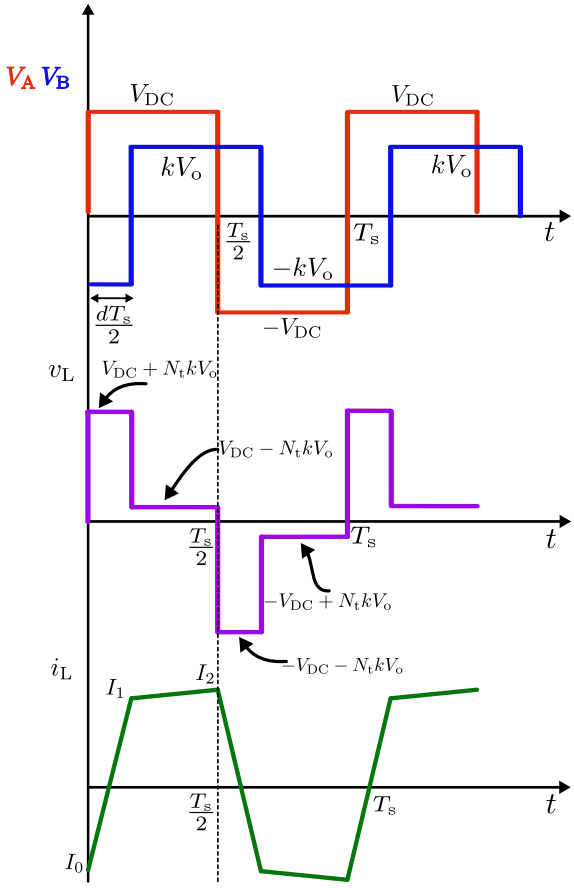

Figure 4.2: SPS Modulation

The small inertia and ease of realizing soft-switching are some of the merits of SPS [154], making it an attractive modulation scheme at rated power operation, considering the low voltage and high current nature of electrolysis.

4.3. Dual Phase Shift Modulation (DPS)

In the SPS modulation scheme, the power flow is determined by the phase shift ratio, d. Due to the presence of only a single degree of freedom, the efficiency of this scheme begins to deteriorate when the voltage gain of the transformer deviates from unity [155]. This scenario occurs during electrolysis, too, since the voltage and current of the electrolyzer no longer remain fixed but remain dynamic as the reaction within the electrolyzer continues. This deviation of voltage gain from unity results in circulating currents or an increase in the reactive power within the converter, causing it to draw more current. Given the nature of electrolysis, i.e., a low-voltage and high-current process, the losses within the converter can increase significantly in such a scenario [156]. The DPS modulation scheme can address the issue of circulating currents, expand the soft-switching range, and decrease current stress [157–159].

Unlike the SPS modulation scheme, wherein only a single degree of freedom, d exists, the DPS modulation scheme consists of two phase shift ratios, d_1 and d_2. d_1 is the inner phase shift ratio while, d_2 is the outer phase shift ratio. Both phase shift ratios are lagging. Switch Q_4 is phase shifted by d_1 while, switch Q_5 is phase shifted by d_2. Furthermore, switch Q_8 is phase shifted by d_1+d_2. This sum of the inner and the outer phase shift ratios can also be defined as d_3 for the sake of simplicity. In this manner, phase shift ratio, d_3 is dependent on the inner and outer phase ratios. The presence of two degrees of freedom allows for better control of power flow. Fig. 4.3(a)-4.3(d) showcases the considered modes of operation.

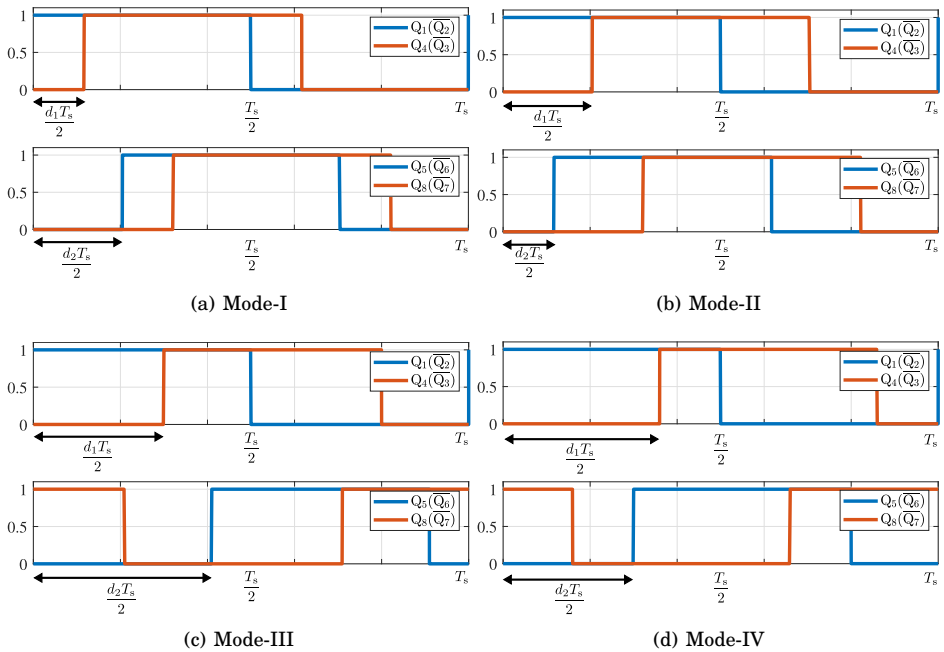

(a) Mode-I (b) Mode-II

(c) Mode-III (d) Mode-IV

Figure 4.3: Switching patterns for considered four modes considered in DPS modulation

4.4. DPS MODES FOR ELECTROLYSIS

4.4.1. MODE - I ($d_1 + d_2 \leq 1$, $d_1 \leq d_2$)

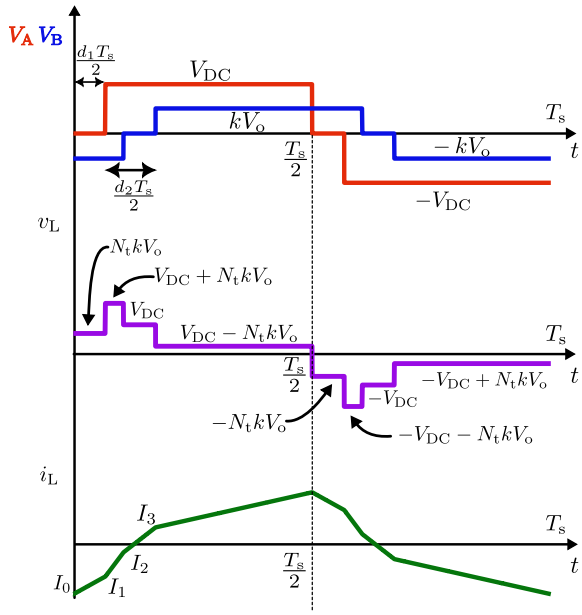

Figure 4.4: DPS Mode - I

Fig. 4.4 illustrates Mode I of the DPS modulation scheme. Considering half-cycle symmetry, we have,

$$\frac{2Lf_{sw}(I_1 - I_0)}{d_1} = N_t k V_o \tag{4.5}$$

$$\frac{2Lf_{sw}(I_2 - I_1)}{d_2 - d_1} = V_{DC} - N_t k V_o \tag{4.6}$$

$$\frac{2Lf_{sw}(I_3 - I_2)}{d_1} = V_{DC} \tag{4.7}$$

$$\frac{-2Lf_{sw}(I_0 + I_3)}{1 - d_1 - d_2} = V_{DC} - N_t k V_o \tag{4.8}$$

Solving Equations (4.5-4.8) we have,

$$\boxed{I_0 = A(-k(d_1+2d_2-1)+d_1-1)} \tag{4.9}$$

$$\boxed{I_1 = A(k(1+d_1-2d_2)+d_1-1)} \tag{4.10}$$

$$\boxed{I_2 = A(-k(d_1-1)-d_1+2d_2-1)} \tag{4.11}$$

$$\boxed{I_3 = A(k(1-d_1)+d_1+2d_2-1)} \tag{4.12}$$

Fig. 4.5 showcases the transformer current along with the rectified stack current (blue) at the output of H-LV bridge.

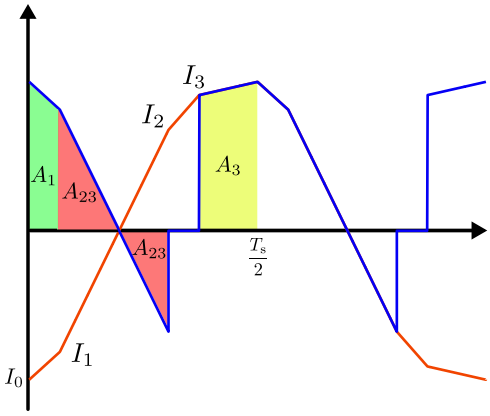

Figure 4.5: Rectified output stack current(blue) during DPS Mode-I.

The average stack current can be determined by calculating the charge enclosed within the shaded regions by using the state currents described in Equations (4.9-4.12).

$$A_1 = \frac{-d_1}{4f_{sw}}(I_0+I_1)$$

$$A_{23} = \frac{1}{4f_{sw}}(I_1+I_2)(d_1-d_2)$$

$$A_4 = \frac{1}{4f_{sw}}(-I_0+I_3)(1-d_1-d_2)$$

$$\boxed{A_1 = \frac{d_1 V_{DC}}{8 L f_{sw}^2}(k(2d_2 - 1) - d_1 + 1)} \tag{4.13}$$

$$\boxed{A_{23} = \frac{V_{DC}}{8 L f_{sw}^2}(k-1)(1-d_2)(d_1 - d_2)} \tag{4.14}$$

$$\boxed{A_4 = \frac{d_2 V_{DC}}{8 L f_{sw}^2}(k+1)(1-d_1-d_2)} \tag{4.15}$$

The average current is given by,

$$I_o = 2 N_t f_{sw} A_{enc} \tag{4.16}$$

$$\boxed{I_o = \frac{N_t V_{DC}}{4 L f_{sw}}(2d_2(1-d_2) - d_1^2)} \tag{4.17}$$

The output power of the DAB converter operating in DPS Mode - I during electrolysis is given by,

$$P_o = k V_o I_o = v_{stack} I_o \tag{4.18}$$

$$\boxed{P_o = \frac{N_t v_{stack} V_{DC}}{4 L f_{sw}}(-d_1^2 - 2d_2^2 + 2d_2)} \tag{4.19}$$

4.4.2. Mode - II ($d_1 + d_2 \leq 1$, $d_1 > d_2$)

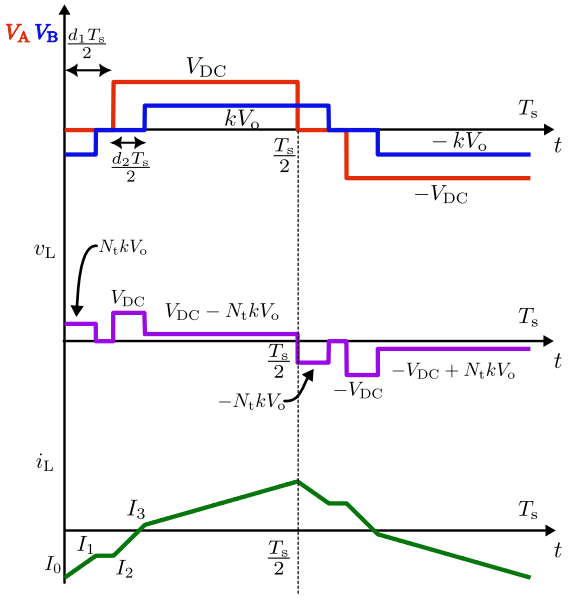

Figure 4.6: DPS Mode - II

Fig. 4.6 illustrates Mode-II of the DPS modulation scheme. Considering half-cycle symmetry, we have,

$$\frac{2Lf_{sw}(I_1 - I_0)}{d_2} = N_t k V_o \tag{4.20}$$

$$\frac{2Lf_{sw}(I_3 - I_2)}{d_2} = V_{DC} \tag{4.21}$$

$$\frac{-2Lf_{sw}(I_0 + I_3)}{1 - d_1 - d_2} = V_{DC} - N_t k V_o \tag{4.22}$$

$$I_1 = I_2 \tag{4.23}$$

Solving Equations (4.20-4.23) we have,

$$\boxed{I_0 = A(-k(d_1+2d_2-1)+d_1-1)} \tag{4.24}$$

$$\boxed{I_1 = -A(k-1)(d_1-1)} \tag{4.25}$$

$$\boxed{I_2 = -A(k-1)(d_1-1)} \tag{4.26}$$

$$\boxed{I_3 = A(k(1-d_1)+d_1+2d_2-1)} \tag{4.27}$$

Fig. 4.7 showcases the transformer current along with the rectified stack current at the output of the H-LV bridge.

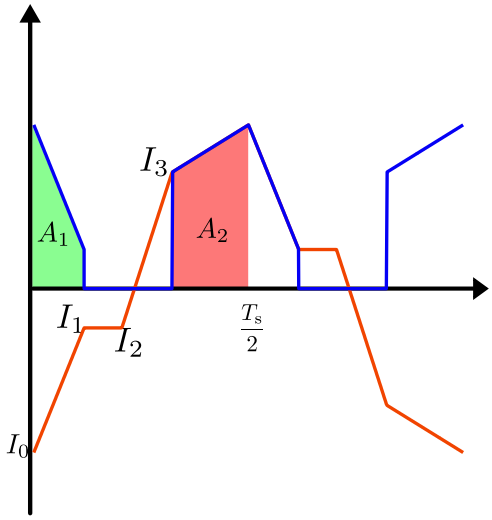

Figure 4.7: Rectified output stack current(blue) during DPS Mode-II.

The average stack current can be determined by calculating the charge enclosed within the shaded regions by using the state currents described in Equations (4.24-4.27).

$$A_1 = \frac{-d_2}{4f_{sw}}(I_0+I_1)$$

$$A_2 = \frac{1}{4f_{sw}}(-I_0+I_3)(1-d_1-d_2)$$

$$\boxed{A_1 = \frac{d_2 V_{DC}}{8 L f_{sw}^2}(k(d_1+d_2-1)-d_1+1)} \tag{4.28}$$

$$\boxed{A_2 = \frac{d_2 V_{DC}}{8 L f_{sw}^2}(k+1)(1-d_1-d_2)} \tag{4.29}$$

Using Equation (4.16), the average output current is given by,

$$\boxed{I_o = \frac{N_t V_{DC} d_2}{4 L f_{sw}}(2-2d_1-d_2)} \tag{4.30}$$

Using Equation (4.18), the output power of the DAB converter operating in DPS Mode - II during electrolysis is given by,

$$\boxed{P_o = \frac{N_t v_{stack} V_{DC}}{4 L f_{sw}} d_2(2-2d_1-d_2)} \tag{4.31}$$

4.4.3. Mode - III ($d_1+d_2>1$, $d_1 \le d_2$)

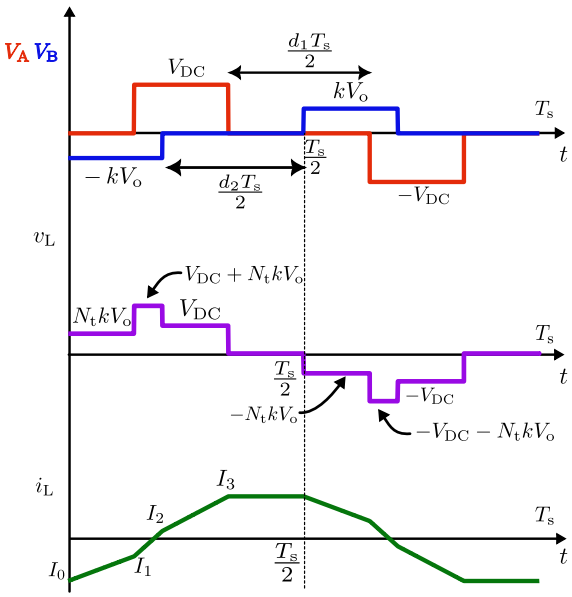

Figure 4.8: DPS Mode - III

Fig. 4.8 illustrates Mode III of the DPS modulation scheme. Considering half-cycle symmetry, we have,

$$\frac{2Lf_{sw}(I_2 - I_1)}{1 - d_2} = N_t k V_o \tag{4.32}$$

$$\frac{2Lf_{sw}(I_3 - I_2)}{d_2 - d_1} = V_{DC} + N_t k V_o \tag{4.33}$$

$$\frac{-2Lf_{sw}(I_0 + I_3)}{1 - d_2} = V_{DC} \tag{4.34}$$

$$I_0 = I_1 \tag{4.35}$$

Solving Equation (4.32-4.35) we have,

$$\boxed{I_0 = A(k+1)(d_1 - 1)} \tag{4.36}$$

$$\boxed{I_1 = A(k+1)(d_1 - 1)} \tag{4.37}$$

$$\boxed{I_2 = A(k(1 + d_1 - 2d_2) + d_1 - 1)} \tag{4.38}$$

$$\boxed{I_3 = A(-k(d_1 - 1) - d_1 + 2d_2 - 1)} \tag{4.39}$$

Fig. 4.9 showcases the transformer current along with the rectified stack current at the output of the H-LV bridge.

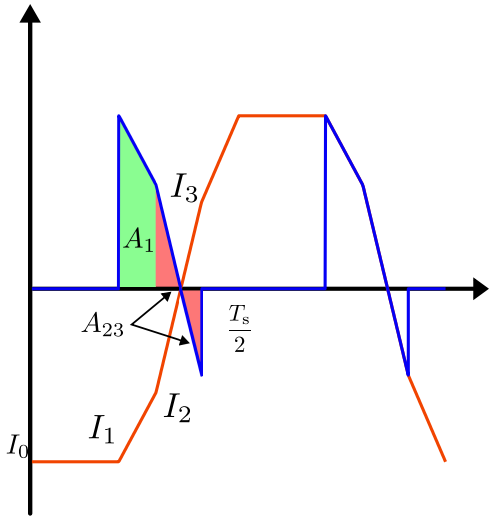

Figure 4.9: Rectified output stack current(blue) during DPS Mode-III.

The average stack current can be determined by calculating the charge enclosed within the shaded regions by using the state currents described in Equations (4.36-4.39).

$$A_1 = \frac{1}{4f_{sw}}(I_1 + I_2)(1 - d_2)$$

$$A_{23} = \frac{1}{4f_{sw}}(I_2 + I_3)(d_1 - d_2)$$

$$\boxed{A_1 = \frac{V_{DC}}{8Lf_{sw}^2}(d_2 - 1)(k(d_1 - d_2) + d_1 - 1)} \tag{4.40}$$

$$\boxed{A_{23} = \frac{V_{DC}}{8Lf_{sw}^2}(k - 1)(d_1 - d_2)(1 - d_2)} \tag{4.41}$$

Using Equation (4.16), the average output current is given by,

$$\boxed{I_o = \frac{N_t V_{DC}}{4Lf_{sw}}(1 - d_2)(1 - 2d_1 + d_2)} \tag{4.42}$$

Using Equation (4.18), the output power of the DAB converter operating in DPS Mode - III during electrolysis is given by,

$$\boxed{P_o = \frac{N_t v_{stack} V_{DC}}{4Lf_{sw}}(1 - d_2)(d_2 - 2d_1 + 1)} \tag{4.43}$$

4.4.4. MODE - IV ($d_1 + d_2 > 1, d_1 > d_2$)

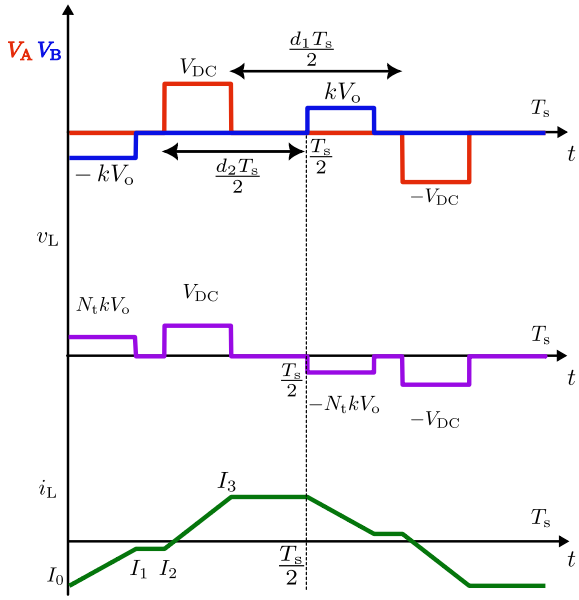

Figure 4.10: DPS Mode - IV

Fig. 4.10 illustrates Mode IV of the DPS modulation scheme. Considering half-cycle symmetry, we have,

$$\frac{2Lf_{sw}(I_3 - I_0)}{1 - d_1} = N_t k V_o \tag{4.44}$$

$$\frac{-2Lf_{sw}(I_0 + I_3)}{1 - d_1} = V_{DC} \tag{4.45}$$

$$I_0 = I_1 \tag{4.46}$$

$$I_2 = I_3 \tag{4.47}$$

Solving Equation (4.44-4.47) we have,

$$\boxed{I_0 = A(k+1)(d_1 - 1)} \tag{4.48}$$

$$\boxed{I_1 = A(k+1)(d_1 - 1)} \tag{4.49}$$

$$\boxed{I_2 = A(k-1)(1 - d_1)} \tag{4.50}$$

$$\boxed{I_3 = A(k-1)(1 - d_1)} \tag{4.51}$$

Fig. 4.11 showcases the transformer current along with the rectified stack current at the output of the H-LV bridge.

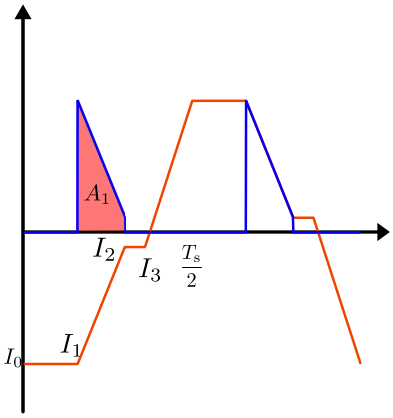

Figure 4.11: Rectified output stack current(blue) during DPS Mode-IV.

The average stack current can be determined by calculating the charge enclosed within the shaded regions by using the state currents described in Equations (4.48-4.51).

$$A_1 = \frac{-1}{4f_{sw}}(I_0 + I_2)(1 - d_1)$$

$$\boxed{A_1 = \frac{V_{DC}}{8Lf_{sw}^2}(d_1 - 1)^2} \tag{4.52}$$

Using Equation (4.16), the average output current is given by,

$$\boxed{I_o = \frac{N_t V_{DC}}{4Lf_{sw}}(d_1 - 1)^2} \tag{4.53}$$

Using Equation (4.18), the output power of the DAB converter operating in DPS Mode - III during electrolysis is given by,

$$\boxed{P_o = \frac{N_t v_{stack} V_{DC}}{4Lf_{sw}}(d_1 - 1)^2} \tag{4.54}$$

For each mode, Table 4.1 provides the constraints for the phase shift ratios, expressions for the state currents of the transformer (primary side), and expressions for the operating power of the converter for electrolysis where, $A = \frac{N_t V_o}{4Lf_{sw}}$.

Table 4.1: Operating modes in DPS modulation.

$d_1+d_2 \leq 1$			
Mode - I ($d_1 \leq d_2$)		Mode - II ($d_1 > d_2$)	
$I_0 =$	$A(-k(d_1+2d_2-1)+d_1-1)$	$I_0 =$	$A(-k(d_1+2d_2-1)+d_1-1)$
$I_1 =$	$A(k(1+d_1-2d_2)+d_1-1)$	$I_1 =$	$-A(d_1-1)(k-1)$
$I_2 =$	$A(-k(d_1-1)-d_1+2d_2-1)$	$I_2 =$	$-A(d_1-1)(k-1)$
$I_3 =$	$A(k(1-d_1)+d_1+2d_2-1)$	$I_3 =$	$A(k(1-d_1)+d_1+2d_2-1)$
$P_o =$	$kAV_{DC}(-d_1^2-2d_2^2+2d_2)$	$P_o =$	$kAV_{DC}d_2(-2d_1-d_2+2)$
$d_1+d_2 > 1$			
Mode - III ($d_1 \leq d_2$)		Mode - IV ($d_1 > d_2$)	
$I_0 =$	$A(d_1-1)(k+1)$	$I_0 =$	$A(d_1-1)(k+1)$
$I_1 =$	$A(d_1-1)(k+1)$	$I_1 =$	$A(d_1-1)(k+1)$
$I_2 =$	$A(k(1+d_1-2d_2)+d_1-1)$	$I_2 =$	$A(1-d_1)(k-1)$
$I_3 =$	$A(-k(d_1-1)-d_1-1+2d_2)$	$I_3 =$	$A(1-d_1)(k-1)$
$P_o =$	$kAV_{DC}(1-d_2)(d_2-2d_1+1)$	$P_o =$	$kAV_{DC}(d_1-1)^2$

4.5. Triple Phase Shift Modulation (TPS)

In the DPS modulation scheme, switch Q_8 was applied with a phase shift ratio, d_3, which was the sum of the inner phase ratio, d_1, and the outer phase shift ratio, d_2. By making d_3 independent of d_1 and d_2, an additional degree of freedom can be introduced for controlling the power flow. This is known as the TPS modulation scheme[59, 160, 161]. It is interesting to note that SPS and DPS are special cases of TPS modulation schemes. They can be implemented within the TPS modulation scheme with the following conditions,

$$d_1 = 0 \;\&\; d_2 = d_3 \rightarrow \text{SPS}$$
$$d_1 \neq 0 \;\&\; d_3 = d_1 + d_2 \rightarrow \text{DPS}$$

Fig. 4.12(a)-4.12(c) showcases the considered three modes of operation.

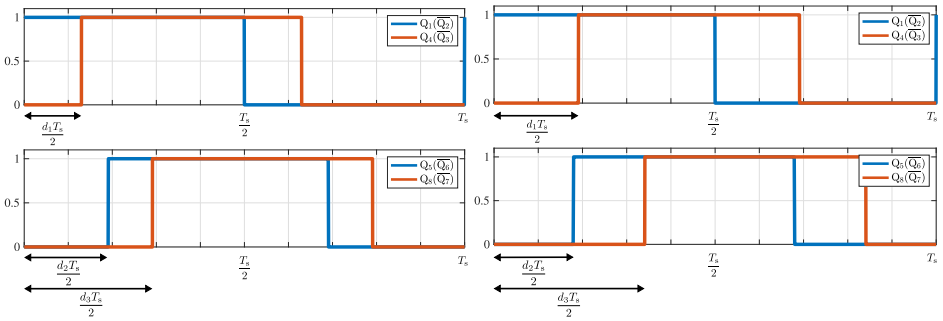

(a) Mode-I (b) Mode-II

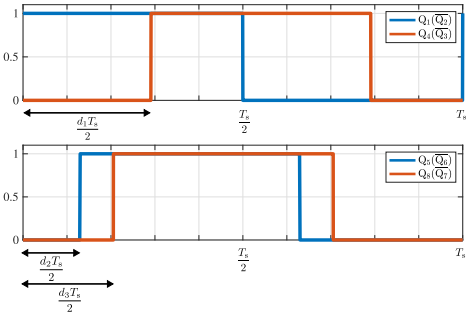

(c) Mode-III

Figure 4.12: Switching patterns for three considered modes in TPS modulation

4.6. TPS MODES FOR ELECTROLYSIS

4.6.1. MODE - I ($d_1 \leq d_2 \leq d_3$)

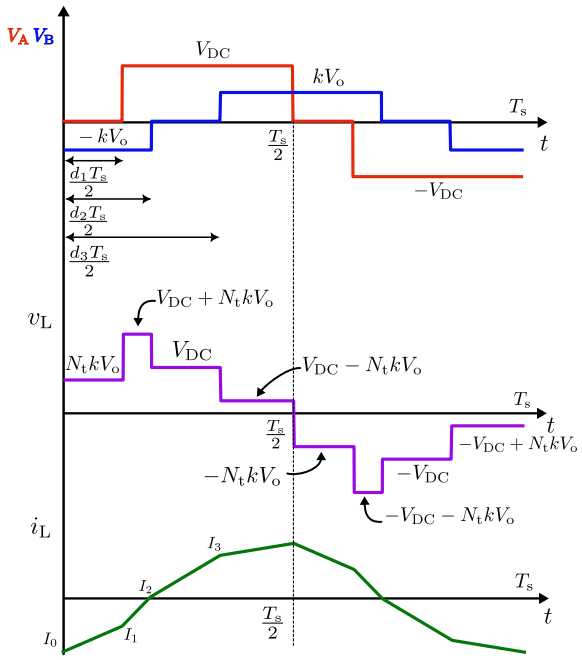

Figure 4.13: TPS Mode-I

Fig. 4.13 illustrates Mode I of the TPS modulation scheme. Considering half-cycle symmetry, we have,

$$\frac{2Lf_{sw}(I_1 - I_0)}{d_1} = N_t k V_o \tag{4.55}$$

$$\frac{2Lf_{sw}(I_2 - I_1)}{d_2 - d_1} = V_{DC} + N_t k V_o \tag{4.56}$$

$$\frac{2Lf_{sw}(I_3 - I_2)}{d_3 - d_2} = V_{DC} \tag{4.57}$$

$$\frac{-2Lf_{sw}(I_0 + I_3)}{1 - d_3} = V_{DC} - N_t k V_o \tag{4.58}$$

Solving Equation (4.55-4.58) we have,

$$\boxed{I_0 = A(-k(d_2+d_3-1)+d_1-1)} \tag{4.59}$$

$$\boxed{I_1 = A(k(2d_1-d_2-d_3+1)+d_1-1)} \tag{4.60}$$

$$\boxed{I_2 = A(k(d_2-d_3+1)-d_1+2d_2-1)} \tag{4.61}$$

$$\boxed{I_3 = A(k(d_2-d_3+1)-d_1+2d_3-1)} \tag{4.62}$$

Fig. 4.14 showcases the transformer current along with the rectified stack current at the output of the H-LV bridge.

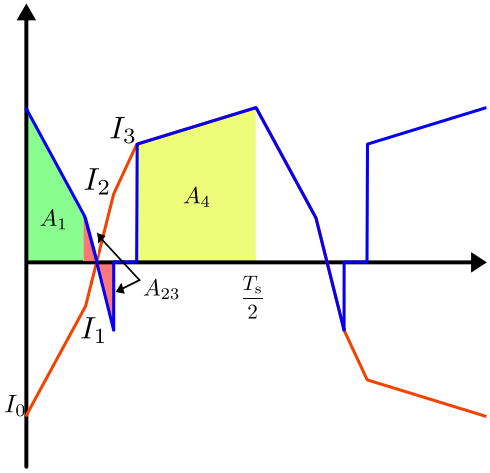

Figure 4.14: Rectified output stack current(blue) during TPS Mode-I.

The average stack current can be determined by calculating the charge enclosed within the shaded areas by using the state currents described in Equations (4.59-4.62).

$$A_1 = \frac{-d_1}{4f_{sw}}(I_0+I_1)$$

$$A_{23} = \frac{1}{4f_{sw}}(I_1+I_2)(d_1-d_2)$$

$$A_4 = \frac{1}{4f_{sw}}(I_3-I_0)(1-d_3)$$

$$A_1 = \frac{V_{DC}}{8Lf_{sw}^2} d_1(-k(1+d_1-d_2-d_3)-d_1+1) \tag{4.63}$$

$$A_{23} = \frac{V_{DC}}{8Lf_{sw}^2} (d_1-d_2)(k(1+d_1-d_3)+d_2-1) \tag{4.64}$$

$$A_4 = \frac{V_{DC}}{8Lf_{sw}^2} (1-d_3)(-d_1+kd_2+d_3) \tag{4.65}$$

Using Equation (4.16), the average output current is given by,

$$I_o = \frac{N_t V_{DC}}{4Lf_{sw}} (-d_1(d_1-d_2-d_3+1)-d_2(d_2-1)-d_3(d_3-1)) \tag{4.66}$$

Using Equation (4.18), the output power of the DAB converter operating in TPS Mode-I during electrolysis is given by,

$$P_o = \frac{N_t v_{stack} V_{DC}}{4Lf_{sw}} (-d_1(d_1-d_2-d_3+1)-d_2(d_2-1)-d_3(d_3-1)) \tag{4.67}$$

4.6.2. MODE - II ($d_2 \le d_1 \le d_3$)

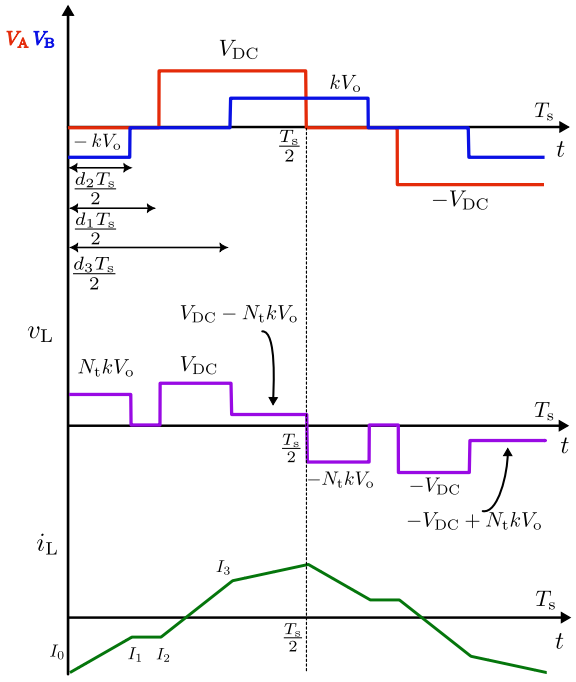

Figure 4.15: TPS Mode-II

Fig. 4.15 illustrates Mode-II of the TPS modulation scheme. Considering half-cycle symmetry, we have,

$$\frac{2Lf_{sw}(I_1 - I_0)}{d_2} = N_t k V_o \tag{4.68}$$

$$\frac{2Lf_{sw}(I_3 - I_1)}{d_3 - d_1} = V_{DC} \tag{4.69}$$

$$\frac{-2Lf_{sw}(I_0 + I_3)}{1 - d_3} = V_{DC} - N_t k V_o \tag{4.70}$$

$$I_2 = I_1 \tag{4.71}$$

Solving Equation (4.68-4.71) we have,

$$\boxed{I_0 = A(-k(d_2 + d_3 - 1) + d_1 - 1)} \tag{4.72}$$

$$\boxed{I_1 = A(k(d_2 - d_3 + 1) + d_1 - 1)} \tag{4.73}$$

$$\boxed{I_2 = A(k(d_2 - d_3 + 1) + d_1 - 1)} \tag{4.74}$$

$$\boxed{I_3 = A(k(d_2 - d_3 + 1) - d_1 + 2d_3 - 1)} \tag{4.75}$$

Fig. 4.16 showcases the transformer current along with the rectified stack current at the output of the H-LV bridge.

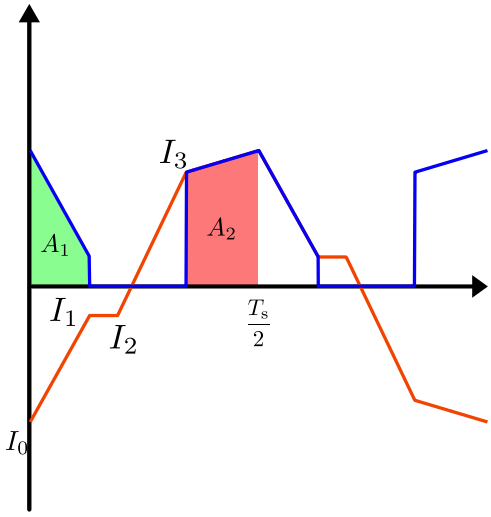

Figure 4.16: Rectified output stack current(blue) during TPS Mode-II.

The average stack current can be determined by calculating the charge enclosed within the shaded areas by using the state currents described in Equations (4.72-4.75).

$$A_1 = \frac{-d_2}{4f_{sw}}(I_0 + I_1)$$

$$A_2 = \frac{1}{4f_{sw}}(I_3 - I_0)(1 - d_3)$$

$$\boxed{A_1 = \frac{V_{DC}}{8Lf_{sw}^2} d_2(k(d_3 - 1) - d_1 + 1)} \tag{4.76}$$

$$\boxed{A_2 = \frac{V_{DC}}{8Lf_{sw}^2}(1 - d_3)(d_3 - d_1 + kd_2)} \tag{4.77}$$

Using Equation (4.16), the average output current is given by,

$$\boxed{I_o = \frac{N_t V_{DC}}{4Lf_{sw}}(d_1(d_3 - d_2 - 1) + d_2 + d_3(1 - d_3))} \tag{4.78}$$

Using Equation (4.18), the output power of the DAB converter operating in TPS Mode-II during electrolysis is given by,

$$\boxed{P_o = \frac{N_t v_{stack} V_{DC}}{4Lf_{sw}}(d_1(d_3 - d_2 - 1) + d_2 + d_3(1 - d_3))} \tag{4.79}$$

4.6.3. Mode - III ($d_2 \leq d_3 \leq d_1$)

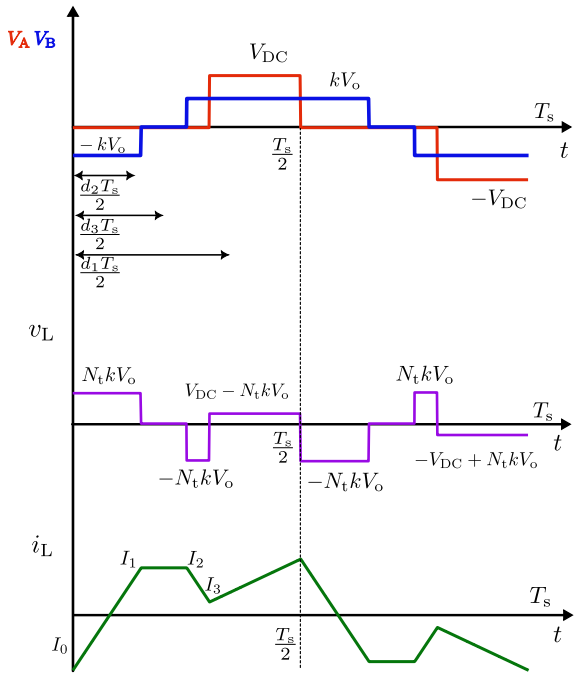

Figure 4.17: TPS Mode-III

Fig. 4.17 illustrates Mode III of the TPS modulation scheme. Considering half-cycle symmetry, we have,

$$\frac{2Lf_{sw}(I_1 - I_0)}{d_2} = N_t k V_o \tag{4.80}$$

$$\frac{2Lf_{sw}(I_3 - I_2)}{d_1 - d_3} = -N_t k V_o \tag{4.81}$$

$$\frac{-2Lf_{sw}(I_0 + I_3)}{1 - d_1} = V_{DC} - N_t k V_o \tag{4.82}$$

$$I_2 = I_1 \tag{4.83}$$

Solving Equation (4.80-4.83) we have,

$$\boxed{I_0 = A(-k(d_2 + d_3 - 1) + d_1 - 1)} \tag{4.84}$$

$$\boxed{I_1 = A(k(d_2 - d_3 + 1) + d_1 - 1)} \tag{4.85}$$

$$\boxed{I_2 = A(k(d_2 - d_3 + 1) + d_1 - 1)} \tag{4.86}$$

$$\boxed{I_3 = A(k(d_2 - 2d_1 + d_3 + 1) + d_1 - 1)} \tag{4.87}$$

Fig. 4.18 showcases the transformer current along with the rectified stack current at the output of the H-LV bridge.

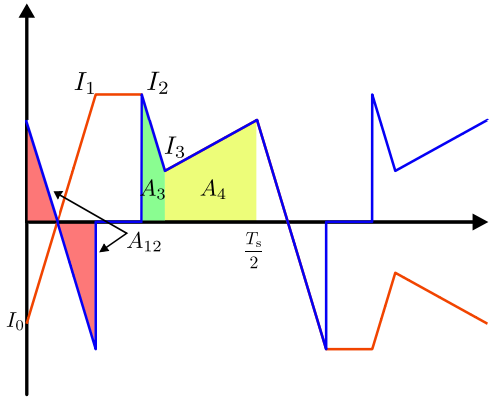

Figure 4.18: Rectified output stack current(blue) during TPS Mode-III.

The average stack current can be determined by calculating the charge enclosed within the shaded areas by using the state currents described in Equations (4.84-4.87).

$$A_{12} = \frac{-d_2}{4f_{sw}}(I_0 + I_1)$$

$$A_3 = \frac{1}{4f_{sw}}(I_2 + I_3)(d_1 - d_3)$$

$$A_4 = \frac{1}{4f_{sw}}(I_3 - I_0)(1 - d_1)$$

$$\boxed{A_{12} = \frac{V_{DC}}{8Lf_{sw}^2} d_2(k(d_3-1)-d_1+1)} \tag{4.88}$$

$$\boxed{A_3 = \frac{V_{DC}}{8Lf_{sw}^2} (d_1-d_3)(k(1-d_1+d_2)+d_1-1)} \tag{4.89}$$

$$\boxed{A_4 = \frac{V_{DC}}{8Lf_{sw}^2} k(1-d_1)(d_2+d_3-d_1)} \tag{4.90}$$

Using Equation (4.16), the average output current is given by,

$$\boxed{I_o = \frac{N_t V_{DC}}{4Lf_{sw}} (1-d_1)(d_2-d_1+d_3)} \tag{4.91}$$

Using Equation (4.18), the output power of the DAB converter operating in TPS Mode - III during electrolysis is given by,

$$\boxed{P_o = \frac{N_t v_{stack} V_{DC}}{4Lf_{sw}} (1-d_1)(d_2-d_1+d_3)} \tag{4.92}$$

For each mode, Table 4.2 provides the constraints for the phase shift ratios, expressions for the state currents of the transformer (primary side), and expressions for the operating power of the converter for electrolysis where, $A = \frac{N_t V_o}{4Lf_{sw}}$.

Table 4.2: Considered operating modes in TPS modulation.

Mode - I ($d_1 \le d_2 \le d_3$)		Mode - II ($d_2 \le d_1 \le d_3$)		Mode - III ($d_2 \le d_3 \le d_1$)	
$I_0 =$	$A(-k(d_2+d_3-1)+d_1-1)$	$I_0 =$	$A(-k(d_2+d_3-1)+d_1-1)$	$I_0 =$	$A(-k(d_2+d_3-1)+d_1-1)$
$I_1 =$	$A(k(2d_1-d_2-d_3+1)+d_1-1)$	$I_1 =$	$A(k(d_2-d_3+1)+d_1-1)$	$I_1 =$	$A(k(d_2-d_3+1)+d_1-1)$
$I_2 =$	$A(k(d_2-d_3+1)-d_1+2d_2-1)$	$I_2 =$	$A(k(d_2-d_3+1)+d_1-1)$	$I_2 =$	$A(k(d_2-d_3+1)+d_1-1)$
$I_3 =$	$A(k(d_2-d_3+1)-d_1+2d_3-1)$	$I_3 =$	$A(k(d_2-d_3+1)-d_1+2d_3-1)$	$I_3 =$	$A(k(d_2-2d_1+d_3+1)+d_1-1)$
$P_o =$	$kAV_{DC}(-d_1(1+d_1-d_2-d_3)-d_2(d_2-1)-d_3(d_3-1))$	$P_o =$	$kAV_{DC}(-d_1(1+d_2-d_3)+d_2+d_3(1-d_3)$	$P_o =$	$kAV_{DC}(1-d_1)(d_2-d_1+d_3)$

4.7. SELECTION OF OPTIMIZATION METHOD

The selection of phase shift ratios for the SPS scheme is relatively straightforward, as only one control variable exists. However, DPS and TPS modulation schemes contain more than one control variable. Therefore, there exist infinite possible combinations of d_1, d_2, and d_3 to achieve an operating power for a given operating mode. As a result, phase shift ratios in the case of DPS and TPS need to be determined based on optimization objectives.

In [162], the authors have modified the DPS scheme by implementing various optimization strategies. Three different optimization strategies are considered: minimum reactive power, minimum peak current, and minimum RMS current. The efficiency of the converter has been compared over a wide voltage range for each of the optimization methods. It has been concluded that the peak current and RMS current optimization strategies performed the best. Similarly, authors in [163] performed a comprehensive comparison of modulation and control strategies for the DAB converter. It has been concluded that the Minimal Current Stress Optimization (MCSO) and Minimal RMS Current Optimization (MRMSCO) performed the best.

In this work, the determination of the phase shift ratios for both DPS and TPS will be carried out based on the peak current optimization for electrolysis. Contrary to the approach reviewed in [163], this work uses a different approach. The following assumptions have been made while conducting the optimization process:

- The effects of dead-time are neglected.
- The parasitic effects of the circuit are neglected for the sake of simplicity.

To perform peak current optimization, this work uses the `fmincon` function in MATLAB to determine the phase shift ratios for DPS and TPS schemes. The minimum of a problem is specified by,

$$\min_x f(x) \ni \begin{cases} c(x) \leq 0 \\ c_{\text{eq}}(x) = 0 \\ A_{\text{ineq}} \cdot x \leq b_{\text{ineq}} \\ A_{\text{eq}} \cdot x = b_{\text{eq}} \\ l \leq x \leq u \end{cases} \tag{4.93}$$

where $f(x)$ is the objective function that needs to be minimized.

The objective function for the peak current during electrolysis, $i_{\text{L(peak)}}$ for a given mode in both DPS and TPS schemes, is given by,

$$\boxed{i_{\text{L(peak)}}(d,k) = \max(K_0 I_0, K_1 I_1, K_2 I_2, K_3 I_3)} \tag{4.94}$$

Table 4.3: Selection of K_x for the modulation schemes and their associated modes under study.

Modulation	K_0	K_1	K_2	K_3
DPS-I	-1	-1	-1	1
DPS-II	-1	-1	-1	1
DPS-III	-1	-1	1	1
DPS-IV	-1	-1	-1	1
TPS-I	-1	-1	1	1
TPS-II	-1	-1	-1	1
TPS-III	-1	1	1	1

As the reaction during electrolysis continues, I_0 which has been considered as the peak current with reference to Fig. 4.4-4.10 and Fig. 4.13-4.17, may not necessarily be the peak current for the entire operating region of the electrolyzer. The peak current value keeps shifting between I_0, I_1, I_2, and I_3. By using (4.94), this shift in the peak current is taken into account over the entire operating region of the electrolyzer and across all modes of operation under study. Furthermore, it simplifies the formulation process of the objective function. Table 4.3 provides values for K_x in (4.94) for each modulation scheme and its associated modes.

Using (4.93), the peak current optimization problem for DPS and TPS can be defined,

$$\min_{d} i_{\mathrm{L(peak)}}(d,k) \ni \begin{cases} P_o(d,k) = P_{\mathrm{stack}} \\ A_{\mathrm{ineq}} \cdot d \leq b_{\mathrm{ineq}} \\ d_{\min} \leq d \leq d_{\max} \end{cases} \tag{4.95}$$

Table 4.4 and 4.5 provides the equality and inequality constraint matrices, A_{ineq}, A_{eq}, b_{ineq}, and b_{eq} for DPS and TPS, respectively. These inequality matrices are constructed based on the constraints on the phase shift ratios in each mode of DPS and TPS schemes, respectively.

Table 4.4: Equality and inequality matrices for DPS modulation

Parameter	Mode-I	Mode-II	Mode-III	Mode-IV
A_{ineq}	$\begin{bmatrix} 1 & -1 \\ 1 & 1 \end{bmatrix}$	$\begin{bmatrix} -1 & 1 \\ 1 & 1 \end{bmatrix}$	$\begin{bmatrix} 1 & -1 \\ -1 & -1 \end{bmatrix}$	$\begin{bmatrix} -1 & 1 \\ -1 & -1 \end{bmatrix}$
A_{eq}	0	0	0	0
b_{ineq}	$\begin{bmatrix} 0 & 1 \end{bmatrix}$	$\begin{bmatrix} 0 & 1 \end{bmatrix}$	$\begin{bmatrix} 0 & -1 \end{bmatrix}$	$\begin{bmatrix} 0 & -1 \end{bmatrix}$
b_{eq}	0	0	0	0

Table 4.5: Equality and inequality matrices for TPS modulation

Parameter	Mode-I	Mode-II	Mode-III
A_{ineq}	$\begin{bmatrix} -1 & -1 & 0 \\ 0 & 1 & -1 \end{bmatrix}$	$\begin{bmatrix} -1 & 1 & 0 \\ 1 & 0 & -1 \end{bmatrix}$	$\begin{bmatrix} 0 & 1 & -1 \\ -1 & 0 & 1 \end{bmatrix}$
A_{eq}	0	0	0
b_{ineq}	0	0	0
b_{eq}	0	0	0

The equality cost function for both DPS and TPS is given by,

$$\boxed{c_{\text{eq}}(d,k) = P_{\text{o}}(d,k) - P_{\text{stack}} = P_{\text{o}}(d,k) - v_{\text{stack}} i_{\text{stack}}} \tag{4.96}$$

where P_{o} is the output power for various operating modes of DPS and TPS from Tables 4.1 and 4.2. P_{stack} is the target operating power that needs to be achieved based on the electrolyzer's characteristics, which can be obtained using (2.1) - (2.4). d is the phase shift ratio matrix defined as $[d_1, d_2]$ for DPS, and $[d_1, d_2, d_3]$ for TPS. The lower and upper bounds are defined by $d_{\text{min}} = [0,0]$ and $d_{\text{max}} = [1,1]$ for DPS, and $d_{\text{min}} = [0,0,0]$ and $d_{\text{max}} = [1,1,1]$ for TPS. Fig. 4.19 illustrates the optimization scheme.

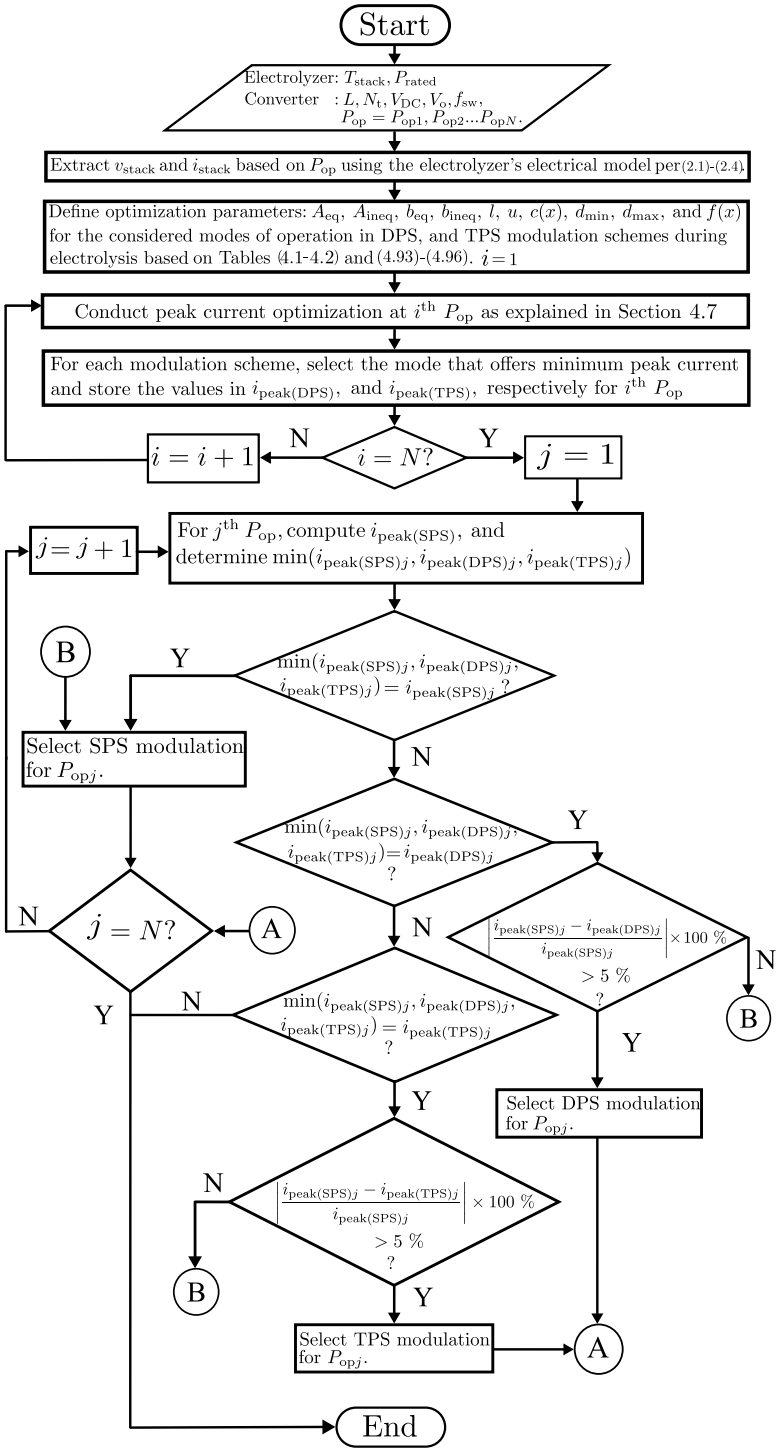

Figure 4.19: Flowchart to determine the optimal modulation scheme during electrolysis for peak current optimization

4.8. COMPARISON OF MODULATION STRATEGIES

Based on the peak current optimization scheme for electrolysis presented in the previous section, an analysis is carried out by comparing the primary transformer peak currents during electrolysis. Three different electrolyzers whose characteristics are illustrated in Fig. 4.20 are considered, each having a different power rating: 1 kW, 10 kW, and 100 kW, so as to additionally consider the effect of rated power. The phase shift ratios for DPS and TPS schemes, and therefore, the resulting peak currents, are determined based on the peak current optimization scheme described in the previous section. Electrolyzers are unique, non-linear, low-voltage, and high-current loads. To showcase this distinction, a similar analysis is carried out for a 500 V CV load (high-voltage and low-current load) for the same power rating.

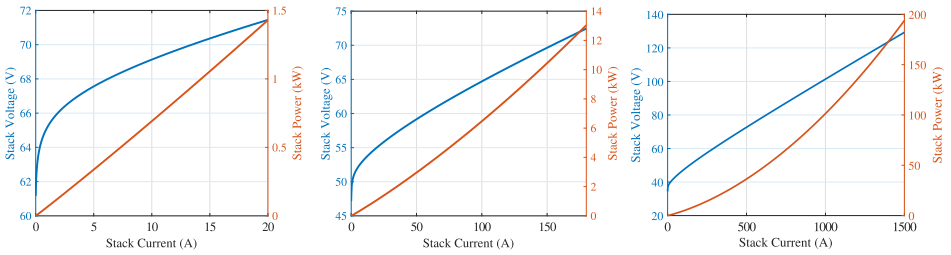

Figure 4.20: Electrical characteristics of electrolyzer considered in this work, (a) 1 kW, (b) 10 kW, and (c) 100 kW.

Tables 4.6 and 4.7 showcase the DAB converter specifications for each case. The peak currents on the primary side of the transformer were measured for 19 operating power points: starting from 10% of rated power to the rated power.

Table 4.6: Considered DAB converters for electrolyzers

Parameters	**1 kW**	**10 kW**	**100 kW**
V_{DC}	500 V	1400 V	1400 V
V_o	70 V	70 V	100 V
N_t	7:1	20:1	14:1
L	580 μH	580 μH	50 μH
f_{sw}	20 kHz	20 kHz	20 kHz
C_o	210 μF	440 μF	6.3 mF

Table 4.7: Considered DAB converters for CV loads

Parameters	1 kW	10 kW	100 kW
V_{DC}	1400 V	1400 V	1400 V
V_o	500 V	500 V	500 V
N_t	2.8:1	2.8:1	2.8:1
L	580 μH	580 μH	50 μH
f_{sw}	20 kHz	20 kHz	20 kHz
C_o	210 μF	440 μF	6.3 mF

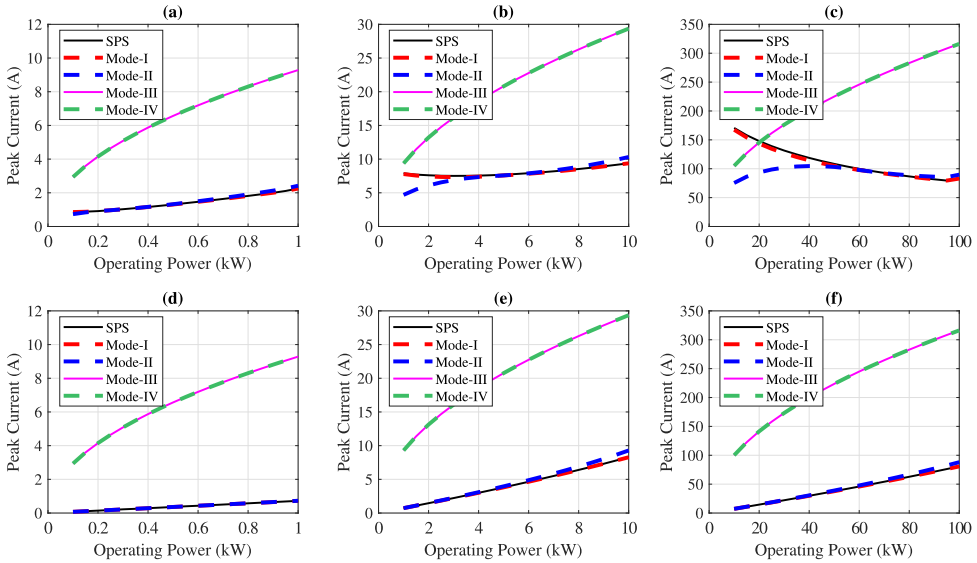

Figure 4.21: Comparison of studied DPS modes with conventional SPS operation for electrolyzer and CV loads: (a) 1 kW electrolyzer, (b) 10 kW electrolyzer, (c) 100 kW electrolyzer, (d) 1 kW CV load, (e) 10 kW CV load, and (f) 100 kW CV load.

Fig. 4.21 showcases a comparison of the transformer primary peak currents between DPS and SPS operation based on the analytical results of peak current optimization. For 1 kW and 10 kW electrolyzers, DPS Mode-I and SPS perform the best for both the loads, achieving minimum peak current until 0.4 kW and 5.5 kW, respectively. In both cases, DPS Mode-II offers the lowest peak current below 0.2 kW and 4 kW, respectively. However, in the case of the 100 kW power level, while DPS Mode-I/SPS performed the best overall for the CV load, this is not the case for the electrolyzer load. In the electrolyzer load, as the operating power begins to decrease, the peak currents for DPS Mode-I and SPS begin to increase. At an operating power close to 50 kW, a crossover is observed between the DPS Mode-I/SPS and DPS Mode-II. Below 50 kW power, DPS Mode-II performs the best by achieving the lowest peak current compared to the DPS Mode-I, Mode-III, Mode-IV, and SPS.

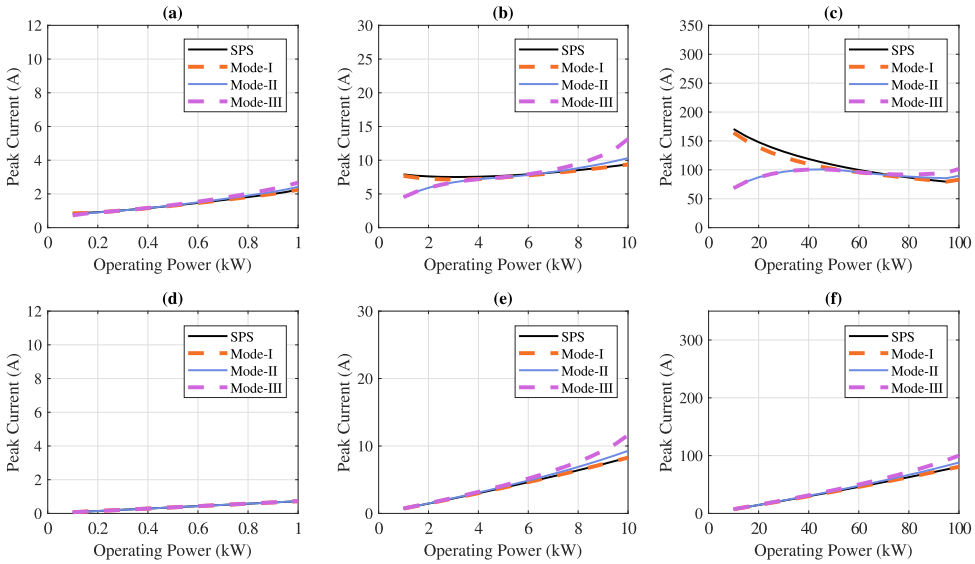

Figure 4.22: Comparison of studied TPS modes with conventional SPS operation for electrolyzer and CV loads: (a) 1 kW electrolyzer, (b) 10 kW electrolyzer, (c) 100 kW electrolyzer, (d) 1 kW CV load, (e) 10 kW CV load, and (f) 100 kW CV load.

Similarly, Fig. 4.22 showcases the transformer primary peak currents based on the peak current optimization for the TPS modulation scheme, as well as during the SPS modulation scheme for electrolyzer and CV load for the considered test cases. For the test case of 1 kW CV load, SPS and all the TPS modes of operation provide the same value of peak current for a given operating power. On the other hand, there are minor differences observed during electrolysis. At the rated power, TPS Mode-I and SPS offer the lowest possible peak current, followed by TPS Mode-II, and finally TPS Mode-III. However, this trend begins to change as the operating power begins to decrease. As operating power approaches 400 W, the peak currents obtained with TPS Mode-III begin to decrease and therefore align with the peak currents of TPS Mode-I, TPS Mode-II, and SPS at 400 W. Below 200 W, the crossover finally occurs, wherein TPS Mode-II and TPS Mode-III provide the lowest possible peak current. For the case of 10 kW and 100 kW CV load, the peak currents showcase a relatively similar trend. At the rated power, TPS Mode-I and SPS provide the lowest possible peak current. As the operating power decreases, the difference in performance between the TPS modes and SPS begins to decrease, too. However, this is not the case for the 10 kW and 100 kW electrolyzers. The difference in performance is clearly observed for these test cases in contrast to the 1 kW electrolyzer discussed previously. For both the electrolyzer loads, TPS Mode-I and SPS performed the best, followed by TPS Mode-II and TPS Mode-III. As the operating power decreased, a crossover was achieved at 6 kW, below which, TPS Mode-II and TPS Mode-III outperformed TPS Mode-I and SPS. A similar trend is observed for the 100 kW electrolyzer. The crossover occurs between 60 kW and 80 kW. TPS Mode-II and TPS Mode-III outperform TPS Mode-I and SPS by a significant margin.

Using Fig. 4.21(a)-(c) and Fig. 4.22(a)-(c), comparison of studied DPS modes and TPS modes is carried from the context of peak current reduction with SPS modulation as a baseline. This comparison is illustrated in Fig. 4.23 and Fig. 4.24, where positive percentage values indicating improvement, while negative percentage values indicating worse performance.

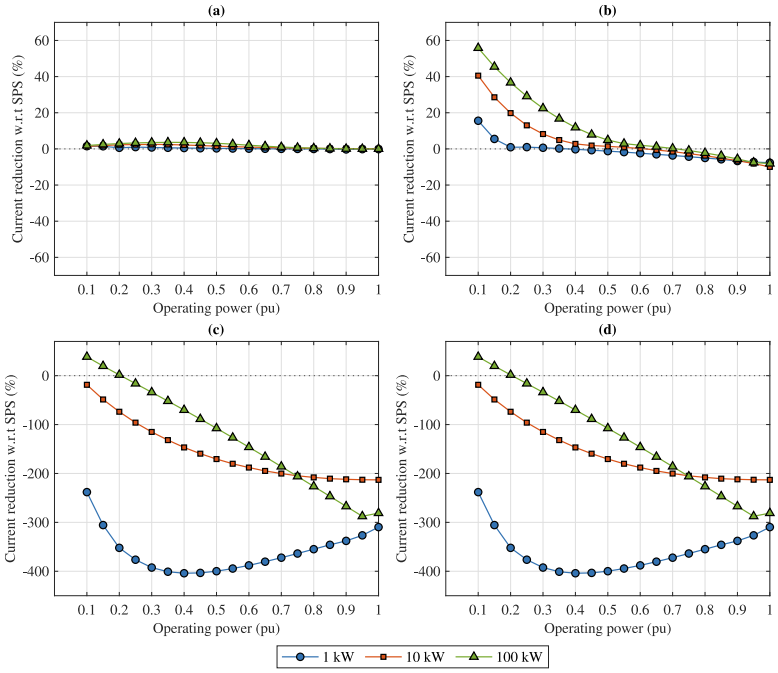

Figure 4.23: Comparison of studied DPS modes with conventional SPS operation from the context of peak current reduction during electrolysis: (a) DPS Mode-I, (b) DPS Mode-II, (c) DPS Mode-III, (d) DPS Mode-IV.

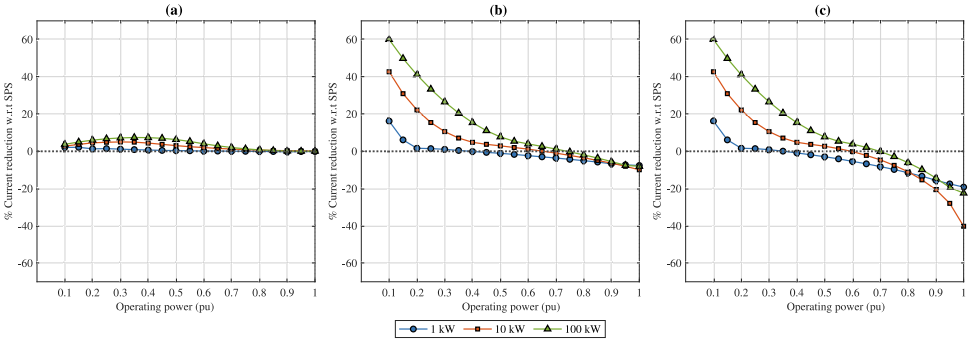

Figure 4.24: Comparison of studied TPS modes with conventional SPS operation from the context of peak current reduction during electrolysis: (a) TPS Mode-I, (b) TPS Mode-II, (c) TPS Mode-III.

In DPS Mode-I, peak current reduction is nearly identical to SPS, with only a minor reduction of 3.62% at 0.35 pu for the 100 kW electrolyzer as illustrated in Fig. 4.23(a). In contrast, DPS Modes II–IV underperforms near rated power but achieves substantial improvements at lower operating points. At 0.1 pu, DPS Mode-II reduces peak current by 55.83%, 40.52%, and 15.09% for the 100 kW, 10 kW, and 1 kW electrolyzers, respectively, as shown in Fig. 4.23(b). Modes-III and Mode-IV show similar behavior, with the 100 kW electrolyzer reaching 38.51% reduction at 0.1 pu as shown in Fig. 4.23(c)-(d).

In case of TPS modulation, TPS Mode-I resembled DPS Mode-I but delivered greater peak current reduction for the 100 kW case, achieving 7.41% reduction at 0.35 pu as illustrated in Fig. 4.24(a). TPS Modes II and III, while less effective near rated power, provide significant peak current reduction at low power levels. At 0.1 pu, both modes achieved reductions of 60% (100 kW), 42.71% (10 kW), and 15.75% (1 kW), as shown in Fig. 4.24(b)-(c).

Each mode of operation in both DPS and TPS is optimized for the lowest possible peak current it can offer while strictly operating in that specific mode. However, additional steps need to be considered so that the best possible mode of operation among all three modulation schemes can be considered for optimal operation of the converter during electrolysis. The detailed steps, as illustrated in Fig. 4.19, showcase subsequent steps post optimization scheme in order to obtain an optimized operating trajectory for the converter during electrolysis by selecting the best possible mode of operation among the studied modulation schemes.

The determination of an optimal modulation scheme mainly depends on evaluating the deviation between the peak current during SPS modulation and either the DPS or the TPS modulation scheme.

$$\boxed{\left|\frac{i_{\text{peak(SPS)}} - i_{\text{peak(X)}}}{i_{\text{peak(SPS)}}}\right| \times 100\% > \epsilon} \tag{4.97}$$

X in (4.97) can either be SPS, DPS, or TPS.
With reference to the flowchart illusrated in Fig. 4.19, the optimal operating trajectory of the converter during electrolysis is determined for the considered power levels, as illustrated in Fig. 4.25. Operation under the SPS scheme is used as the reference. To highlight the effect of the deviation threshold, ϵ, Fig. 4.25 presents the optimized trajectories of the DAB converter for 1 kW, 10 kW, and 100 kW electrolyzers at $\epsilon = 2\%$, $\epsilon = 5\%$, and $\epsilon = 10\%$ illustrated in Fig. 4.25(a)-(c), Fig. 4.25(d)-(f), and Fig. 4.25(g)-(i), respectively.

For a deviation threshold of $\epsilon = 2\%$, the preferred operation varies with electrolyzer size. In the case of 1 kW electrolyzer, TPS Mode-III is selected up to 200 W, after which the converter transitions to SPS modulation for the remainder of the operating range, as shown in Fig. 4.25(a). In the case of 10 kW electrolyzer, TPS Mode-III is used up to 4 kW, TPS Mode-I is selected between 4 kW and 6.5 kW, and SPS modulation is applied above 6.5 kW, as shown in Fig. 4.25(b). In the case of 100 kW electrolyzer, TPS Mode-III is preferred up to 60 kW, TPS Mode-I between 60 kW and 75 kW, and SPS modulation beyond 75 kW, as shown in Fig. 4.25(c).

For this work, a baseline deviation threshold of $\epsilon = 5\%$ is considered. In the case of 1 kW electrolyzer, SPS modulation is favored for most of the operating range, except below 200 W where TPS Mode-III is selected. In this region, a peak current reduction of up to 15.75% at 100 W is achieved as shown in Fig. 4.25(d). In the case of 10 kW electrolyzer, SPS modulation is preferred above 4 kW, while below this level, TPS Mode-III provides superior performance, yielding a peak current reduction of up to 42.71% at 1 kW, as shown in Fig. 4.25(e). Similarly, for the 100 kW electrolyzer, SPS modulation is selected above 60 kW, and TPS Mode-III is used below 60 kW, resulting in a peak current reduction of up to 60% at 10 kW, as shown in Fig. 4.25(f).

For a higher deviation threshold of $\epsilon = 10\%$, SPS modulation becomes dominant. In the 1 kW electrolyzer, TPS Mode-III is applied only up to 150 W, with SPS modulation covering the remainder of the range, as shown in Fig. 4.25(g). In the 10 kW case, TPS Mode-III is preferred below 3.5 kW and SPS above this point, as shown in Fig. 4.25(h). For the 100 kW electrolyzer, TPS Mode-III is selected up to 50 kW, while SPS modulation is used for higher power levels, as shown in Fig. 4.25(i).

The results in Figs. 4.25(a)-(i) show that a lower deviation threshold (ϵ) enables utilization of different modulation schemes and their associated modes. Conversely, a higher ϵ minimizes transitions, leading to operation primarily in the SPS scheme.

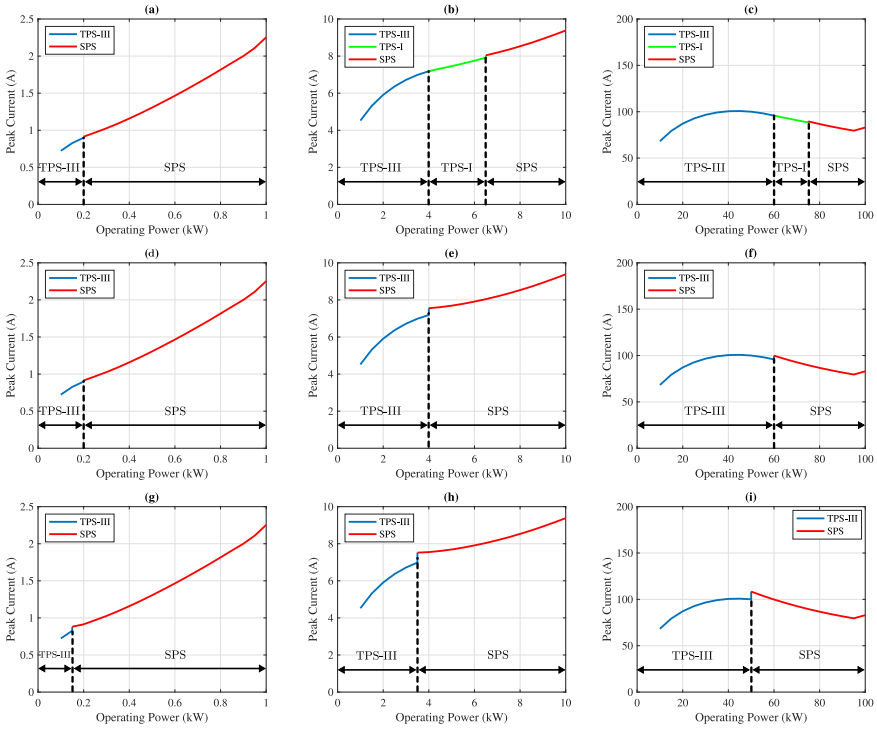

Figure 4.25: Optimized operation for electrolysis based on deviation threshold: $\epsilon = 2\%$: (a) 1 kW, (b) 10 kW, and (c) 100 kW. $\epsilon = 5\%$: (d) 1 kW, (e) 10 kW, and (f) 100 kW. $\epsilon = 10\%$: (g) 1 kW, (h) 10 kW, and (i) 100 kW.

Another important observation is that the region where SPS modulation is preferred decreases as the rated electrolyzer power increases. For low-power electrolyzers, SPS provides the lowest peak current across most of the operating range, with TPS Mode-III applied only near the lower power limit, as shown in Fig. 4.25(d). However, for medium and high power electrolyzers, TPS becomes essential. The SPS scheme cannot minimize peak current effectively at lower operating points, which can result in increased reactive power within the system. In these cases, TPS outperforms both SPS and DPS, as demonstrated in Fig. 4.25(e)-(f).

4.9. EXPERIMENTAL SETUP AND RESULTS

Table. 4.8 showcases the specifications of the designed prototype. Tables 4.9-4.12 provide specifications regarding the chosen semiconductor switch, gate-driver, series inductor, and the HF transformer designed for the 1 kW prototype in this work.

Table 4.8: Converter Specifications

Parameter	
P_o	1 kW
V_{DC}	500 V
V_o	70 V
f_{sw}	20 kHz
C_{in}, C_o	210 μF

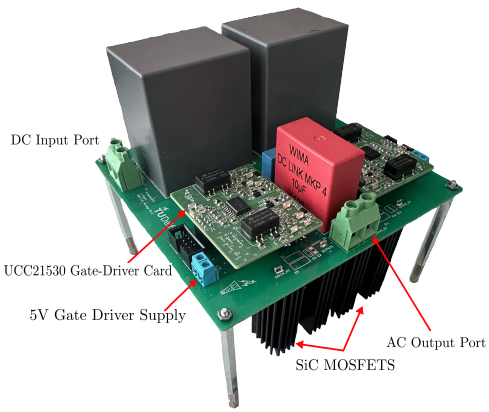

Figure 4.26: H-Bridge board.

Table 4.9: Selected semiconductor switch.

Parameter	
Model	AIMZH120R020M1T
Technology	SiC
Package	TO-247-4
V_{DS}	1.2 kV
$R_{DS(on)}$	19 mΩ
$R_{G(int)}$	2.2 Ω
I_D	100 A

Table 4.10: Selected gate-driver.

Parameter	
Model	UCC21530
Isolation	Reinforced
Configuration	Half-Bridge
I_{source}	4 A
I_{sink}	6 A
$R_{G(selected)}$	5.11 Ω
t_{dead}	110 ns

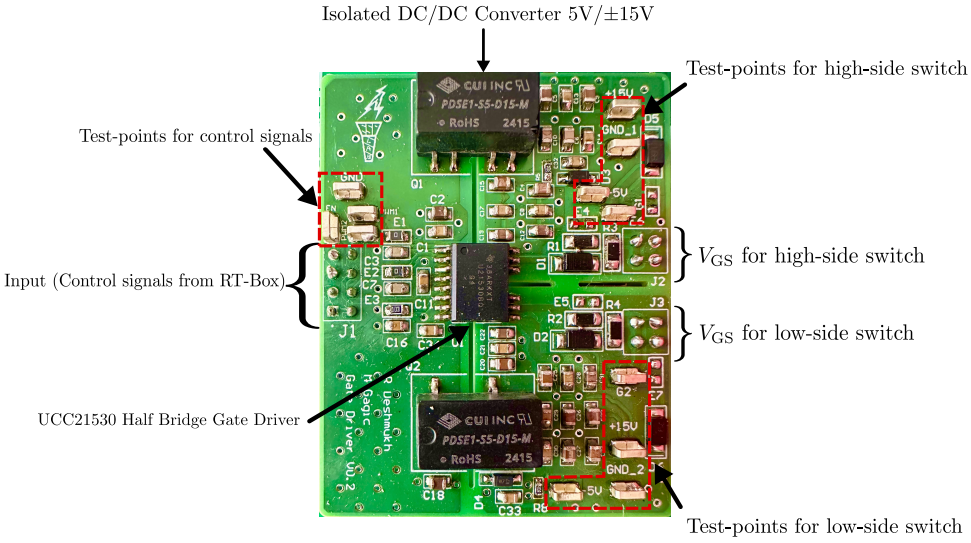

Figure 4.27: UCC21530 half-bridge gate driver card.

Table 4.11: HF Transformer Specifications

Parameters	
Selected core shape	PM74/59
Core material	N87
N_t	7:1
N_p	56
Selected primary conductor type	Litz Wire
Number of strands (primary)	600
$d_{p(effective)}$	1.54 mm
$d_{p(strand)}$	0.063 mm
N_{sec}	8
Selected secondary conductor type	Litz Wire
Number of strands (secondary)	910
$d_{s(effective)}$	2.15 mm
$d_{s(strand)}$	0.071 mm

Table 4.12: Series Inductor Specifications

Parameters	
Selected core shape	E70/33/22
Core material	N87
Number of turns	22
l_g	1.4 mm
Selected conductor type	Litz Wire
Number of strands	600
$d_{p(effective)}$	1.54 mm
$d_{p(strand)}$	0.063 mm

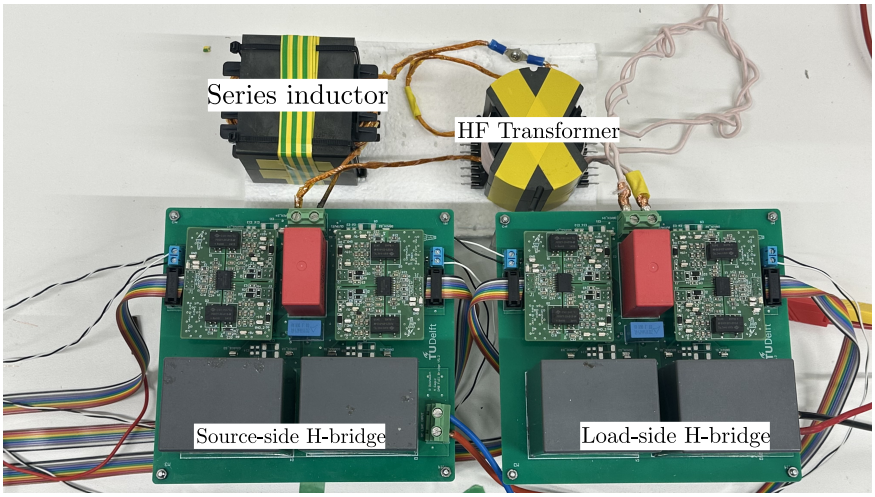

Figure 4.28: Prototype connections showcasing the H-bridge boards and magnetics.

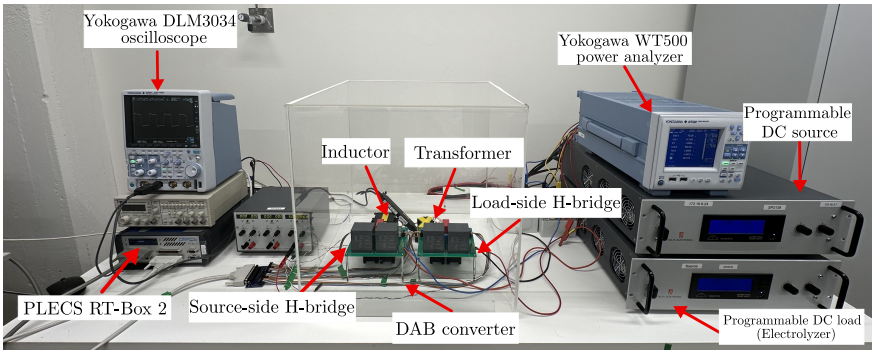

Figure 4.29: Experimental Setup

4

Fig. 4.26 showcases one of the H-bridge boards of the designed DAB prototype, while Fig. 4.28 showcases both H-bridges connected together via the designed magnetics. Fig. 4.29 showcases the complete experimental setup for this work. The prototype is operated in open-loop using PLECS RT-Box 2 by implementing the modulation logic within the PLECS environment. Based on the identified optimal operating trajectory, the phase shift ratios are defined in a lookup table within PLECS. One of them is programmed as a DC source and set at 500 V, while the other is configured as a DC load that follows the electrical characteristics of the 1 kW electrolyzer. The efficiency measurement has been carried out with the help of a Yokogawa WT500 power analyzer. The peak value of the primary-side transformer current is measured using a Yokogawa DLM3034 oscilloscope.

The prototype is operated to follow along the optimal operation curve, as shown in Fig. 4.25(a). On the other hand, in order to validate the 10 kW and 100 kW cases, equivalent Simulink models are made to operate along their respective optimal operation curves.

Table 4.13: Comparison of simulation and experimental results of the 1 kW prototype

Operating Power (kW)	Selected Mode	Simulation (A)	Experiment (A)
0.1	TPS-III	0.74	0.73
0.2	SPS	0.93	0.89
0.3	SPS	1.03	1.01
0.4	SPS	1.16	1.13
0.5	SPS	1.30	1.28
0.6	SPS	1.46	1.47
0.7	SPS	1.63	1.61
0.8	SPS	1.81	1.96
0.9	SPS	2.00	2.20
1	SPS	2.28	2.60

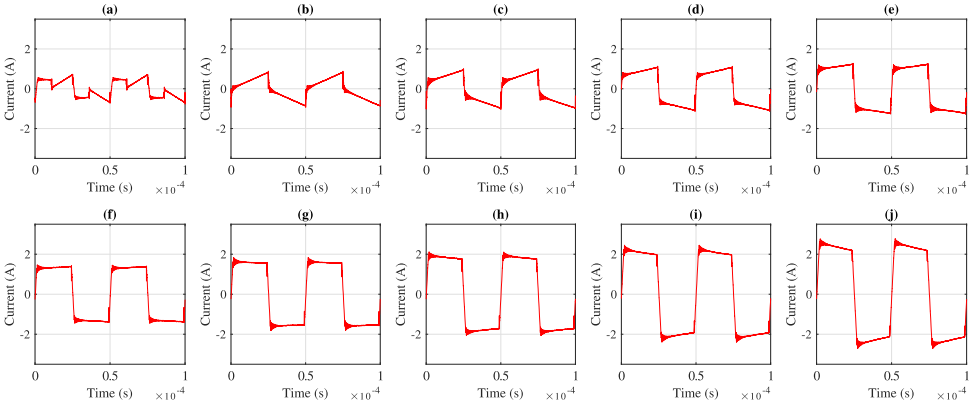

Figure 4.30: Experimental results of primary transformer current: TPS-III in (a) 100 W, SPS in (b) 200 W, (c) 300 W, (d) 400 W, (e) 500 W, (f) 600 W, (g) 700 W, (h) 800 W, (i) 900 W, and (j) 1 kW.

Table 4.14: Comparison of the optimization results with the simulation results of the 10 kW system

Operating Power (kW)	Selected Mode	Calculated optimized current (A)	Simulation (A)
1	TPS-III	4.60	4.67
2	TPS-III	5.80	5.82
3	TPS-III	6.63	6.53
4	SPS	7.44	7.33
5	SPS	7.57	7.45
6	SPS	7.77	7.83
7	SPS	8.04	8.09
8	SPS	8.38	8.40
9	SPS	8.77	8.79
10	SPS	9.22	9.23

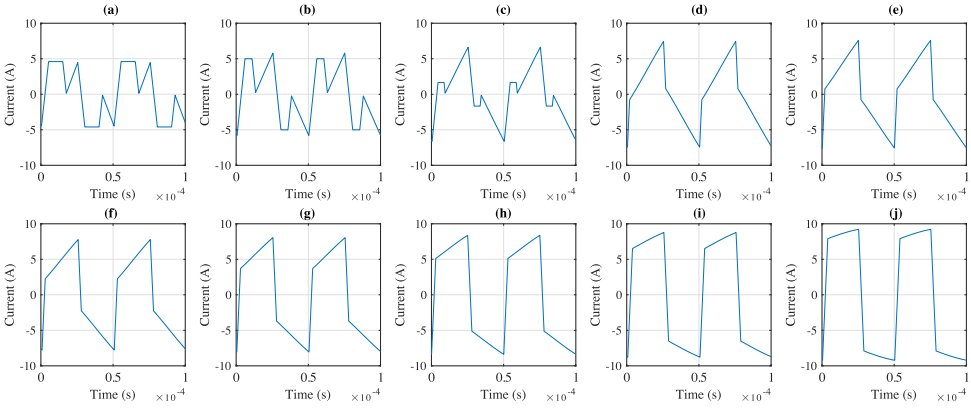

Figure 4.31: Simulation results of primary transformer current: TPS-III in (a) 1 kW, (b) 2 kW, (c) 3 kW, SPS in (d) 4 kW, (e) 5 kW, (f) 6 kW, (g) 7 kW, (h) 8 kW, (i) 9 kW, and (j) 10 kW.

Table 4.15: Simulation results of the 100 kW system

Operating Power (kW)	Selected Mode	Calculated optimized current (A)	Simulation (A)
10	TPS-III	68.25	68.56
20	TPS-III	87.16	87.46
30	TPS-III	96.64	96.73
40	TPS-III	100.50	100.3
50	TPS-III	100.03	99.54
60	SPS	99.84	99.46
70	SPS	92.70	92.2
80	SPS	86.70	86.09
90	SPS	81.70	80.96
100	SPS	83.0	84.16

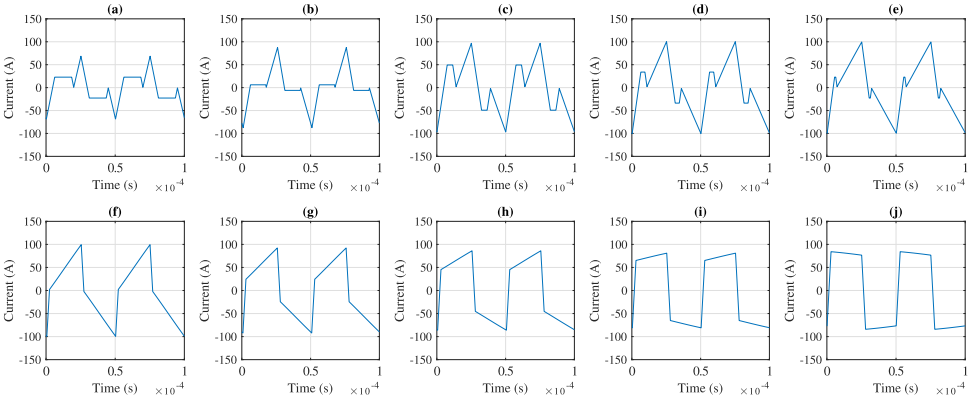

Figure 4.32: Simulation results of primary transformer current: TPS-III in (a) 10 kW, (b) 20 kW, (c) 30 kW, (d) 40 kW, (e) 50 kW, SPS in (f) 60 kW, (g) 70 kW, (h) 80 kW, (i) 90 kW, and (j) 100 kW.

Table 4.13 provides a comparison of peak currents measured from the experimental setup against the simulation model operating on the optimized phase shift ratios for the 1 kW system, and Fig. 4.30 showcases the primary transformer currents obtained from the prototype. On the other hand, Tables 4.14 and 4.15 provide a comparison between peak currents of simulation results against the value of the objective function of the optimization problem for the 10 kW and 100 kW systems, respectively. Fig. 4.31 and 4.32 showcase the primary transformer currents for the 10 kW and 100 kW systems, respectively.

The phase shift ratios determined by the optimization scheme correctly result in the expected primary peak transformer current during electrolysis for the 1 kW case. On the other hand, simulation results for the 10 kW and 100 kW cases are in accordance with the peak current values obtained through the defined objective function for the optimization scheme, showcasing that the proposed optimized operating trajectory for the converter during electrolysis effectively helps minimize the peak transformer current at lower operating power points during electrolysis.

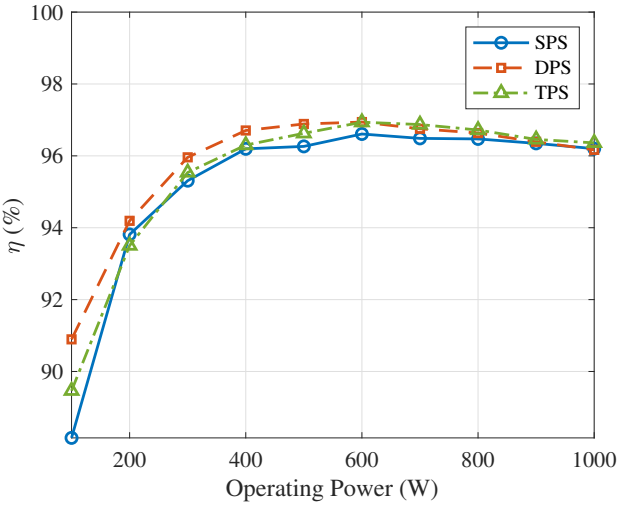

Figure 4.33: Measured efficiencies of the 1 kW prototype operating in SPS, DPS, and TPS modulation schemes.

Fig. 4.33 presents the measured efficiencies of the 1 kW experimental prototype operating under SPS, DPS, and TPS modulation schemes during electrolysis. At the rated power of 1 kW, all three schemes exhibit nearly identical efficiencies, with SPS at 96.20%, DPS at 96.17%, and TPS at 96.36%. This convergence occurs because, at rated power, DPS and TPS effectively operate in a manner similar to SPS, as described in Section 4.5. As the operating power decreases, the efficiency of SPS begins to drop, while DPS and TPS maintain similar trends and even show slight improvements up to 600 W. Below 600 W, TPS efficiency gradually declines and falls slightly below that of DPS. At 100 W, DPS demonstrates the highest efficiency at 90.89%, followed by TPS at 89.46%, and SPS at 88.15%. In this work, peak current optimization was employed, which results in TPS modulation achieving the lowest peak current at 100 W. However, TPS exhibits a slightly higher RMS current compared to DPS. As a result, DPS delivers higher efficiency due to its lower RMS current, despite having a slightly higher peak current than TPS.

4.10. CONCLUSION

This chapter has investigated state-of-the-art modulation schemes for the DAB converter with a focus on electrolysis applications. Due to their nonlinear, low-voltage, and high-current characteristics, electrolyzers pose distinct challenges compared to conventional CV loads. A comparative analysis across SPS, DPS, and TPS modulation schemes using peak primary transformer current as the evaluation metric has been conducted at three power levels: 1 kW, 10 kW, and 100 kW. To achieve this, a peak current optimization method based on MATLAB's `fmincon` function was developed to determine optimal phase shift ratios for DPS and TPS schemes. The results revealed

that electrolyzers exhibit fundamentally different behavior than CV loads under the same operating conditions, highlighting the need to study modulation strategies for electrolysis.

Extending the optimization scheme, optimized operating trajectories for the DAB converter have been identified for each power level. While SPS remains the most effective for low-power electrolyzers, it proves suboptimal at medium to high power due to increased circulating currents and reactive power—issues that can be significantly mitigated with DPS and TPS schemes.

The proposed optimization framework was validated through experiments using a 1 kW, 20 kHz prototype and simulations for 10 kW and 100 kW systems. The optimized trajectories resulted in peak current reductions of up to 15.75% at 100 W for the 1 kW system, 42.71% at 1 kW for the 10 kW system, and 60% at 10 kW for the 100 kW system, compared to conventional SPS operation.

5

REAL-TIME DIGITAL TWIN OF DAB-ELECTROLYZER SYSTEM

This chapter presents a closed-loop RTDT of a 10 kW Dual Active Bridge (DAB)-electrolyzer system using OP4610-XG real-time simulator. Furthermore, to address the challenge of visualizing and analyzing the high-frequency quantities within the intermediate AC conversion stage of the DAB converter, the eHS toolbox is utilized for real-time simulation of power electronics within the FPGA. A comparison of the RTDT results with offline PLECS simulation indicates that the developed RTDT accurately operates along the 10 kW AEL's electrical characteristics, and at the same time, an accurate visualization of the intermediate HF AC quantities, especially the transformer currents, is achieved with this implementation. Thus, this setup exhibits the potential and provides a foundation to evaluate designs of PECs for electrolyzers.

Chapter published in R. S. Deshmukh, G. Rituraj, P. Bauer and H. Vahedi, "Real-time digital twin implementation of power electronics-based hydrogen production system," in *Energy Reports*, vol. 13, pp. 5006-5015, 2025.

5.1. INTRODUCTION

Testing and evaluating PECs for electrolysis applications present notable challenges, primarily due to the safety risks associated with hydrogen generation. In many systems, the power supply and electrolyzer are housed within a standard enclosure, making it hazardous to test new converter designs under real operating conditions. Any abnormal behavior or fault during testing can lead to unsafe situations.

To mitigate these risks, a DT can be developed as a virtual replica of the physical PEC. This enables non-intrusive, flexible, and safe evaluation of converter performance across a wide range of scenarios without requiring direct interaction with the actual electrolyzer.

As discussed in Section 1.2.3, DT technology has been widely adopted in various domains, with significant applications in power electronics. However, its use in testing PECs with multi-stage conversions specifically for electrolyzer systems remains limited and largely unexplored.

This chapter bridges that gap by presenting an RTDT setup for a DAB-electrolyzer system, focusing on the following:

- The real-time simulation model architecture has been explained in detail for the chosen real-time simulator by using the top-down approach.
- RTDT models are not similar to standard offline simulation models. The offline simulation model elements need to be divided such that they fall under two types of subsystems within the RTDT model. A standard offline simulation model of a closed-loop current-controlled 10 kW DAB-electrolyzer system is utilized for this work and is converted to a hybrid Simulink-based RT-Lab model along with a detailed explanation.
- The RTDT model is validated with offline simulations in PLECS for a given stack temperature. Furthermore, the RTDT model is subjected to different test cases of stack temperature to validate its operation along with the electrical characteristics of the electrolyzer.

5.2. OPAL-RT REAL-TIME SIMULATION PLATFORM

The OP4610XG real-time simulator, developed by OPAL-RT Technologies, was used in this work. This simulator's comprehensive system includes a Kintex 7 FPGA. It has a robust target computer, a high-speed, flexible front-end processor, and a signal conditioning stage. The target computer is located in the lower part of the chassis and can function as an independent, standalone computer in its standard configuration [164].

Figure 5.1: OP4610-XG real-time simulator

Table 5.1: Real-Time Simulator Specifications

(a) Target Computer Specifications

	Description
Model	OP4610XG
Operating System	OPAL-RT Linux 3.4.1
Central Processing Unit (CPU)	AMD Ryzen 5 3600XT, 6-Core, 3.8 GHz
Memory (RAM)	8 GB

(b) FPGA Specifications

	Description
Model	Kintex 7 TE0741
Number of Analog Channels	16 (Both input and output)
Analog Input Card Model	OP5340 (Input Range: ±20 V to ±30 V)
Analog Output Card Model	OP5330 (Output Range: ±5 V, ±10 V, ±16 V)
Number of Digital Channels	32 (Bidirectional)
Digital input-output card model	OP5369
Digital input specifications:	Voltage Range: 0 to 30 V DC, Turn-on delay: 10 ns, Turn-off delay: 15 ns
Digital output specifications	Voltage range: 4.5 to 25 V DC, Turn on delay: < 90 ns (5 V) and <100 ns (25 V) Turn off delay: < 90 ns (5 V) and <100 ns (25 V)
Output Frequency	up to 4 MHz

5.3. REAL-TIME SIMULATION MODEL ARCHITECTURE

Fig. 5.2 showcases a hybrid electrical-block diagram representation of the DAB-electrolyzer system to be implemented as an RTDT.

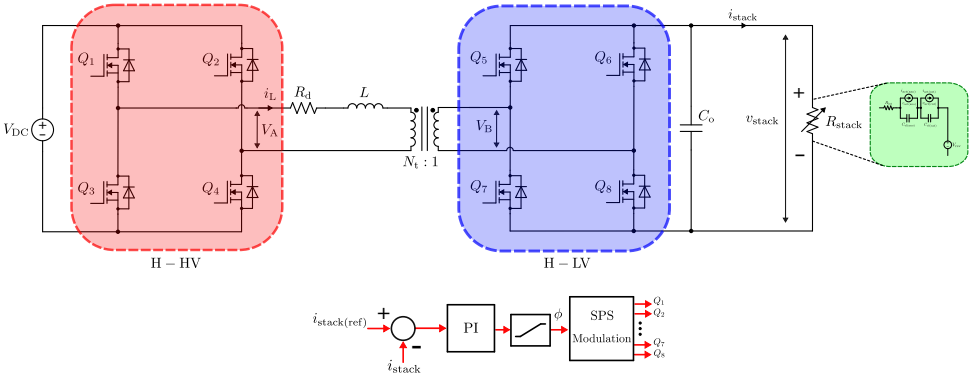

Figure 5.2: DAB-Electrolyzer system to be implemented within the RTDT.

A MATLAB Simulink model is unsuitable for direct real-time simulation using OPAL-RT. Fig. 5.3 illustrates a typical top-level layout of a Simulink model adapted for use within a real-time simulator. This model is organized into two main subsystems: the graphical user interface (GUI), labeled with the prefix "SC_", and the computational subsystem, labeled "SM_". The SC_GUI subsystem incorporates all monitoring elements, such as scopes and displays, and input mechanisms like constant blocks and sliders. Conversely, the SM_COMPUTE subsystem includes essential functions and, crucially, the plant model, designed to operate on the FPGA/CPU of the real-time simulator.

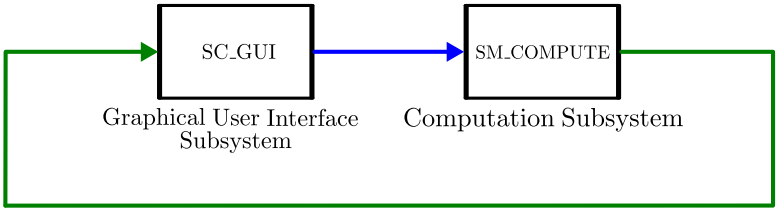

Figure 5.3: Top-level structure of the Simulink-based real-time simulation model.

Fig. 5.4 illustrates a closed-loop RTDT of a DAB converter integrated with the 10 kW AEL. The detailed structure of the graphical user interface subsystem, SC_GUI, and the computation subsystem, SM_COMPUTE, has been showcased here. The structure of both these subsystems is explained briefly in subsequent sections.

5.3.1. GRAPHICAL USER INTERFACE SUBSYSTEM (SC_GUI)

For this RTDT, the SC_GUI subsystem consists of input parameters such as f_{sw}, D, t_{dead}, disable (for blocking PWM signals), and pu loading (stack current). These

parameters can be tuned while the RTDT is online. If information from either the SM_COMPUTE subsystem must be monitored or inputs must be acquired from the SC_GUI subsystem, the information must pass through an OPCOMM block. The OPCOMM block is necessary for simulating real-time communication links [165].

5.3.2. COMPUTATION SUBSYSTEM (SM_COMPUTE)

The CPU of the OP4610-XG simulator can compute at a minimum time step of $T_{\text{disc}} = 5\ \mu$s. This time step has also been utilized for the current CPU system of the real-time simulator. However, it mainly depends on the model complexity and switching frequency. However, PECs often operate at higher switching frequencies, ranging from tens to hundreds of kilohertz. Under these conditions, relying entirely on the CPU for computations may not be advisable due to its time-step limitations, which can lead to overrun conditions and subsequent data loss. Consequently, utilizing the FPGA of the simulator is essential, as it can handle computations with time steps on the order of tens of nanoseconds. Power electronics circuits can be simulated in real-time using the eHS toolbox. This toolbox provides an electrical solver for the FPGA ,specifically for simulating power electronics circuits. It includes a schematic editor that facilitates integrating inputs from Simulink and FPGA and routing outputs to the Simulink scopes within the SC_GUI subsystem and the FPGA's output channels.

Table 5.2: PWM OUT Configuration

Parameter	Value
Number of PWM signals	2
Polarity	Active high
Carrier wave	Asymmetric (Sawtooth)
Output complementary channel	Yes

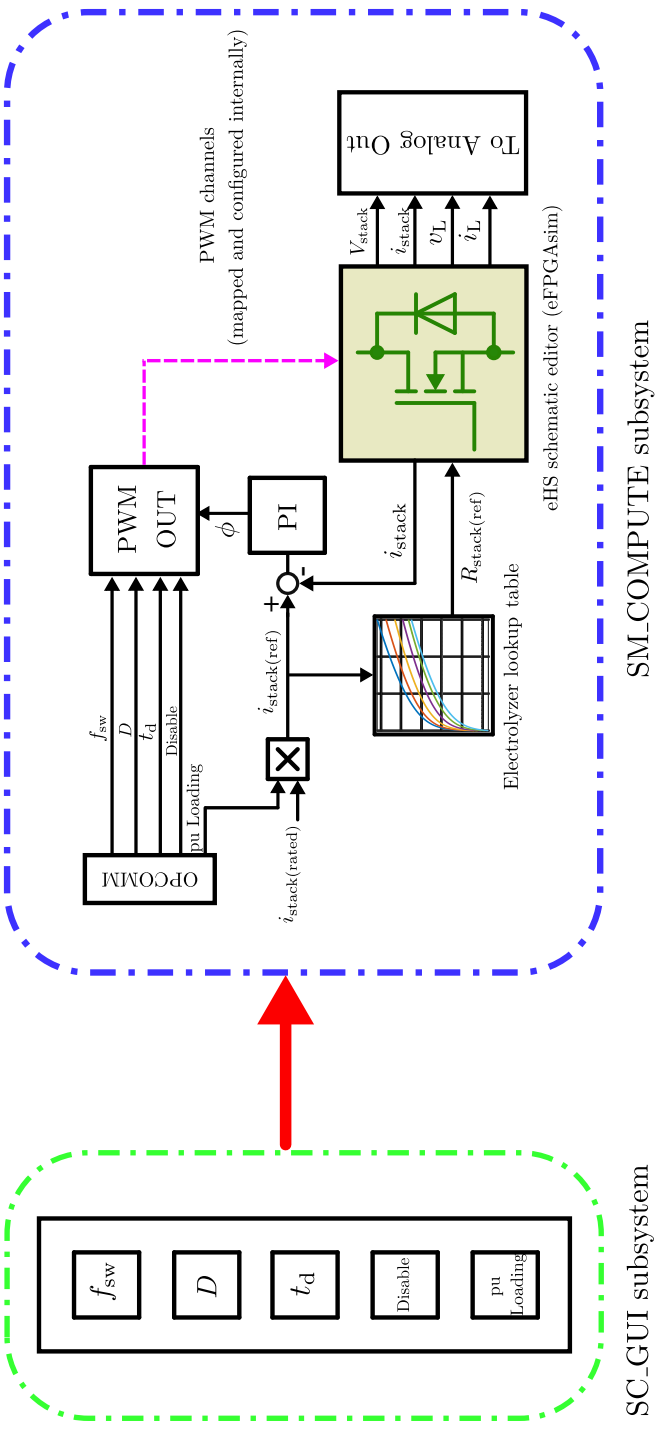

Figure 5.4: Detailed structure of the closed-loop RTDT of a DAB converter integrated with the 10 kW AEL.

The computation subsystem is illustrated in Fig. 5.4. Input parameters are acquired from the SC_GUI subsystem through the OPCOMM block. These parameters are essential for generating the PWM signals needed to control the semiconductor switches in the DAB converter and are supplied to the PWM OUT block. The PWM OUT block sets up the simulator's bidirectional digital I/O card to function in PWM mode. The configurations of the PWM OUT block, critical for this real-time digital twin, are presented in Table 5.2. Note that the complementary channels are automatically generated based on the number of activated PWM channels. For the current system, two PWM channels are activated for switch pairs Q_1-Q_4, and Q_5-Q_8. On the other hand, the complementary switch pairs, Q_2-Q_3, and Q_6-Q_7 are driven by the complementary signals generated based on the initially activated PWM channels.

Using the eHS schematic editor, the PWM signals from the PWM OUT block are internally mapped to the corresponding digital channels and, therefore, the appropriate switches. The DAB converter itself is constructed within the eHS schematic editor. Any circuit defined within this schematic editor is considered a part of the FPGA computation. An FPGA time-step of $T_{\text{disc}} = 120$ ns was chosen for the current system. Referring to Chapter 2, the electrolyzer characteristics, derived from experimental data obtained from the literature [144] and presented in Table 2.2, along with the stated assumptions, will be used to model the electrolyzer within the DAB-electrolyzer RTDT setup.

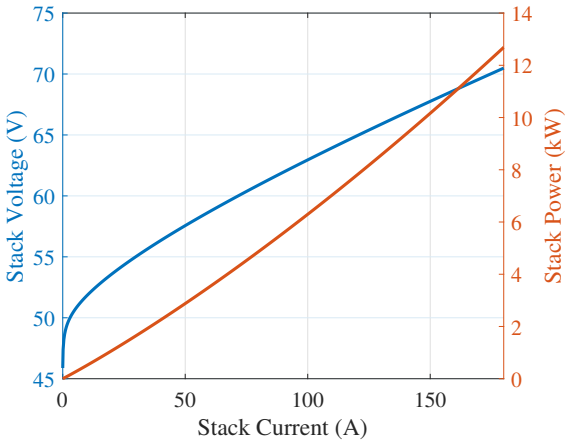

Figure 5.5: 10 kW AEL characteristics considered for the DAB-electrolyzer setup.

The AEL's electrical characteristics illustrated in Fig. 5.5 is represented as a variable resistor. The eHS schematic editor uses a lookup table, which defines the stack resistance reference based on the electrolyzer's I-V characteristics according to the stack current reference input. A PI current controller is implemented to adjust the phase angle that regulates the stack current.

5.4. RESULTS AND DISCUSSION

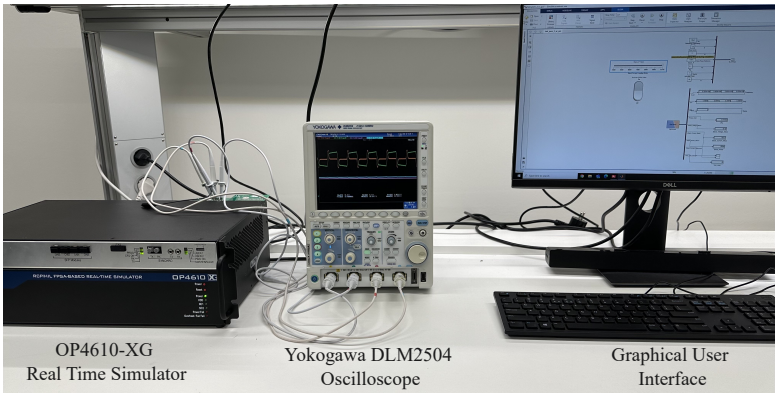

Figure 5.6: RTDT setup.

Table 5.3: Test Converter Specifications

Parameters	Value
P_o	10 kW
V_{DC}	1400 V
V_o	70 V
N_t	20:1
R_d	0.1 Ω
L	235 μH
f_{sw}	50 kHz
C_o	440 μF

Table 5.3 shows the test converter specifications for the RTDT model, and Fig. 5.6 depicts the RTDT setup. The AEL within the RTDT was operated from 40 % to 100 % of the rated power, with the model's stack current loading ranging from 0.4 pu to 1 pu. Fig. 5.7 displays the RTDT model outputs, such as stack voltage, stack current, inductor voltage, and inductor current, as monitored on the Yokogawa DLM2504 oscilloscope connected to the analog output card of the simulator. The oscilloscope readings, which ranged up to ±16 V, corresponded to the output voltage range of the simulator's analog out cards.

The inductor voltage, v_L (shown in orange), appears as a spike rather than a square pulse, with the pulse width corresponding to the applied phase shift, ϕ. This effect can be attributed to the analog card's sampling rate limitations. However, the inductor currents are accurately visualized by the RTDT. As the AEL is modeled as a variable resistor, the stack voltage and current on the oscilloscope show minimal to no ripple. Table 5.4 compares the measurements of the RTDT and the PLECS simulation model for the considered operating power cases.

Table 5.4: Comparison of RTDT model with PLECS model for 15°C stack temperature

Operating Power Case	Method	V_{stack} (V)	I_{stack} (A)	$i_{L(rms)}$ (A)	$i_{L(peak)}$ (A)	P_{stack}	% Error (P_{stack}) w. r. t. PLECS
10 kW	RTDT	67.38	147.5	7.52	9	9.93	0.7 %
	PLECS	67.55	148.46	8.1	9.2	10	
8 kW	RTDT	64.94	122.38	6.04	8.2	7.95	0.63 %
	PLECS	65.17	122.71	6.54	8.37	8	
6 kW	RTDT	62.5	96	4.72	7.4	6	0%
	PLECS	62.53	95.92	5.16	7.73	6	
4 kW	RTDT	59.5	67.63	3.78	7	4.02	-0.5%
	PLECS	59.51	67.2	4.14	7.33	4	

It was observed that the measured values of V_{stack}, I_{stack}, and P_{stack} are matching well with the simulation results with an error of less than 1 %. However, a slight variation was seen in the $i_{L(rms)}$ than the $i_{L(peak)}$ obtained from RTDT and simulation. The limit in the analog card sampling rate can justify this. While the analog card sampling rate did not affect the peak values of the inductor voltage, it did impact the RMS value since it is calculated over the switching period. As a result, this impact was reflected within the transformer currents. The RTDT measurements of stack voltage and current, reported in Table 5.4, were superimposed on the I-V characteristics of the electrolyzer operating at a temperature of T_c = 15°C.

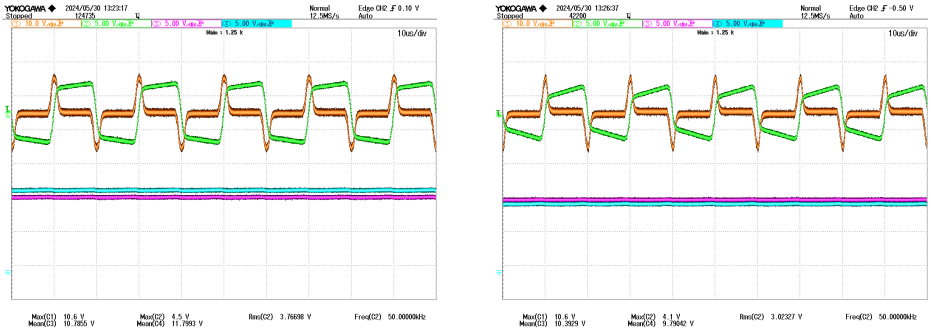

(a) $P_o = 10$ kW (b) $P_o = 8$ kW

(c) $P_o = 6$ kW (d) $P_o = 4$ kW

Figure 5.7: Response of the closed loop RTDT of the DAB converter integrated with a 10 kW AEL showcasing the inductor voltage (orange), the inductor current (green), stack voltage (purple), and stack current (cyan).

To showcase the operation of RTDT during the variation in stack temperature, two additional characteristics were considered for $T_c = 35°C$, and $T_c = 55°C$, respectively. Fig. 5.8 showcases this superimposition and demonstrates that the PI current controller effectively tracks the reference stack current set-point, allowing the RTDT to operate along the electrical characteristics of the AEL and during the variation in stack temperature.

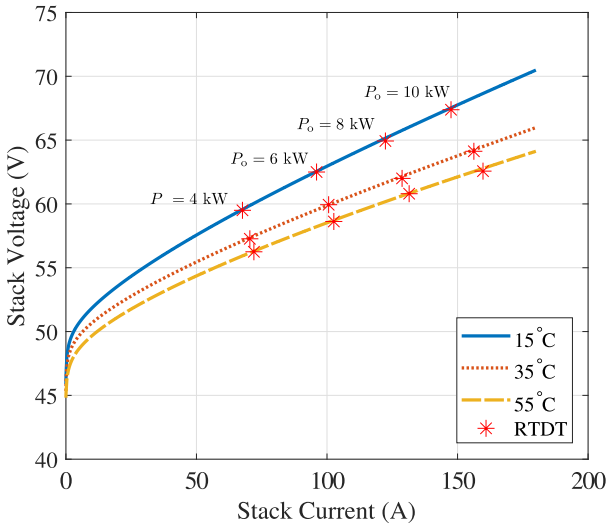

Figure 5.8: Comparison of RTDT response with the electrolyzer I-V characteristics for variation in stack temperature

5.5. CONCLUSIONS

This chapter presents the implementation of a 10 kW RTDT setup for a DAB-electrolyzer system operating in closed-loop current control. The real-time simulation architecture was explained in detail. This was followed by converting the Simulink model of the DAB-electrolyzer system to a hybrid Simulink-based RT-Lab model with a detailed explanation of its subsystems, SC_GUI, and SM_COMPUTE. The operation of the RTDT model was experimentally validated at four different power levels, considering stack temperature variations.

6

CONCLUSIONS AND FUTURE WORK

6.1. CONCLUDING REMARKS

1. *How do electrolyzer parameters imapact its electrical behavior? What preliminary implications do these parameters have on the design of a DAB converter?*

   Electrolyzers exhibit varying behavior under different operating conditions such as temperature and pressure, which alter their I-V characteristics. While electrical models of electrolyzers are well established, the implications of these variations for the design of the power electronics that interface with them remain insufficiently explored. In particular, the influence of operating conditions on converter ratings, efficiency, component sizing, and overall design has not been thoroughly addressed in the literature. Chapter 2 seeks to bridge this gap, focusing on DAB converters.

   Using a validated electrical model of an AEL, the study first confirmed that the electrolyzer's electrical characteristics are inherently nonlinear. Four key parameters—stack temperature, molar concentration, electrode surface area, and activation current—were then investigated to determine their influence on the electrical behavior. The analysis revealed that molar concentration had minimal impact on the electrical characteristics, whereas stack temperature, activation current, and electrode surface area significantly affected them. These variations were subsequently linked to DAB converter design, providing preliminary insights into their implications for converter operation.

   In summary, stack temperature, activation current, and electrode surface area were found to have a notable influence on DAB converter design, particularly in shaping HF transformer specifications and the current ratings of semiconductor switches. Although molar concentration had little short-term impact, it

may affect converter performance over long-term operation through corrosion-related changes in electrolyzer impedance. The long-term impact of molar concentration on the electrolyzer impedance requires access to a physical system which is beyond the scope of this thesis.

2. *How can GAM of DAB converter be simplified to achieve accurate transformer current reconstruction with minimal mathematical complexity?*

   Mathematical modeling has always been a cornerstone of power electronics design. It is an essential tool for understanding, analyzing, designing, and defining control objectives for power electronic systems. The DAB topology is a multi-stage DC-DC converter and, as such, includes an intermediate HF AC stage between the H-HV and H-LV ports. The small-ripple approximation—a conventional assumption used in modeling DC-DC converters to neglect higher-order harmonics—does not hold true for DAB converters because of this intermediate stage. In this context, the GAM technique addresses this limitation by accounting for the contribution of each harmonic of the fundamental frequency. However, despite this capability, previous studies have generally restricted modeling to the fundamental frequency only. While this simplifies the procedure, it leads to an inaccurate representation of the transformer current. Moreover, the effect of the turns ratio, N_t, was often ignored to reduce complexity, limiting practical relevance. In addition, many existing modeling approaches lack clearly defined steps or rely on multiple mathematical transformations, making them difficult to follow.

   Chapter 3 overcomes these shortcomings by presenting a high-accuracy GAM model of the DAB converter. A clear, step-by-step method is outlined to derive the model. Unlike traditional approaches, this work incorporates the effect of N_t. Generalized expressions are provided to construct a GAM model that includes the first M odd harmonics, allowing analysis beyond the fundamental frequency. This approach uses only Fourier Series and Complex Fourier Series techniques, limiting the amount of mathematical transformations.

   In conclusion, the proposed modeling technique accurately reconstructs transformer currents and has been validated against both offline and real-time simulations. The results confirm that limiting the analysis to the fundamental frequency produces incorrect transformer current reconstruction. Furthermore, the accuracy of the proposed model improves significantly as M increases.

3. *How do different state-of-the-art modulation strategies affect the performance of the DAB converter during electrolysis? How can the operation of DAB converter be optimized for electrolysis?*

   Chapter 3 focused not only on improving an existing modeling approach but also on the most critical component of the DAB converter—the HF transformer current. Maintaining the transformer current within permissible limits and with the appropriate waveform is essential for achieving efficient power transfer during electrolysis.

   Chapter 4 established the interaction between the DAB converter and the electrolyzer. State-of-the-art modulation schemes were investigated for the DAB converter with a focus on electrolysis. Due to their nonlinear, low-voltage, and high-current characteristics, electrolyzers present distinct challenges compared to conventional loads. A comparative analysis of SPS, DPS, and TPS modulation schemes was conducted using peak primary transformer current as the key evaluation metric at three power levels: 1 kW, 10 kW, and 100 kW. To accomplish this, a peak current optimization method was developed based on MATLAB's `fmincon` function to determine optimal phase-shift ratios for DPS and TPS schemes. This study demonstrated that electrolyzers behave fundamentally differently from CV loads under similar operating conditions, underscoring the importance of tailored modulation strategies for electrolysis.

   Building on this optimization framework, optimized operating trajectories for the DAB converter were identified for each power level. The analysis revealed that while SPS remained the most effective strategy for low-power electrolyzers, it became suboptimal at medium and high power levels due to increased circulating currents and reactive power—issues that can be significantly mitigated using DPS and TPS schemes. The proposed optimization framework was validated experimentally for the 1 kW electrolyzer and through simulations for 10 kW and 100 kW systems. The optimized trajectories achieved peak current reductions of up to 15.75% at 100 W for the 1 kW system, 42.71% at 1 kW for the 10 kW system, and 60% at 10 kW for the 100 kW system compared to conventional SPS operation.

   In conclusion, the operation of the DAB converter during electrolysis can be significantly enhanced by segmenting the electrolyzer's I-V characteristics into multiple regions and selecting the optimal modulation scheme for each that results in minimum peak current. This approach not only allow higher stack temperatures that can improve the hydrogen yield of the electrolyzer but, at the same time it avoids compromising the DAB converter's efficiency.

4. *How can DAB-electrolyzer system, be implemented and evaluated using a real-time digital twin?*

   Testing power electronics for electrolyzers has always been challenging due to the inherent risks associated with hydrogen production. Hydrogen gas is highly flammable, and any fault in the power electronics converter to which the electrolyzer is connected can compromise safety and create hazardous conditions. Furthermore, access to electrolyzers is often restricted in research institutions because of strict regulations and limited laboratory space. An effective alternative for evaluating converter designs is to implement the system using a RTDT. As noted in the literature review in Chapter 1, only one study has implemented such a setup for a single-stage PEC, indicating limited research in this area. Additionally, as shown in Table 1.4, most DT implementations for PEC involve only a single conversion stage, with no reported studies addressing multi-stage topologies.

   Chapter 5 addresses this gap by presenting an RTDT implementation for a DAB–electrolyzer system operating under closed-loop current control on an OP-4610XG real-time simulator. RTDT models differ significantly from standard offline simulation models. To bridge this gap, detailed steps were developed to convert an offline simulation into an RTDT-compatible model. With reference to Chapters 3 and 4, this work places particular emphasis on investigating transformer currents in the context of electrolysis. Consequently, the RTDT model was implemented using the eHS toolbox, which is particularly suited for real-time visualization of transformer currents.

   Validation of the RTDT showed an error of less than ±1% between the stack power obtained from offline PLECS simulations and the RTDT results. While peak currents were closely matched, RMS currents showed noticeable differences. In addition, the inductor voltage exhibited waveform distortion, attributed to hardware limitations in the simulator's sampling capabilities. The RTDT model was further validated against offline PLECS simulations under varying stack temperatures, demonstrating effective closed-loop control in tracking the required reference signals.

   In conclusion, the presented RTDT setup provides a valuable platform for evaluating power electronic converters for electrolysis, especially for researchers without direct access to electrolyzers. However, its applicability depends heavily on the chosen converter topology and the hardware capabilities of the real-time simulator. Limitations in simulator specifications can constrain both the scope and fidelity of the investigation. This was evident in this work, where the OP-4610XG served as an entry-level simulator.

6.2. FUTURE WORK

1. **Physical electrolyzer setups**
   This work relied on electrolyzer characteristics derived partly from a mathematical model and partly from experimentally measured parameters obtained from the literature (Chapter 2). These characteristics were emulated using a programmable DC power supply during the experimental phase (Chapter 4). Due to the safety concerns associated with hydrogen gas, operating a physical electrolyzer in a laboratory environment poses significant challenges. Consequently, this thesis focused exclusively on the steady-state operation of electrolyzers and their static characteristics. As discussed in Chapter 2, the electrical behavior of electrolyzers is also influenced by thermodynamic and electrochemical processes that are inherently time-dependent. These dynamic effects could not be captured in the present study. Future research should incorporate experimental validation using a physical electrolyzer setup to account for such time-dependent phenomena and to provide a more comprehensive understanding of electrolyzer-converter interactions.

2. **Stability analysis of DAB converter during electrolysis**
   As mentioned earlier, this work was conducted using the static characteristics of electrolyzers. However, dynamic behavior during startup or transient operating conditions may significantly impact the performance and stability of the DAB converter. This aspect was beyond the scope of the present research. Future studies should investigate the stability of the DAB converter under dynamic electrolyzer conditions, including startup, shutdown, and varying operating states, to ensure reliable and safe system operation.

3. **Soft-switching analysis of DAB converter during electrolysis**
   In Chapter 4, a comprehensive analysis and comparison of state-of-the-art modulation strategies for the DAB converter were carried out in the context of electrolysis. The proposed peak current optimization scheme, however, did not consider soft-switching constraints, as the primary objective was to establish a foundational framework for future research. A valuable extension of this work would be to incorporate soft-switching requirements into the optimization process. This would enable the development of a more sophisticated optimization scheme that minimizes peak current while simultaneously ensuring soft-switching operation, thereby improving converter efficiency and reducing switching losses.

Acknowledgements

I still remember the day I first set foot in this country on 14 August 2019. My initial goal was simple: to complete the M.Sc. programme and secure a job. Two years later, during my M.Sc. graduation ceremony, I was unexpectedly offered the opportunity to pursue a Ph.D.—an opportunity I accepted without hesitation. Looking back, I can say with absolute confidence that it was the right decision. My journey at TU Delft as a Ph.D. candidate was not without obstacles, but every challenge taught me valuable lessons and shaped me into the person I am today. This journey, however, was not one I could have traversed alone.

First and foremost, I express my heartfelt gratitude to the Almighty, Shri Swami Samarth. Without His blessings, I would not have reached this milestone. I am deeply indebted to my family, especially my parents, for their unconditional love, patience, and encouragement. They have been my constant companions, offering wisdom and support whenever I faltered.

I extend my sincere thanks to my supervisory team at TU Delft. To my promoter, Prof. Pavol Bauer, thank you for granting me the opportunity to pursue a Ph.D. and for your openness to my ideas and your steady guidance throughout this journey. Thiago, thank you for initiating my Ph.D. journey and for your mentorship during the first six months. Having been supervised by you during my M.Sc. thesis as well, I have benefited greatly from your knowledge of power electronics and your approachable nature. Aditya, thank you for supervising me for one and a half years. I tend to become emotionally invested in my work, and your critical—sometimes over-critical—feedback during our weekly meetings helped me develop resilience and taught me to evaluate my work with greater objectivity, an invaluable lesson for me as a researcher. Hani, it was a privilege to be supervised by you during the last two years of my Ph.D. I learned a great deal from your rigorous approach to research as well as your philosophical outlook on scientific inquiry. While we occasionally disagreed, our constructive discussions always led to mutual understanding. I also cherish our many conversations in the coffee room. Thank you for being not only a supervisor but also a friend.

I am grateful to my office mates for their companionship and support. Gautam, you have been an integral part of my Ph.D. journey—not only as a co-author in my publications but also as a close colleague. Yang and Lyu, your dedication during the final stages of your own Ph.D. journeys was a great source of motivation for me. Qobad and Heshi, although our time together was brief, I enjoyed sharing the office with you and wish you success in your future endeavours.

Anand, our friendship dates back to the early days of the M.Sc. programme. You have been a constant source of support—whether brainstorming ideas, debugging code, or refining approaches to complex problems. I am truly grateful for your help and wish you the very best as you continue your own Ph.D. journey.

I have always been somewhat introverted, which sometimes made it difficult to connect with others. Thanks to my colleagues and friends in the DCE&S research group, I was able to step out of my shell. Francesca, Ibrahim, Wiljan, Miad, Junjie, and Yang, thank you for your delightful company during PEMC 2022 in Bucharest and Brașov—an unforgettable trip filled with laughter. Reza, Faezeh, Gangwei, Dario, Alvaro, and Zhengzhao, I equally cherish the good times we shared during IECON 2023 in Singapore. To Siddhesh and Dhanashree, my Indian Marathi colleagues, thank you for the camaraderie and familiarity that made Delft feel closer to home. A special thanks to Sharmila, the true backbone of the DCE&S group, whose patience, efficiency, and unwavering support in handling travel, financial, and administrative matters made our lives significantly easier.

I also appreciate the invaluable support of our lab technicians—Joris, for assisting with the real-time simulator setups, and Hitesh and Mladen, for your patience and guidance in PCB design during my experiments. My thanks also go to Sachin for generously sharing his knowledge of PCB design and LaTeX.

Calvin and Joel, I have thoroughly enjoyed our conversations—whether over legendary rice bowls at lunch or ramen on weekends—and I look forward to many more. To Taybeh, Shadi, and Sourabh, it has been inspiring to watch you initiate research in such a promising domain. I wish you strength and success in your Ph.D. journeys.

Finally, to everyone else whose paths crossed mine during these years—thank you for your kindness and companionship.

A

Propositions

Propositions

accompanying the dissertation

DUAL ACTIVE BRIDGE CONVERTERS FOR ELECTROLYZERS

AN APPLICATION ORIENTED PERSPECTIVE

by

Rohan Shailesh DESHMUKH

1. Fundamental research is not only an indispensable first step but can also be the final step towards novelty. *(this thesis)*
2. The pace of power electronics research for hydrogen production is dictated less by innovation and more by the data silence of electrolyzer manufacturers. *(this thesis)*
3. The true strength of mathematical modeling lies in its clarity, not in its complexity. *(this thesis)*
4. Converter-level studies deserve equal footing with system-level investigations. *(this thesis)*
5. It is laughable to think open-access journals are second-rate.
6. Obsessed with prestige and rankings, academia risks a zombie apocalypse of its own - researchers reduced to lifeless paper factories wandering in search of impact factors.
7. Good research runs on patience, not on deadlines.
8. A Ph.D. program should never be reduced to a business deal between student and university.
9. Reviewer 2 exists only to test the limits of human patience.
10. Coffee is not a beverage but a vital reagent in any Ph.D. experiment.
11. If flights traveling from east to west give us jet lag then, flights from west to east should give us jet lead.

These propositions are regarded as opposable and defendable, and have been approved as such by the promotor Prof. dr. ir. P. Bauer and copromotor dr. H.Vahedi.

BIBLIOGRAPHY

[1] A. M. Oliveira, R. R. Beswick, and Y. Yan, "A green hydrogen economy for a renewable energy society", *Current Opinion in Chemical Engineering*, vol. 33, p. 100 701, 2021, ISSN: 2211-3398. DOI: https://doi.org/10.1016/j.coche.2021.100701.

[2] M. van Economische Zaken en Klimaat, *Klimaatakkoord*, Aug. 2019.

[3] E. Commission, *Eu climate strategies and targets*, 2020.

[4] U. Nations, *Paris agreement*, 2016.

[5] S. A. Bonab and M. Yazdani-Asrami, "Artificial intelligence-based model to predict the heat transfer coefficient in flow boiling of liquid hydrogen as fuel and cryogenic coolant in future hydrogen-powered cryo-electric aviation", *Fuel*, vol. 381, p. 133 323, 2025.

[6] S. A. Bonab and M. Yazdani-Asrami, "Investigation on the heat transfer estimation of subcooled liquid hydrogen for transportation applications using intelligent technique", *International Journal of Hydrogen Energy*, vol. 84, pp. 468–479, 2024.

[7] Linde, *Electrolysis for green hydrogen production towards a cleaner, greener future*, https://www.linde.com/clean-energy/our-h2-technology/electrolysis-for-green-hydrogen-production, Accessed: 2024-04-04, 2024.

[8] S. A. Bonab, T. Waite, W. Song, D. Flynn, and M. Yazdani-Asrami, "Machine learning-powered performance monitoring of proton exchange membrane water electrolyzers for enhancing green hydrogen production as a sustainable fuel for aviation industry", *Energy Reports*, vol. 12, pp. 2270–2282, 2024.

[9] G. H. Coalition, *Green hydrogen guide book*, https://www.ghcoalition.org/guidebook, Accessed: 2024-10-21, 2022.

[10] I. E. Agency, "Global hydrogen review", 2022.

[11] M. Al-Breiki and Y. Bicer, "Investigating the technical feasibility of various energy carriers for alternative and sustainable overseas energy transport scenarios", *Energy Conversion and Management*, vol. 209, p. 112 652, 2020, ISSN: 0196-8904. DOI: https://doi.org/10.1016/j.enconman.2020.112652.

[12] R. Tarkowski, "Underground hydrogen storage: Characteristics and prospects", *Renewable and Sustainable Energy Reviews*, vol. 105, pp. 86–94, 2019, ISSN: 1364-0321. DOI: https://doi.org/10.1016/j.rser.2019.01.051.

[13] T. N. Hydrohub Innovation Program Amersfoort, *Gigawatt green hydrogen plant: State-of-the-art design and total installed capital costs*, Accessed: 2025-5-1, 2020.

[14] L. Nuttall, A. Fickett, and W. Titterington, "Hydrogen generation by solid polymer electrolyte water electrolysis", *Hydrogen Energy: Part A*, pp. 441–455, 1975.

[15] I. R. E. A. (IRENA), *Green hydrogen supply: A guide to policy making*, Accessed: 2025-5-1, 2021.

[16] S. Qazi, A. Abdelhakim, T. B. Soeiro, Q. Xu, S. Bosga, and F. Canales, "Electrified hydrogen systems: An overview", *IEEE Industrial Electronics Magazine*, 2025.

[17] A. Trattner, M. Höglinger, M.-G. Macherhammer, and M. Sartory, "Renewable hydrogen: Modular concepts from production over storage to the consumer", *Chemie Ingenieur Technik*, vol. 93, no. 4, pp. 706–716, 2021.

[18] P. Kim-Lohsoontorn et al., "Durability and degradation issues in solid oxide electrolysis cells", in *High Temperature Electrolysis*, Springer, 2023, pp. 277–312.

[19] J. Koponen, V. Ruuskanen, A. Kosonen, M. Niemelä, and J. Ahola, "Effect of converter topology on the specific energy consumption of alkaline water electrolyzers", *IEEE Transactions on Power Electronics*, vol. 34, no. 7, pp. 6171–6182, 2018.

[20] M. Chen, S.-F. Chou, F. Blaabjerg, and P. Davari, "Overview of power electronic converter topologies enabling large-scale hydrogen production via water electrolysis", *Applied Sciences*, vol. 12, no. 4, p. 1906, 2022.

[21] A. Siebert, A. Troedson, and S. Ebner, "Ac to dc power conversion now and in the future", *IEEE transactions on industry applications*, vol. 38, no. 4, pp. 934–940, 2002.

[22] J. Solanki, N. Fröhleke, and J. Böcker, "Implementation of hybrid filter for 12-pulse thyristor rectifier supplying high-current variable-voltage dc load", *IEEE Transactions on Industrial Electronics*, vol. 62, no. 8, pp. 4691–4701, 2015.

[23] J. R. Rodríguez et al., "Large current rectifiers: State of the art and future trends", *IEEE Transactions on Industrial Electronics*, vol. 52, no. 3, pp. 738–746, 2005.

[24] J. Solanki, N. Fröhleke, J. Böcker, A. Averberg, and P. Wallmeier, "High-current variable-voltage rectifiers: State of the art topologies", *IET Power Electronics*, vol. 8, no. 6, pp. 1068–1080, 2015.

[25] Á. Hernández-Gómez, V. Ramirez, D. Guilbert, and B. Saldivar, "Cell voltage static-dynamic modeling of a pem electrolyzer based on adaptive parameters: Development and experimental validation", *Renewable Energy*, vol. 163, pp. 1508–1522, 2021.

[26] Z. Dobó and Á. B. Palotás, "Impact of the current fluctuation on the efficiency of alkaline water electrolysis", *International Journal of Hydrogen Energy*, vol. 42, no. 9, pp. 5649–5656, 2017.

[27] D. Guilbert, S. M. Collura, and A. Scipioni, “Dc/dc converter topologies for electrolyzers: State-of-the-art and remaining key issues”, *Int. Journal of Hydrogen Energy*, vol. 42, no. 38, pp. 23 966–23 985, 2017.

[28] M. B. El Kattel et al., “Overview of main electrolyzer technologies and power electronic converter topologies for enabling hydrogen production through water electrolysis”, *International Journal of Circuit Theory and Applications*, 2024.

[29] J. Jiménez-Giménez, A. Lázaro, Á. Mayor, J. López-López, and A. Barrado, “New bidirectional isolated three-phase dc-dc converter with parallel-to-serial configuration for energy applications”, *IEEE Open Journal of the Industrial Electronics Society*, 2025.

[30] X. Li, N. Li, W. Xue, W. Mao, S. Qiu, and X. Wu, “Lcc-resonant-type current-fed-out three-port dc–dc converter for pv electrolytic hydrogen production integrated with energy storage”, *IEEE Transactions on Industrial Electronics*, 2024.

[31] X. Guo, S. Zhang, F. Ding, J. Zhu, and H. Bai, “A novel dc–dc converter for electrolyzer with low ripple and high step down”, *IEEE Transactions on Industrial Electronics*, vol. 71, no. 10, pp. 12 476–12 486, 2024.

[32] S. A. Gorji, “Reconfigurable quadratic converters for electrolyzers utilized in dc microgrids”, *IEEE Access*, vol. 10, pp. 109 677–109 687, 2022.

[33] Y. Xiao, Z. Zhang, M. A. Andersen, and B. E. Thomsen, “Partial parallel dual active bridge converter with variable voltage gain for soec/sofc system”, in *ganjavi2022design2019 IEEE Applied Power Electronics Conference and Exposition (APEC)*, IEEE, 2019, pp. 1641–1646.

[34] X. Lin, K. Sun, J. Lin, Z. Zhang, and W. Kong, “A multi-port bidirectional power conversion system for reversible solid oxide fuel cell applications”, in *2018 International Power Electronics Conference (IPEC-Niigata 2018-ECCE Asia)*, IEEE, 2018, pp. 3460–3465.

[35] R. Pittini, Z. Zhang, and M. A. Andersen, “Isolated full bridge boost dc-dc converter designed for bidirectional operation of fuel cells/electrolyzer cells in grid-tie applications”, in *2013 15th European Conference on Power Electronics and Applications (EPE)*, IEEE, 2013, pp. 1–10.

[36] L. Sánchez, D. Reigosa, A. Bilbao, I. Peña-Gonzalez, and F. Briz, “Comparative analysis of power converter topologies for hydrogen electrolyzers”, *IEEE Journal of Emerging and Selected Topics in Power Electronics*, 2024.

[37] M. E. Şahin, H. İ. Okumuş, and M. T. Aydemir, “Implementation of an electrolysis system with dc/dc synchronous buck converter”, *International Journal of hydrogen energy*, vol. 39, no. 13, pp. 6802–6812, 2014.

[38] A. Garrigós, J. Blanes, J. Carrasco, J. Lizán, R. Beneito, and J. Molina, “5 kw dc/dc converter for hydrogen generation from photovoltaic sources”, *International Journal of hydrogen energy*, vol. 35, no. 12, pp. 6123–6130, 2010.

[39] S. M. Collura et al., “Design and experimental validation of a high voltage ratio dc/dc converter for proton exchange membrane electrolyzer applications”, *International Journal of Hydrogen Energy*, vol. 44, no. 14, pp. 7059–7072, 2019.

[40] X. Guo, F. Ding, S. Zhang, Y. Teng, N. Diao, and V. Terzija, “Enhanced green hydrogen production using a novel converter with extremely low current ripple and high step-down ratio”, *Fuel*, vol. 398, p. 135 424, 2025.

[41] M. B. El Kattel, K. D. N. Cavalcante, P. P. Praça, D. S. Oliveira, L. H. S. C. Barreto, and F. L. M. Antunes, “High-efficiency multi-arm interleaved dc-dc converter featuring reduced magnetic components for high power density in water electrolysis applications”, *IEEE Journal of Emerging and Selected Topics in Power Electronics*, 2025.

[42] Á. Iribarren, E. L. Barrios, P. Sanchis, and A. Ursúa, “Modeling and optimal sizing of thyristor rectifiers for high-power hydrogen electrolyzers”, *IEEE Journal of Emerging and Selected Topics in Power Electronics*, 2025.

[43] M. C. Mira, Z. Zhang, and A. M. Andersen, “Analysis and comparison of dc/dc topologies in partial power processing configuration for energy storage systems”, in *2018 International Power Electronics Conference (IPEC-Niigata 2018-ECCE Asia)*, IEEE, 2018, pp. 1351–1357.

[44] S. Dahbi, R. Aboutni, A. Aziz, N. Benazzi, M. Elhafyani, and K. Kassmi, “Optimised hydrogen production by a photovoltaic-electrolysis system dc/dc converter and water flow controller”, *International Journal of Hydrogen Energy*, vol. 41, no. 45, pp. 20 858–20 866, 2016.

[45] D. Guilbert and G. Vitale, “Optimal hydrogen production from direct coupled variable speed wind generator with a stacked interleaved buck converter”, in *2019 IEEE International Conference on Environment and Electrical Engineering and 2019 IEEE Industrial and Commercial Power Systems Europe (EEEIC/I&CPS Europe)*, IEEE, 2019, pp. 1–6.

[46] C. Pascalau, T. B. Soeiro, N. H. van der Blij, and P. Bauer, “Electrical energy conversion for low temperature electrolysis-challenges and future trends”, in *2021 IEEE 19th International Power Electronics and Motion Control Conference (PEMC)*, IEEE, 2021, pp. 349–356.

[47] A. Ganjavi, S. A. Gorji, A. Hakemi, A. Moradi, and D. Sera, “Design and implementation of an sic-based 48 v-380 v dual active bridge dc-dc converter for batteries employed in green hydrogen microgrids”, in *2022 IEEE 7th Southern Power Electronics Conference (SPEC)*, IEEE, 2022, pp. 1–6.

[48] T. Martin, B. Majmunović, V. I. Kumar, M. Ilic, and D. Maksimović, “Modular series-stacked bidirectional ac/dc architecture for 3-phase grid-tied applications”, in *2023 IEEE Applied Power Electronics Conference and Exposition (APEC)*, IEEE, 2023, pp. 984–988.

[49] N. Fritz, T. Sechel, P. Kowalewski, and R. W. De Doncker, "Optimizing current-fed, gan-based dc-dc converters for electrolysis applications", in *2023 11th International Conference on Power Electronics and ECCE Asia (ICPE 2023-ECCE Asia)*, IEEE, 2023, pp. 2843–2850.

[50] F. Pellitteri, N. Campagna, R. Inguanta, and R. Miceli, "Application of a multiphase interleaved dc-dc converter for power-to-hydrogen systems", in *2023 IEEE 17th International Conference on Compatibility, Power Electronics and Power Engineering (CPE-POWERENG)*, IEEE, 2023, pp. 1–6.

[51] M. Geske, H. S. Hildebrandt, K. Jalili, and C. Keller, "High-power converter systems for hydrogen production", in *2023 25th European Conference on Power Electronics and Applications (EPE'23 ECCE Europe)*, IEEE, 2023, pp. 1–10.

[52] A. Rospirski et al., "Enhanced three-phase interleaving phase-shifted full bridge converter with active clamp using ganfet for green hydrogen production", in *2023 IEEE 8th Southern Power Electronics Conference and 17th Brazilian Power Electronics Conference (SPEC/COBEP)*, IEEE, 2023, pp. 1–6.

[53] L. Palma, "Analysis and selection of step-down converter for pem electrolyzer applications", in *2024 International Symposium on Power Electronics, Electrical Drives, Automation and Motion (SPEEDAM)*, IEEE, 2024, pp. 1160–1165.

[54] C. Matus, H. Young, B. Pavez, P. Burgos, C. Cifuentes, and C. Lazcano, "Integration of renewable sources with multiport converter to supply electrolyzers", in *2024 IEEE International Conference on Automation/XXVI Congress of the Chilean Association of Automatic Control (ICA-ACCA)*, IEEE, 2024, pp. 1–5.

[55] T. O. Olowu, A. Shigrekar, M. J. Casteel, N. Kang, J. L. Hartvigsen, and T. L. Westover, "Analysis of ac-dc converters for grid-tied high temperature steam electrolysis systems", in *2024 IEEE Energy Conversion Congress and Exposition (ECCE)*, IEEE, 2024, pp. 598–605.

[56] D. Pedro, R. E. Araújo, A. M. Elhawash, and J. A. P. Lopes, "Comparative analysis of classical ac/dc rectifiers for hydrogen electrolyzer applications", in *2024 IEEE 3rd Industrial Electronics Society Annual On-Line Conference (ONCON)*, IEEE, 2024, pp. 1–6.

[57] D. S. Gautam and A. K. Bhat, "A comparison of soft-switched dc-to-dc converters for electrolyzer application", *IEEE Transactions on power electronics*, vol. 28, no. 1, pp. 54–63, 2012.

[58] G. Oggier, G. O. Garcia, and A. R. Oliva, "Modulation strategy to operate the dual active bridge dc-dc converter under soft switching in the whole operating range", *IEEE Trans. Power Electron.*, vol. 26, no. 4, pp. 1228–1236, 2010.

[59] F. Krismer and J. W. Kolar, "Efficiency-optimized high-current dual active bridge converter for automotive applications", *IEEE Trans. Ind. Electron.*, vol. 59, no. 7, pp. 2745–2760, 2011.

[60] E. Amores, J. Rodríguez, and C. Carreras, "Influence of operation parameters in the modeling of alkaline water electrolyzers for hydrogen production", *International Journal of Hydrogen Energy*, vol. 39, no. 25, pp. 13 063–13 078, 2014.

[61] A. A. AlZahrani and I. Dincer, "Thermodynamic and electrochemical analyses of a solid oxide electrolyzer for hydrogen production", *International Journal of Hydrogen Energy*, vol. 42, no. 33, pp. 21 404–21 413, 2017.

[62] X. Shen, X. Zhang, T. T. Lie, and G. Li, "Mathematical modeling and simulation for external electrothermal characteristics of an alkaline water electrolyzer", *International Journal of Energy Research*, vol. 42, no. 12, pp. 3899–3914, 2018.

[63] A. S. Tijani, M. A. Ghani, A. A. Rahim, I. K. Muritala, and F. A. B. Mazlan, "Electrochemical characteristics of (pem) electrolyzer under influence of charge transfer coefficient", *international journal of hydrogen energy*, vol. 44, no. 50, pp. 27 177–27 189, 2019.

[64] Á. Hernández-Gómez, V. Ramirez, D. Guilbert, and B. Saldivar, "Development of an adaptive static-dynamic electrical model based on input electrical energy for pem water electrolysis", *International journal of hydrogen energy*, vol. 45, no. 38, pp. 18 817–18 830, 2020.

[65] C. V. Pham, D. Escalera-López, K. Mayrhofer, S. Cherevko, and S. Thiele, "Essentials of high performance water electrolyzers–from catalyst layer materials to electrode engineering", *Advanced energy materials*, vol. 11, no. 44, p. 2 101 998, 2021.

[66] K. Zhang et al., "Status and perspectives of key materials for pem electrolyzer", *Nano Res. Energy*, vol. 1, no. 3, e9120032, 2022.

[67] I. Firtina-Ertis, "Thermodynamic and electrochemical assessment of an alkaline electrolyzer (ae) at different operating parameters", *Journal of Environmental Chemical Engineering*, vol. 10, no. 2, p. 107 225, 2022.

[68] G. Sakas, A. Ibáñez-Rioja, V. Ruuskanen, A. Kosonen, J. Ahola, and O. Bergmann, "Dynamic energy and mass balance model for an industrial alkaline water electrolyzer plant process", *International Journal of Hydrogen Energy*, vol. 47, no. 7, pp. 4328–4345, 2022.

[69] K. Hu et al., "Comparative study of alkaline water electrolysis, proton exchange membrane water electrolysis and solid oxide electrolysis through multiphysics modeling", *Applied Energy*, vol. 312, p. 118 788, 2022.

[70] S. Bacha, I. Munteanu, A. I. Bratcu, et al., "Power electronic converters modeling and control", *Advanced textbooks in control and signal processing*, vol. 454, p. 454, 2014.

[71] H. Qin and J. W. Kimball, "Generalized average modeling of dual active bridge dc–dc converter", *IEEE Transactions on power electronics*, vol. 27, no. 4, pp. 2078–2084, 2011.

[72] J. A. Mueller and J. W. Kimball, “Generalized average modeling of dc subsystem in solid state transformers”, in *2017 IEEE Energy Conversion Congress and Exposition (ECCE)*, IEEE, 2017, pp. 1659–1666.

[73] J. A. Mueller and J. W. Kimball, “An improved generalized average model of dc–dc dual active bridge converters”, *IEEE Transactions on Power Electronics*, vol. 33, no. 11, pp. 9975–9988, 2018.

[74] S. Ghosh, D. Das, B. Singh, S. Janardhanan, and S. Mishra, “Frequency-domain modeling of dual-active-bridge converter based on harmonic balance approach”, *IEEE Journal of Emerging and Selected Topics in Industrial Electronics*, vol. 3, no. 1, pp. 166–176, 2021.

[75] O. M. Hebala, A. A. Aboushady, K. H. Ahmed, S. Burgess, and R. Prabhu, “Generalized small-signal modelling of dual active bridge dc/dc converter”, in *2018 7th International Conference on Renewable Energy Research and Applications (ICRERA)*, IEEE, 2018, pp. 914–919.

[76] J. A. Mueller and J. W. Kimball, “Modeling dual active bridge converters in dc distribution systems”, *IEEE Transactions on Power Electronics*, vol. 34, no. 6, pp. 5867–5879, 2018.

[77] M. Zhang, J. Tong, Z. Chen, and A. Q. Huang, “A unified numerical modeling method for dual active bridge type converter”, in *2023 IEEE Energy Conversion Congress and Exposition (ECCE)*, IEEE, 2023, pp. 3035–3041.

[78] Z. Xiao, W. Lei, G. Gao, H. Wang, and W. Mu, “Simplified discrete-time modeling for convenient stability prediction of dab converter in energy storage system”, *IEEE Transactions on Power Electronics*, 2024.

[79] J. Cronin, A. Wunderlich, and E. Santi, “Transconductance model of the dual active bridge converter under single and dual phase shift control”, in *2025 IEEE Applied Power Electronics Conference and Exposition (APEC)*, IEEE, 2025, pp. 2865–2870.

[80] B. Zhao, Q. Song, W. Liu, and Y. Xiao, “Next-generation multi-functional modular intelligent ups system for smart grid”, *IEEE Trans. Ind. Electron.*, vol. 60, no. 9, pp. 3602–3618, 2012.

[81] H. Wen, W. Xiao, and B. Su, “Nonactive power loss minimization in a bidirectional isolated dc–dc converter for distributed power systems”, *IEEE Trans. Ind. Electron.*, vol. 61, no. 12, pp. 6822–6831, 2014.

[82] B. Zhao, Q. Song, and W. Liu, “Experimental comparison of isolated bidirectional dc–dc converters based on all-si and all-sic power devices for next-generation power conversion application”, *IEEE Trans. Ind. Electron.*, vol. 61, no. 3, pp. 1389–1393, 2013.

[83] S. P. Engel, M. Stieneker, N. Soltau, S. Rabiee, H. Stagge, and R. W. De Doncker, “Comparison of the modular multilevel dc converter and the dual-active bridge converter for power conversion in hvdc and mvdc grids”, *IEEE Trans. Power Electron.*, vol. 30, no. 1, pp. 124–137, 2014.

[84] N. Hou and Y. W. Li, "A tunable power sharing control scheme for the output-series dab dc–dc system with independent or common input terminals", *IEEE Trans. Power Electron.*, vol. 34, no. 10, pp. 9386–9391, 2019.

[85] B. Zhao, Q. Song, J. Li, Y. Wang, and W. Liu, "High-frequency-link modulation methodology of dc–dc transformer based on modular multilevel converter for hvdc application: Comprehensive analysis and experimental verification", *IEEE Trans. Power Electron.*, vol. 32, no. 5, pp. 3413–3424, 2016.

[86] F. D. Freijedo, E. Rodriguez-Diaz, and D. Dujic, "Stable and passive high-power dual active bridge converters interfacing mvdc grids", *IEEE Trans. Ind. Electron.*, vol. 65, no. 12, pp. 9561–9570, 2018.

[87] P. Nayak, S. Mandal, Y. Gupta, A. Shukla, and S. Doolla, "Improving the efficiency of the dab converter of an on-board ev charger using different modulation techniques", in *2020 IEEE International Conference on Power Electronics, Drives and Energy Systems (PEDES)*, 2020, pp. 1–6. DOI: 10.1109/PEDES49360.2020.9379360.

[88] J. Everts, F. Krismer, J. Van den Keybus, J. Driesen, and J. W. Kolar, "Charge-based zvs soft switching analysis of a single-stage dual active bridge ac-dc converter", in *2013 IEEE Energy Conver. Congress and Expo.*, IEEE, 2013, pp. 4820–4829.

[89] J. Everts, F. Krismer, J. Van den Keybus, J. Driesen, and J. W. Kolar, "Optimal zvs modulation of single-phase single-stage bidirectional dab ac–dc converters", *IEEE Trans. Power Electron.*, vol. 29, no. 8, pp. 3954–3970, 2013.

[90] L. Xue, Z. Shen, D. Boroyevich, P. Mattavelli, and D. Diaz, "Dual active bridge-based battery charger for plug-in hybrid electric vehicle with charging current containing low frequency ripple", *IEEE Trans. Power Electron.*, vol. 30, no. 12, pp. 7299–7307, 2015.

[91] A. V. Mirtchev and E. C. Tatakis, "Design methodology based on dual control of a resonant dual active bridge converter for electric vehicle battery charging", *IEEE Transactions on Vehicular Technology*, vol. 71, no. 3, pp. 2691–2705, 2022. DOI: 10.1109/TVT.2022.3142681.

[92] D. Chen, J. Deng, W. Wang, and Z. Wang, "A dual-transformer-based hybrid dual active bridge converter for plug-in electric vehicle charging to cope with wide load voltages", *IEEE Transactions on Industrial Electronics*, vol. 70, no. 2, pp. 1444–1454, 2023. DOI: 10.1109/TIE.2022.3158013.

[93] Y. Xuan, X. Yang, W. Chen, T. Liu, and X. Hao, "A three-level dual-active-bridge converter with blocking capacitors for bidirectional electric vehicle charger", *IEEE Access*, vol. 7, pp. 173 838–173 847, 2019. DOI: 10.1109/ACCESS.2019.2957022.

[94] H. V. Nguyen, D.-D. To, and D.-C. Lee, "Onboard battery chargers for plug-in electric vehicles with dual functional circuit for low-voltage battery charging and active power decoupling", *IEEE Access*, vol. 6, pp. 70 212–70 222, 2018. DOI: 10.1109/ACCESS.2018.2876645.

[95] P. He and A. Khaligh, "Comprehensive analyses and comparison of 1 kw isolated dc–dc converters for bidirectional ev charging systems", *IEEE Transactions on Transportation Electrification*, vol. 3, no. 1, pp. 147–156, 2017. DOI: 10.1109/TTE.2016.2630927.

[96] J. Shi, W. Gou, H. Yuan, T. Zhao, and A. Q. Huang, "Research on voltage and power balance control for cascaded modular solid-state transformer", *IEEE Trans. Power Electron.*, vol. 26, no. 4, pp. 1154–1166, 2011.

[97] T. Zhao, G. Wang, S. Bhattacharya, and A. Q. Huang, "Voltage and power balance control for a cascaded h-bridge converter-based solid-state transformer", *IEEE Trans. Power Electron.*, vol. 28, no. 4, pp. 1523–1532, 2012.

[98] X. She, A. Q. Huang, and X. Ni, "Current sensorless power balance strategy for dc/dc converters in a cascaded multilevel converter based solid state transformer", *IEEE Trans. Power Electron.*, vol. 29, no. 1, pp. 17–22, 2013.

[99] S. Falcones, R. Ayyanar, and X. Mao, "A dc–dc multiport-converter-based solid-state transformer integrating distributed generation and storage", *IEEE Transactions on Power Electronics*, vol. 28, no. 5, pp. 2192–2203, 2013. DOI: 10.1109/TPEL.2012.2215965.

[100] R. Naayagi, A. Forsyth, and R. Shuttleworth, "Bidirectional control of a dual active bridge dc–dc converter for aerospace applications", *IET Power Electron.*, vol. 5, no. 7, pp. 1104–1118, 2012.

[101] G. Buticchi, D. Barater, L. F. Costa, and M. Liserre, "A pv-inspired low-common-mode dual-active-bridge converter for aerospace applications", *IEEE Trans. Power Electron.*, vol. 33, no. 12, pp. 10 467–10 477, 2018.

[102] N. M. L. Tan, T. Abe, and H. Akagi, "Design and performance of a bidirectional isolated dc–dc converter for a battery energy storage system", *IEEE Trans. Power Electron.*, vol. 27, no. 3, pp. 1237–1248, 2011.

[103] F. Xue, R. Yu, and A. Q. Huang, "A 98.3% efficient gan isolated bidirectional dc–dc converter for dc microgrid energy storage system applications", *IEEE Trans. Ind. Electron.*, vol. 64, no. 11, pp. 9094–9103, 2017.

[104] V. Karthikeyan and R. Gupta, "Multiple-input configuration of isolated bidirectional dc–dc converter for power flow control in combinational battery storage", *IEEE Trans. Ind. Inform.*, vol. 14, no. 1, pp. 2–11, 2017.

[105] D.-D. Nguyen, K. Yuktta, A. Katou, and S. Yoshida, "A comparison study of modulation methods for three-phase dual-active-bridge converters in battery charging applications", in *2021 IEEE 12th Energy Conversion Congress & Exposition - Asia (ECCE-Asia)*, 2021, pp. 1033–1038. DOI: 10.1109/ECCE-Asia49820.2021.9479112.

[106] R. S. Deshmukh, A. Shekhar, and P. Bauer, "Adaptive modularity for power electronics based electrolysis systems for green hydrogen", in *2022 IEEE 20th Int. Power Electron. Motion Control Conf. (PEMC)*, IEEE, 2022, pp. 508–515.

[107] R. S. Deshmukh, G. Rituraj, N. Lock, H. Vahedi, A. Shekhar, and P. Bauer, "Implementation of real-time digital twin of dual active bridge converter in electrolyzer applications", in *IECON 2023-49th Annu. Conf. IEEE Indus. Electron. Soc.*, IEEE, 2023, pp. 1–6.

[108] C. Wu, Z. Cui, Q. Xia, J. Yue, and F. Lyu, "An overview of digital twin technology for power electronics: State-of-the-art and future trends", *IEEE Transactions on Power Electronics*, 2025.

[109] E. Glaessgen and D. Stargel, "The digital twin paradigm for future nasa and us air force vehicles", in *53rd AIAA/ASME/ASCE/AHS/ASC structures, structural dynamics and materials conf. 20th AIAA/ASME/AHS adaptive structures conf. 14th AIAA*, 2012, p. 1818.

[110] M. Zhou and J. Yan, "A new solution architecture for online power system analysis", *CSEE J. Power and Energy Systems*, vol. 4, no. 2, pp. 250–256, 2018.

[111] P. Moutis and O. Alizadeh-Mousavi, "Digital twin of distribution power transformer for real-time monitoring of medium voltage from low voltage measurements", *IEEE Trans. Power Deliver.*, vol. 36, no. 4, pp. 1952–1963, 2020.

[112] F. Arraño-Vargas and G. Konstantinou, "Modular design and real-time simulators toward power system digital twins implementation", *IEEE Transactions on Industrial Informatics*, vol. 19, no. 1, pp. 52–61, 2022.

[113] H. Cao, D. Zhang, and S. Yi, "Real-time machine learning-based fault detection, classification, and locating in large scale solar energy-based systems: Digital twin simulation", *Solar Energy*, vol. 251, pp. 77–85, 2023.

[114] S. Venkatesan, K. Manickavasagam, N. Tengenkai, and N. Vijayalakshmi, "Health monitoring and prognosis of electric vehicle motor using intelligent-digital twin", *IET Electric Power Appl.*, vol. 13, no. 9, pp. 1328–1335, 2019.

[115] L. Herrera, C. Li, X. Yao, and J. Wang, "Fpga-based detailed real-time simulation of power converters and electric machines for ev hil applications", *IEEE transactions on industry applications*, vol. 51, no. 2, pp. 1702–1712, 2014.

[116] C. Lyu and V. Dinavahi, "Multidomain device-level fuel-cell modeling and real-time hardware emulation for marine research vessel power system", *IEEE Transactions on Transportation Electrification*, vol. 10, no. 1, pp. 1715–1728, 2023.

[117] K. Jessen, M. Soltani, A. Hajizadeh, E. Schaltz, S. H. Jensen, and L. Török, "Real-time emulation of reversible solid oxide electrolyzer's electrical behavior for rapid-prototyping of power electronics", *IEEE Access*, 2024.

[118] C. Liu, H. Bai, S. Zhuo, X. Zhang, R. Ma, and F. Gao, "Real-time simulation of power electronic systems based on predictive behavior", *IEEE Transactions on Industrial Electronics*, vol. 67, no. 9, pp. 8044–8053, 2019.

[119] H. F. Blanchette, T. Ould-Bachir, and J. P. David, "A state-space modeling approach for the fpga-based real-time simulation of high switching frequency power converters", *IEEE Transactions on Industrial Electronics*, vol. 59, no. 12, pp. 4555–4567, 2011.

[120] G. Di Nezio, S. D. L. Diz, M. Di Benedetto, A. Lidozzi, E. J. B. Peña, and L. Solero, "Parameters estimation of a 3-phase ac-dc converter based on the digital twin method", in *2023 IEEE Energy Conversion Congress and Exposition (ECCE)*, IEEE, 2023, pp. 2937–2944.

[121] P. B. Nazif et al., "Parameter identification for dc-dc buck converter digital twin considering sensors errors", *IEEE Journal of Emerging and Selected Topics in Power Electronics*, 2025.

[122] Q. Wu, W. Wang, Q. Wang, L. Xiao, and B. Hu, "Digital twin approach for degradation parameters identification of a single-phase dc-ac inverter", in *2022 IEEE Applied Power Electronics Conference and Exposition (APEC)*, IEEE, 2022, pp. 1725–1730.

[123] A. Sharida, N. F. Kamal, H. Alnuweiri, S. Bayhan, and H. Abu-Rub, "Digital-twin-based diagnosis and tolerant control of t-type three-level rectifiers", *IEEE open journal of the industrial electronics society*, vol. 4, pp. 230–241, 2023.

[124] H. Shi, L. Xiao, Q. Wu, and W. Wang, "Digital twin approach for igbt parameters identification of a three-phase dc-ac inverter", in *2022 IEEE Transportation Electrification Conference and Expo, Asia-Pacific (ITEC Asia-Pacific)*, IEEE, 2022, pp. 1–4.

[125] S. Zhang, W. Song, H. Cao, T. Tang, and Y. Zou, "A digital-twin-based health status monitoring method for single-phase pwm rectifiers", *IEEE transactions on power electronics*, vol. 38, no. 11, pp. 14 075–14 087, 2023.

[126] M. T. Fard, B. J. Luckett, and J. He, "Digital twin enabled open-circuit fault diagnosis for five-level anpc multilevel converters", *IEEE Journal of Emerging and Selected Topics in Power Electronics*, 2024.

[127] S. de Lopez Diz, R. M. López, F. J. R. Sánchez, E. D. Llerena, and E. J. B. Peña, "A real-time digital twin approach on three-phase power converters applied to condition monitoring", *Applied Energy*, vol. 334, p. 120 606, 2023.

[128] P. Wang, Y. An, Y. Ding, and X. Gu, "Real-time monitoring method for small-signal stability of vsc-hvdc converter based on digital twin approach", in *2024 IEEE PES 16th Asia-Pacific Power and Energy Engineering Conference (APPEEC)*, IEEE, 2024, pp. 1–5.

[129] W. Han, L. Cheng, W. Han, C. Yu, and Z. Yin, "Adaptive update method of digital twin for dc-dc converter based on mechanism-data drive", *IEEE Sensors Journal*, 2024.

[130] Y. Liu, X. Qing, and G. Chen, "One-cycle digital twin based multi-parameters identification of power electronic converters with simple implementation and high accuracy", *IEEE Transactions on Instrumentation and Measurement*, 2024.

[131] M. Milton, C. De La O, H. L. Ginn, and A. Benigni, "Controller-embeddable probabilistic real-time digital twins for power electronic converter diagnostics", *IEEE Transactions on Power Electronics*, vol. 35, no. 9, pp. 9850–9864, 2020.

[132] G. Di Nezio, M. di Benedetto, A. Lidozzi, and L. Solero, "Dc-dc boost converters parameters estimation based on digital twin", *IEEE transactions on industry applications*, vol. 59, no. 5, pp. 6232–6241, 2023.

[133] S. de Lopez Diz, R. M. Lopez, F. J. R. Sanchez, and E. J. B. Peña, "A digital twin approach for online impedance-based stability analysis of three-phase ac systems", *IEEE Transactions on Industrial Electronics*, 2024.

[134] Y. Li, B. Bohara, H. S. Krishnamoorthy, and J. Seshadrinath, "Data-driven digital twins for monitoring the health and performance of converters", in *2024 IEEE International Communications Energy Conference (INTELEC)*, IEEE, 2024, pp. 1–6.

[135] K. Choksi, A. B. Mirza, A. Zhou, D. Singh, M. Hijikata, and F. Luo, "Self-evolving digital twin-based online health monitoring of multiphase boost converters", *IEEE Transactions on Power Electronics*, vol. 38, no. 12, pp. 16 100–16 117, 2023.

[136] G. Di Nezio, M. Di Benedetto, A. Lidozzi, and L. Solero, "Digital-twin based health monitoring for multi-phase boost rectifier in wind offshore applications", *IEEE Journal of Emerging and Selected Topics in Power Electronics*, 2024.

[137] Y. Peng, S. Zhao, and H. Wang, "A digital twin based estimation method for health indicators of dc–dc converters", *IEEE Transactions on Power Electronics*, vol. 36, no. 2, pp. 2105–2118, 2020.

[138] V. Ruuskanen et al., "Design and implementation of a power-hardware-in-loop simulator for water electrolysis emulation", *Renewable Energy*, vol. 119, pp. 106–115, 2018.

[139] V. Rajasekar and K. Sathya, "Healthcare cyberspace: Medical cyber physical system in digital twin", in IET, 2023.

[140] H. Laaki, Y. Miche, and K. Tammi, "Prototyping a digital twin for real time remote control over mobile networks: Application of remote surgery", *Ieee Access*, vol. 7, pp. 20 325–20 336, 2019.

[141] H. Zhang, Y. Lu, J. Zhang, and A. Benigni, "Real-time simulation of an electrolyzer with a diode rectifier and a three-phase interleaved buck converter", in *2022 IEEE 13th International Symposium on Power Electronics for Distributed Generation Systems (PEDG)*, 2022, pp. 1–6. DOI: 10.1109/PEDG54999.2022.9923192.

[142] Ø. Ulleberg, "Modeling of advanced alkaline electrolyzers: A system simulation approach", *Int. J. Hydrogen Energy*, vol. 28, no. 1, pp. 21–33, 2003.

[143] D. Falcão and A. Pinto, "A review on pem electrolyzer modelling: Guidelines for beginners", *J. Cleaner Production*, vol. 261, p. 121 184, 2020.

[144] A. Ursúa and P. Sanchis, "Static–dynamic modelling of the electrical behaviour of a commercial advanced alkaline water electrolyser", *Int. J. hydrogen energy*, vol. 37, no. 24, pp. 18 598–18 614, 2012.

[145] N. Gallandat, K. Romanowicz, and A. Züttel, "An analytical model for the electrolyser performance derived from materials parameters", *J. Power and Energy Engineering*, vol. 5, no. 10, pp. 34–49, 2017.

[146] D. Aikens, *Electrochemical methods, fundamentals and applications*, 1983.

[147] S. R. Sanders, J. M. Noworolski, X. Z. Liu, and G. C. Verghese, "Generalized averaging method for power conversion circuits", *IEEE Transactions on power Electronics*, vol. 6, no. 2, pp. 251–259, 1991.

[148] W. Foundation. "Fourier series". [Online]. Available: `https://en.wikipedia.org/wiki/Fourier%5C_series`.

[149] Plexim. "Rt-box 2". [Online]. Available: `https://www.plexim.com/products/rt%5C_box/rt%5C_box%5C_2`.

[150] S. Inoue and H. Akagi, "A bidirectional isolated dc–dc converter as a core circuit of the next-generation medium-voltage power conversion system", *IEEE Transactions on Power Electronics*, vol. 22, no. 2, pp. 535–542, 2007.

[151] S. Inoue and H. Akagi, "A bidirectional dc–dc converter for an energy storage system with galvanic isolation", *IEEE Transactions on Power Electronics*, vol. 22, no. 6, pp. 2299–2306, 2007.

[152] R. W. De Doncker, D. M. Divan, and M. H. Kheraluwala, "A three-phase soft-switched high-power-density dc/dc converter for high-power applications", *IEEE Transactions on Industry Applications*, vol. 27, no. 1, pp. 63–73, 1991.

[153] M. Kheraluwala, R. W. Gascoigne, D. M. Divan, and E. D. Baumann, "Performance characterization of a high-power dual active bridge dc-to-dc converter", *IEEE Transactions on Industry Applications*, vol. 28, no. 6, pp. 1294–1301, 1992.

[154] B. Zhao, Q. Song, W. Liu, and Y. Sun, "Overview of dual-active-bridge isolated bidirectional dc–dc converter for high-frequency-link power-conversion system", *IEEE Transactions on power electronics*, vol. 29, no. 8, pp. 4091–4106, 2013.

[155] A. K. Jain and R. Ayyanar, "Pwm control of dual active bridge: Comprehensive analysis and experimental verification", *IEEE transactions on power electronics*, vol. 26, no. 4, pp. 1215–1227, 2010.

[156] H. Bai and C. Mi, "Eliminate reactive power and increase system efficiency of isolated bidirectional dual-active-bridge dc–dc converters using novel dual-phase-shift control", *IEEE Transactions on power electronics*, vol. 23, no. 6, pp. 2905–2914, 2008.

[157] H. Bai, Z. Nie, and C. C. Mi, "Experimental comparison of traditional phase-shift, dual-phase-shift, and model-based control of isolated bidirectional dc–dc converters", *IEEE Transactions on Power Electronics*, vol. 25, no. 6, pp. 1444–1449, 2009.

[158] B. Zhao, Q. Song, and W. Liu, "Power characterization of isolated bidirectional dual-active-bridge dc–dc converter with dual-phase-shift control", *IEEE Transactions on Power Electronics*, vol. 27, no. 9, pp. 4172–4176, 2012.

[159] X. Liu et al., “Novel dual-phase-shift control with bidirectional inner phase shifts for a dual-active-bridge converter having low surge current and stable power control”, *IEEE Transactions on Power Electronics*, vol. 32, no. 5, pp. 4095–4106, 2016.

[160] F. Krismer and J. W. Kolar, “Accurate small-signal model for the digital control of an automotive bidirectional dual active bridge”, *IEEE transactions on power electronics*, vol. 24, no. 12, pp. 2756–2768, 2009.

[161] F. Krismer and J. W. Kolar, “Closed form solution for minimum conduction loss modulation of dab converters”, *IEEE Transactions on Power Electronics*, vol. 27, no. 1, pp. 174–188, 2011.

[162] M. Kim, M. Rosekeit, S.-K. Sul, and R. W. De Doncker, “A dual-phase-shift control strategy for dual-active-bridge dc-dc converter in wide voltage range”, in *8th International Conference on Power Electronics-ECCE Asia*, IEEE, 2011, pp. 364–371.

[163] N. Hou and Y. W. Li, “Overview and comparison of modulation and control strategies for a nonresonant single-phase dual-active-bridge dc–dc converter”, *IEEE Transactions on Power Electronics*, vol. 35, no. 3, pp. 3148–3172, 2019.

[164] *Op4610xg*, `https://opal-rt.atlassian.net/wiki/spaces/PHDGD/pages/550995535/OP4610XG+System+Description`, Accessed: 2024-05-31.

[165] *Opcomm*, `https://opal-rt.atlassian.net/wiki/spaces/PRD/pages/144180849/OpComm`, Accessed: 2024-05-26.

Curriculum Vitæ

Rohan Shailesh DESHMUKH

19-08-1996 Born in Thane, Maharashtra, India.

Education

2021–2025 Ph.D. candidate
Delft University of Technology, Delft, The Netherlands

2019–2021 MSc. Electrical Power Engineering
Delft University of Technology, Delft, The Netherlands

2014–2018 B.E Electrical Engineering
Babaria Institute of Technology, Vadodara, Gujarat, India

Work Experience

2021–2025 Ph.D. candidate
Delft University of Technology, Delft, The Netherlands

List of Publications

Included in this thesis

Journal Papers

1. **R. S. Deshmukh**, P. Bauer and H. Vahedi, "High-Accuracy Generalized Average Model of Dual Active Bridge Converters," in IEEE Open Journal of Power Electronics, vol. 5, pp. 452-460, 2024, doi: 10.1109/OJPEL.2024.3382808.

2. **Rohan Shailesh Deshmukh**, Gautam Rituraj, Pavol Bauer, Hani Vahedi, "Real-time digital twin implementation of power electronics-based hydrogen production system", Energy Reports, Volume 13, 2025, pp. 5006-5015, doi: 10.1016/j.egyr.2025.04.017.

3. **R. S. Deshmukh**, G. Rituraj, P. Bauer, H. Vahedi, "Evaluation and Optimization of Modulation Strategies of a Dual Active Bridge Converter for Electrolyzers", IEEE Open Journal of the Industrial Electronics Society *(Accepted)*.

Conference Papers

1. **R. S. Deshmukh**, A. Shekhar and P. Bauer, "Adaptive Modularity for Power Electronics Based Electrolysis Systems for Green Hydrogen," 2022 IEEE 20th International Power Electronics and Motion Control Conference (PEMC), Brasov, Romania, 2022, pp. 508-515, doi: 10.1109/PEMC51159.2022.9962941.

2. **R. S. Deshmukh**, G. Rituraj, H. Vahedi, A. Shekhar and P. Bauer, "Impact of Electrolyzer on the Operation of a Dual Active Bridge Converter," IECON 2023-49th Annual Conference of the IEEE Industrial Electronics Society, Singapore, Singapore, 2023, pp. 1-6, doi: 10.1109/IECON51785.2023.10312636.

3. **R. S. Deshmukh**, G. Rituraj, N. Lock, H. Vahedi, A. Shekhar and P. Bauer, "Implementation of Real-Time Digital Twin of Dual Active Bridge Converter in Electrolyzer Applications," IECON 2023- 49th Annual Conference of the IEEE Industrial Electronics Society, Singapore, Singapore, 2023, pp. 1-6, doi: 10.1109/IECON51785.2023.10312274.

OUTSIDE OF THIS THESIS

CONFERENCE PAPERS

1. A. Shekhar, G. Rituraj, R. van der Sande, M. Ahmadi, **R. S. Deshmukh**, P. Bauer, V. Nougain, A. Lekić, P. Palensky, "Development of Reliable Power Electronic Systems using Real Time Digital Twin Based Power Hardware-in-the-Loop Testbed," 2023 IEEE Belgrade PowerTech, Belgrade, Serbia, 2023, pp. 1-6, doi: 10.1109/PowerTech55446.2023.10202818.

2. R. van der Sande, **R. Deshmukh**, A. Shekhar and P. Bauer, "DC Link Capacity Enhancement for MMC-based Distribution Link using Dynamic Voltage Operation," 2023 11th International Conference on Power Electronics and ECCE Asia (ICPE 2023 - ECCE Asia), Jeju Island, Korea, Republic of, 2023, pp. 636-642, doi: 10.23919/ICPE2023-ECCEAsia54778.2023.10213697.

ADVISED MSC THESIS

1. N. Lock, "Digital Twin of an isolated DC/DC converter for electrolysis." Master's thesis in Electrical Engineering, Delft University of Technology, 28 September, 2023. Available online: https://resolver.tudelft.nl/uuid:6b41fa94-ed55-4536-9b5c-250862f805f2

2. R. van der Sande, "DC link capacity enhancement for dynamic operation of back-to-back modular multilevel converters." Master's thesis in Electrical Engineering, Delft University of Technology, 23 September, 2022. Available online: https://resolver.tudelft.nl/uuid:4f102dea-7213-49e7-b55f-d1e67b44d947